Austenite-Martensite Phase Transformation and Magneto-Mechanical Studies on Nickel Manganese Gallium Single Crystal Alloy

A DISSERTATION
SUBMITTED TO THE FACULTY OF THE GRADUATE SCHOOL
OF THE UNIVERSITY OF MINNESOTA
BY

YIMING WU

IN PARTIAL FULFILLMENT OF THE REQUIREMENTS
FOR THE DEGREE OF
DOCTOR Of PHILOSOPHY

THOMAS W. SHIELD, ADVISOR

May, 2010

Acknowledgements

First of all, I want to express my appreciation to my advisor, Professor Thomas W. Shield, all his support and encouragement make this work possible. I feel so lucky that I can do my research under his directing as a graduate student.

I would like to thank Professor Richard D. James not only for all helpful discussion during courses, seminars and meetings, but also for his suggestions as my committee member. I also thank the committee chair Professor Perry H. Leo, committee members Professor Mitchell B. Luskin, and Professor Ellad Tadmor for their inspections and comments on this work. Dave Hultman and his workshop are the necessary conditions for the success of my experiments, whenever I have a design problem on instrument, Dave always gives me best solutions.

I want to thank my family and friends for their consistent supports during all these high education years. Their love encourages me to keep moving forward. I also want to thank Dr. Jun Cui, Dr. Zhiyong Zhang, Dr. Liping Liu, Dr. Vijay Kumar Srivastava, graduate students, Pei Li, Xian Chen, Ganesh Borra, Sakthivel Kasinathan, and faculty and staff of the Department of Aerospace Engineering and Mechanics, for all of their help.

I am honored to be supported by research assistantships funded by my advisor, Professor Tom Shield, and fellowship funded by Kenneth G. and Rosemary R. Anderson Scholarship during my graduate research at the University of Minnesota.

For my parents and my lover Shuang

Abstract

The results of experiments on austenite-martensite phase transformation and magneto-mechanical behavior of a NiMnGa ferromagnetic shape-memory alloy are reported. This alloy undergoes a cubic to tetragonal martensitic phase transformation at about 5 ^{o}C and both phases are ferromagnetic. These experiments were conducted using a Magneto-Mechanical Testing Machine (MMTM) that is capable of simultaneously applying a uni-axial load and a magnetic field that can be varied in a plane containing the mechanical loading axis. One of the main accomplishments of this work was the extension of these measurements to tensile loads. Two types of experiments were conducted. First a set of experiments were performed to determine the effects of applied loads and magnetic fields on the transformation temperature of the alloy. The effect of compression on the phase transformation is about 0.2 to 0.4 K/MPa, while the effect of tension is only 0.1 to 0.2 K/MPa. These results agree with predictions made using the Clausius-Clapeyron equation. The effects of applied magnetic field are more complicated and do not follow the simple tends predicted by this equation. Observations of the microstructure that forms during transformation agree reasonably well with the predictions of the crystallographic theory of martensite.

The second set of experiments was conducted to measure the behavior of the alloy under a constant load and applied magnetic fields. These experimental results are directly applicable to using this material in an actuator. Several different magnetic fields paths were used to determine if this has an effect on the strains observed. Measurements of the specimen average magnetization where also made using Hall probes to measure the stray field produced by the specimen during these experiments. These results have

some portions of the strain-magnetization curves that are linear, which is what is predicted by models that have both of these quantities directly related to variant volume fractions. Two of the key parameters for actuators that were measured are blocking stress and work output. It was found that the maximum work output occurs for a small tensile bias load due to the reduced effect of specimen demagnetization in this case. The blocking stress in tension appears to be just above the largest tensile stress of 3 MPa that could be applied, which is similar to the value in compression. The values of these two parameters compare well to values in the literature for compression, while the tensile results are the first to be reported.

Contents

List of Tables

List of Figures

Chapter 1

Introduction

Shape memory alloys (SMAs) are in the class of active materials, which have many potential uses, such as micro-electro-mechanical sensors and actuators, and medical devices [1, 2, 3, 4, 5, 6]. The name shape-memory comes from the fact that these materials have "memory" of their original shapes and can return to their original shape even after large deformations. The thermomechanical behavior of SMAs has been studied theoretically and experimentally for decades. It is well known that the shape memory mechanism is based on the solid-solid phase transformation between an austenite phase, which has high symmetry (typically cubic), and a martensite phase, which has lower symmetry (such as tetragonal, trigonal, orthorhombic or monoclinic). The lower symmetry of the martensite means that there are multiple (3, 4, 6 or 12) variants of the martensite with different orientations that are symmetrically related [7]. Phase transformation between austenite and martensite can be induced by temperature and mechanical stress. Although a large amount of research has been done in this field from the material science and applied physics viewpoints, the prediction of the overall thermomechanical behavior of SMAs still remains difficult.

Recently, the study of ferromagnetic shape memory alloys (FSMAs), especially in the Heusler alloy, Ni_2MnGa, has attracted the interest of researchers in the shape memory alloy field [8, 9, 10, 11, 12, 13, 14, 15]. This is due to the ability to use magnetic fields to actuate FSMAs, and generate large reversible strains between martensite variants.

At the same time, there may also be large differences in magnetic properties between austenite and martensite, such as the saturation magnetization. These differences may allow additional uses besides the general uses of shape memory alloys, such as the applications in refrigeration and energy conversion. Among the FSMAs, such as FePd, CoNiGa and Ni_2MnGa alloys, Ni_2MnGa has some of the most desirable characteristics for applications [16, 17] and thus of will be the subject of this study.

Some applications of FSMA materials make use of the austenite-martensite phase transformation process. When SMAs were discovered, it was found that one of the shape-memory characteristics is a large austenite-martensite phase transformation strain, which provides an efficient mechanism for converting heat to the mechanical energy. While stress effects on the shape-memory transformation are well understood, the effects of magnetic fields on this process are less understood and will also be studied here.

In recent papers, Liang *et al*. [18] reported a calculation of stress-magnetic field-temperature phase transformation diagram for FSMAs and some experimental results. In our research group, the effects of stress and magnetic field on the FePd and Ni_2MnGa FSMAs were researched by Cui *et al*. [19]. It was found that the effect of magnetic field on the phase transformation is small. This is because the differences between saturation magnetizations of austenite and martensite for both FePd and Ni_2MnGa are very small. Additional measurements, reported here, extend the range of these results.

The other important potentially useful FMSA mechanism is martensite variant rearrangement with applied magnetic field. This results in a magnetically induced strain that can be used to make actuators. It can also be used to convert magnetic energy to mechanical energy. The Ni_2MnGa alloy is studied because of its large magnetic induced strain [8, 9, 10, 11, 20, 21, 22, 23]. The differences between these published results may come from differences of stress conditions, different magnitude of applied magnetic field and differences in the composition of the alloys. The amount of agreement with theoretical results also varies. Questions remain as to which factors have the most influence on the behavior of Ni_2MnGa.

The current theoretical models for magnetic field induced strains are based on the rearrangement of martensite variants with applied magnetic field. This rearrangement seems to have been first suggested by Vasil'ev *et al.* [24], when they tried to measure the $\langle 110 \rangle$ magnetostriction of Ni_2MnGa. And the first experiment focusing on variant rearrangement was performed by Ullakko *et al.* [8]. More theoretical study of this variant rearrangement phenomenon have been given by James and Wuttig [12] and O'Handley [13]. Based on a particular twinned domain structure and magnetic anisotropy, O'Handley showed good agreement with Ullakko's experiment results. On the other hand, James and Wuttig's theory is more general, because it does not need to assume a particular domain structure, and considers the minimization of a micromagnetic energy function that includes applied field, stress and demagnetization energies. Most recent theoretical analysis are based on James and Wuttig's model.

A property related to magnetic field induce strain, was also studied by Ganor, Shilo, Shield and James [25]. When a large enough stress is applied to Ni_2MnGa FSMA, martensite variant rearrangement is inhibited and only magnetization rotation occurs. This applied stress is called the blocking stress. It limits actuator applications. The blocking stress and work output under compressive and tensile stress conditions are also reported in this thesis.

Consider about the demagnetization factors of the long rectangular sample, the low demagnetization factor in longitude direction of sample makes it easy to saturated magnetized in longitude direction, but hard in transverse direction. A long rectangular single crystal Ni_2MnGa sample results in large displacements and low demagnetization factor for fields with long direction. Demagnetization factors quantify the effect of magnetic materials shape on the ease of magnetizing it in a given direction. It is easier to magnetize material along its longest direction. For compression in the long direction, which makes the sample shorter, the applied field to extend the sample is in the transverse direction that hard to magnetize the sample. This makes a large magnetic field induced strain, in the case of an applied tension, the field needed to shorten

the sample is in the easy to magnetize long direction of the sample. So the actuator with magnetic field application under tension condition will get larger work output for smaller fields. All current experimental results reported are for compressive loading conditions, which means that the influence of the stress has only been partially studied. After redesigning the sample fixture in the Magneto-Mechanical Test Machine, a series of magneto-mechanical experiments on single crystal Ni_2MnGa material under varying amounts of tension were completed.

The organization of this thesis is as follow: In Chapter 2, all background information will be reviewed, which includes fundamental theories, basic material properties and summarization of other reported experimental results on the Ni_2MnGa phase transformation process and magneto-mechanical behavior. Chapter 3 introduces the sample preparation processes and the details of experimental apartatus. In Chapter 4, the effects of different applied stresses and magnetic fields on the austenite-martensite phase transformation processes, including phase transformation temperatures, phase transformation strains, will be given. In Chapter 5, based on the designed magneto-mechanical experiment measurements, magnetic field induced strains, blocking stresses and work outputs under different uniaxial stresses (compression or tension) will be studied carefully. Finally, conclusions will be given and future work will be proposed in Chapter 6.

Chapter 2

Background

This chapter presents background information on Ni_2MnGa ferromagnetic shape memory alloy research. First, some fundamental theories, including continuum mechanics, crystallographic theory, ferromagnetic theory and phase transformation are introduced, and the model for ferromagnetic shape memory behavior is described. Then, the theoretical analysis of stress and magnetic field effects on phase transformation is shown explicitly. Finally, some basic material properties and summarization of other reported experimental results on Ni_2MnGa phase transformation process and magneto-mechanical behavior are introduced.

2.1 Continuum Mechanics and Continuum Theory of Crystal Solids

Because most of the theoretical analysis in this thesis is based on principles of continuum mechanics and continuum theory of crystal solids, these theories will be introduced first in the subsection below.

2.1.1 Deformation Gradient and Kinematic Compatibility

Consider a body $\mathfrak{B}$, as shown in Figure 2.1, described by material points at position $\mathbf{X}$, in a reference configuration. Here the bold letter means vector in $\mathbb{R}_3$ and same below, and the italicized letters will be used to represent scalars. Let the deformation of the body be given as $\mathbf{x} = \mathbf{x}(\mathbf{X}, t)$, where $\mathbf{x}$ is the current location of the material point at position $\mathbf{X}$ and time t. The deformation gradient $\mathbf{F}$ of the body is the matrix of partial derivatives, i.e., it has components

$$F_{ij} = \frac{\partial x_i}{\partial X_i} \qquad i, j = 1, 2, 3. \tag{2.1}$$

in a rectangular Cartesian coordinate system. Here, indicial notation is used for $\mathbf{F}$ with components F_{ij} in a Cartesian coordinate system with ortho-normal base vectors $\mathbf{e}_i$ where i, j=1, 2, 3 and repeated indices will imply summation in this range.

Now consider a differential material volume dV at the material point $\mathbf{X}$ in Figure 2.1. After deformation, dV becomes to the differential volume dv. The relationship between dV and dv can be found as

$$dv = (\det\mathbf{F})dV. \tag{2.2}$$

So, the determinant of the deformation gradient describes the local volume change.

Then, consider the differential material area dA with unit normal $\mathbf{n}$ in the reference configuration. After deformation in Fig. 2.1, it becomes the differential area da with unit normal $\mathbf{m}$, given by

$$\mathbf{m} = \frac{\mathbf{F}^{-\mathrm{T}}\mathbf{n}}{|\mathbf{F}^{-\mathrm{T}}\mathbf{n}|} \tag{2.3}$$

and

$$da = |(\mathrm{cof}\mathbf{F})\mathbf{n}|dA, \tag{2.4}$$

thus the cofactor of the deformation gradient describes the local area change. Consider the piecewise homogeneous deformation in Figure 2.2. The two parts of the body have been sheared differently, but the body remains unbroken. The deformation of the material is continuous, but the deformation gradient is not. Suppose the deformation

in Figure 2.2 is described by

$$\mathbf{x} = \begin{cases} \mathbf{F}_1\mathbf{X} + \mathbf{c}_1, & \mathbf{X} \in \mathfrak{B}_1 \\ \mathbf{F}_2\mathbf{X} + \mathbf{c}_2, & \mathbf{X} \in \mathfrak{B}_2 \end{cases}, \tag{2.5}$$

where $\mathbf{F}_1$, $\mathbf{F}_2$ are constant positive definite matrices, and $\mathbf{c}_1$ and $\mathbf{c}_2$ are constant vectors. Because the deformation of the plane is given by $(\mathrm{cof}\mathbf{F})\mathbf{n}$, if the deformation is continuous, the necessary condition is

$$(\mathrm{cof}\mathbf{F}_1)\mathbf{n} = (\mathrm{cof}\mathbf{F}_2)\mathbf{n}. \tag{2.6}$$

This implies

$$\mathbf{F}_1 - \mathbf{F}_2 = \mathbf{a} \otimes \mathbf{n} \tag{2.7}$$

for some vector $\mathbf{a}$. This is called the kinematic compatibility or rank-one connection condition [26].

2.1.2 Bravais Lattice

In continuum crystalline solids theory, an infinite set of points in three dimension, which are generated by the translation of a single point $\mathbf{o}$ through three linearly independent lattice vectors by integer amounts, i.e.,

$$\mathfrak{L}(\mathbf{e}_i, \mathbf{o}) = \{\mathbf{x} : \mathbf{x} = \nu^i \mathbf{e}_i + \mathbf{o}, \quad \nu^1, \nu^2, \nu^3 \in \mathbb{Z}\} \tag{2.8}$$

is called a Bravais lattice. The lattice vectors $\{\mathbf{e}_1, \mathbf{e}_2, \mathbf{e}_3\}$ define a unit cell. Figure 2.3 shows some examples of lattice vectors.

Now consider two Bravais lattice $\mathfrak{L}(\mathbf{e}_i, \mathbf{o})$ and $\mathfrak{L}(\mathbf{f}_i, \mathbf{o})$, which are generated by lattice vectors $\{\mathbf{e}_i\}$ and $\{\mathbf{f}_i\}$ respectively. If there exists a matrix with $\det\mathbf{F} \neq 0$ such that

$$\mathbf{f}_i = \mathbf{F}\mathbf{e}_i \tag{2.9}$$

we may consider the lattice $\mathfrak{L}(\mathbf{f}_i, \mathbf{o})$ as a deformation of $\mathfrak{L}(\mathbf{e}_i, \mathbf{o})$ by amount $\mathbf{F}$.

Consider a set of deformations

$$\mathfrak{G}(\mathbf{e}_i) = \{\mathbf{H} : \mathbf{H}\mathbf{e}_i = {\mu_i}^j \mathbf{e}_j\}, \tag{2.10}$$

where 3×3 integers matrix ${\mu_i}^j$ satisfy

$$\det[{\mu_i}^j] = 1, \tag{2.11}$$

if this maps the lattice back into itself, and it is called the symmetry group of the lattice. This includes both translations and rotations.

Also, we can define the point group a lattice $\mathfrak{P}(\mathbf{e}_i)$ as the set of rotations, which maps a lattice back to itself:

$$\mathfrak{P}(\mathbf{e}_i) = \{\mathbf{R} : \mathbf{R}\mathbf{e}_i = {\mu_i}^j \mathbf{e}_j\} \tag{2.12}$$

where $\mathbf{R}$ is a rotation, $\mathbf{R}^T\mathbf{R} = \mathbf{I}$ and ${\mu_i}^j$ satisfies (2.11).

There are seven distinct point groups for Bravais lattice systems. These are shown in Table 2.1 [26].

2.2 Austenite-Martensite Phase Transformation

Martensite, named after the German metallurgist Adolf Martens (1850-1914), is any crystal structure that is formed by displacive transformation, as opposed to much slower diffusive transformations [27]. The transformation process which transforms one crystal structures to another by a displacive transformation is called a martensitic transformation. Two key characteristics of martensite transformations distinguish them from other transformations. One is that the transformation takes place very rapidly, that is long-range diffusion plays no part in the transformation. The other is that the shape of transforming region changes due to a change in the crystal structure of the material. This kind of transformation typically occurs when the material crystal structure transforms from a high symmetry (typically cubic), called austenite, to a lower symmetry, such as, tetragonal, trigonal, orthorhombic or monoclinic structure. In addition, there

is no diffusive type rearrangement of atoms, as shown in Figure 2.4. The martensite transformation exists in many metals and alloys.

Martensite transformation begins at a certain temperature M_s, which is affected by stress or magnetic field applied to the material. When the material reaches martensite-start temperature, M_s, martensite is nucleated at some point in the material, and then the martensite spreads rapidly to the whole material. During this process, there is a boundary between martensite and austenite, which is called an A-M interface. This interface must be compatible as discussed in subsection 2.1.1.

Suppose the lattice vectors of the austenite phase are $\{\mathbf{e}_1^0, \mathbf{e}_2^0, \mathbf{e}_3^0\}$ and those of martensite are $\{\mathbf{e}_1, \mathbf{e}_2, \mathbf{e}_3\}$. Because the thermal expansions of both sets of lattice vectors are much smaller than the distortions during phase transformation process, thermal expansion influences of temperature θ on them will be neglected for simplicity. Then there is a deformation

$$\mathbf{e}_i = \mathbf{R}\mathbf{U}\mathbf{e}_i^0, \tag{2.13}$$

where $\mathbf{R}$ is the same as definition in subsection 2.1.2 and $\mathbf{U}$ is the stretch matrix, which describes the homogeneous deformation between austenite lattice and martensite lattice.

Consider the example in Figure 2.4 without any rotation, which is a cubic to tetragonal transformation that Ni_2MnGa undergoes [28]. It can be described as a Bravais lattice both in the austenite and the martensite phase. It transforms a face-centered-cubic (FCC) lattice in the austenite to a face-centered-tetragonal (FCT) lattice in the martensite. This FCT could be obtained by compressing the one axis and expending the other two axes of FCC. The lattice vectors of the austenite and martensite are

$$\mathbf{e}_1^0 = \begin{pmatrix} a_0 \\ 0 \\ 0 \end{pmatrix}, \mathbf{e}_2^0 = \begin{pmatrix} 0 \\ a_0 \\ 0 \end{pmatrix}, \mathbf{e}_3^0 = \begin{pmatrix} 0 \\ 0 \\ a_0 \end{pmatrix} \tag{2.14}$$

and

$$\mathbf{e}_1 = \begin{pmatrix} c \\ 0 \\ 0 \end{pmatrix}, \mathbf{e}_2 = \begin{pmatrix} 0 \\ a \\ 0 \end{pmatrix}, \mathbf{e}_3 = \begin{pmatrix} 0 \\ 0 \\ a \end{pmatrix} \tag{2.15}$$

or

$$\mathbf{e}_1 = \begin{pmatrix} a \\ 0 \\ 0 \end{pmatrix}, \mathbf{e}_2 = \begin{pmatrix} 0 \\ c \\ 0 \end{pmatrix}, \mathbf{e}_3 = \begin{pmatrix} 0 \\ 0 \\ a \end{pmatrix} \tag{2.16}$$

or

$$\mathbf{e}_1 = \begin{pmatrix} a \\ 0 \\ 0 \end{pmatrix}, \mathbf{e}_2 = \begin{pmatrix} 0 \\ a \\ 0 \end{pmatrix}, \mathbf{e}_3 = \begin{pmatrix} 0 \\ 0 \\ c \end{pmatrix} \tag{2.17}$$

where a_0 is lattice parameter of FCC austenite and a and c are lattice parameters of FCT martensite. From (2.13), and the different lattice vectors of the austenite and martensite in (2.14)-(2.17), the stretch matrices from FCC to FCT are

$$\mathbf{U}_1 = \begin{pmatrix} \beta & 0 & 0 \\ 0 & \alpha & 0 \\ 0 & 0 & \alpha \end{pmatrix}, \mathbf{U}_2 = \begin{pmatrix} \alpha & 0 & 0 \\ 0 & \beta & 0 \\ 0 & 0 & \alpha \end{pmatrix}, \mathbf{U}_3 = \begin{pmatrix} \alpha & 0 & 0 \\ 0 & \alpha & 0 \\ 0 & 0 & \beta \end{pmatrix}, \tag{2.18}$$

where $\alpha = a/a_0$, $\beta = c/a_0$.

A number of martensites with different transformation matrices will appear scattered in the sample after the sample transforms from austenite, even though the sample consists of a single crystal. These different martensites are called *variants*. The number of martensitic variants is determined by the crystalline symmetries of austenite and martensite of the material [29]. From Table 2.1, it is known that there are 24 point groups for cubic lattice and 8 for tetragonal, so there will be $24/8 = 3$ variants of tetragonal martensite that transformed from cubic austenite, as shown in Figure 2.4. Each stretch matrix in (2.18) represents a deformation without rotation from the cubic austenite to one of the tetragonal martensite variants during phase transformation process.

2.3 Basic Principles of Ferromagnetic Materials

Ferromagnetic shape memory alloys attracting more research interests than normal shape memory alloys is mainly based on their ferromagnetic property besides general shape memory properties, which provides potential uses in magneto-mechanical energy exchange, sensing and actuation. So the understanding of ferromagnetic principles is necessary to study FSMAs.

Ferromagnetic materials are materials which have magnetic properties similar to iron. They can be attracted to permanent magnets and can be permanently magnetized. These magnetic properties disappear when the material is above a certain temperature, T_c, called Curie temperature. For our Ni_2MnGa material, T_c is above the martensitic transformation temperatures and austenite is ferromagnetic.

It is known that there is a magnetic field around the magnetic material, which is generated by the material itself, as shown in Figure 2.5 (a). A magnetic field can be also generated by a current flowing in a coil, as Figure 2.5 (b). The magnetic field generated by the magnetic material is called stray or demagnetization field $\mathbf{H}_d$, which is present inside and outside the material. The demagnetization field, $\mathbf{H}_d$ is produced by the magnetization $\mathbf{M}$ of the magnetic material. In Figure 2.5 (b), the current flow in the coil simply produces the magnetic field $\mathbf{H}_0$ [30]. In our experiments, the applied magnetic field is generated by the current flow in the coils on the test machine.

The exterior magnetic fields produced by magnetic material and current flow can be described by (in cgs, Gaussian magnetic units system)

$$\mathbf{B} = \mathbf{H}_0 + \mathbf{H}_d, \tag{2.19}$$

where $\mathbf{B}$ is the magnetic flux density. And the magnetic field inside the material in Figure 2.5 (a) is given by

$$\mathbf{B} = \mathbf{H}_0 + \mathbf{H}_d + 4\pi\mathbf{M}. \tag{2.20}$$

Here, $\mathbf{B}$, $\mathbf{H}_0$ and $\mathbf{H}_d$ are in units of $Gauss$, and $\mathbf{M}$ in unit of emu/cm^3. The magnetic flux density must satisfy Maxwell's equations of magnetostatics, which is:

$$\nabla \cdot \mathbf{B} = 0 \tag{2.21}$$

and jump condition

$$[|\mathbf{B} \cdot \mathbf{n}|] = 0, \tag{2.22}$$

where $\mathbf{n}$ is the unit normal a discontinuity surface. Because the applied magnetic field $\mathbf{H}_0$ is assumed to be present without magnetic material, it satisfies (2.21) and (2.22). So (2.21) and (2.22) must be satisfied by $\mathbf{H}_d$ alone with the given magnetization $\mathbf{M}$. The demagnetization field depends strongly on the shape of the magnetic material [30]. And inside the magnetic material, the demagnetization field points in the opposite direction to the magnetization, which may demagnetize the material and tend to a state with zero-average magnetization. This can be quantified through the magnetostatic demagnetization factor $\mathbf{D}$ as

$$\mathbf{H}_d = -\mathbf{D}\mathbf{M}. \tag{2.23}$$

where $\mathbf{D}$ is a tensor and determined by the average demagnetization field over the material volume for uniformly magnetized material. The sum of the demagnetization factors in the three principle directions is 1 [30]. So for a rectangular magnetic specimen with dimensions of $W \times W \times L$, where L is in the long direction, the demagnetization factor along L direction is defined as

$$D_L = D(\mathbf{e}_3). \tag{2.24}$$

Then the other two factors along the other edges are:

$$D_W = (1 - D_L)/2. \tag{2.25}$$

If $L > W$, then $D_L < D_W$, and the material prefers to be magnetized along the L direction. The demagnetization factor can be calculated numerically for rectangular samples by

$$\mathbf{H}_d = -\nabla(\int_B -\frac{\nabla \mathbf{M}}{r} dv + \int_S \frac{\mathbf{n} \cdot \mathbf{M}}{r} dv). \tag{2.26}$$

In the equation, S is the surface of the body $\mathbf{B}$ and $\mathbf{n}$ is the outward unit normal to this surface.

Crystalline ferromagnetic materials are usually magnetically anisotropic and will have a preferred or easy axis or axes of magnetization. There is a term in the total free energy of a magnetic material, which describes the effects of the magnetic anisotropy. This term combined with the Zeeman (applied field) and demagnetization energies can be combined to give the total magnetic energe

$$E_{Mag} = -4\pi \int_V \mathbf{H}_0 \cdot \mathbf{M} dv + \frac{1}{2} \int_{R^3} \mathbf{H}_d \cdot \mathbf{H}_d dv + \int_V \phi(\mathbf{M}) dv, \tag{2.27}$$

where $\phi(\mathbf{M})$ is the anisotropy magnetic energy of the specimen and V is the material volume. Here the exchange energy has been omitted, because only piecewise homogeneous domain patterns with zero exchange energy will be considered. In ferromagnetic materials, the magnitude of the magnetization can be expressed as a function of temperature, which vanishes at Curie temperature. This magnitude is called saturation magnetization, M_S, and

$$\mathbf{M} = M_S \mathbf{m}, \tag{2.28}$$

where $\mathbf{m}$ is a unit vector.

2.4 Compatibility of Microstructures

If a structure is transformed from cubic austenite to tetragonal martensite, there are three possible transformations, whose transformation matrices are given in (2.18). The matrices depend on the lattice constants through α and β. Because none of the principle stretches are equal to 1, a single variant is not compatible with the undeformed austenite. Instead twinned martensite, that is, alternate layers of two variants, forms which on average is compatible with austenite. Ball and James [31] provided a method to calculate the planar austenite-twinned martensite interfaces that are possible given a set of variants. This is equivalent to the crystallographic theory of martensite (CTM).

The microstructure of a austenite-martensite (A-M) interface is shown in Figure 2.6.

The displacements must be continuous across the A-M interface and the twin boundaries. From the discussion of subsection 2.1.1, the relationship of the deformation gradients across each interface must satisfy (2.7). That is, the deformation gradients of the two variants meeting at a twin boundary satisfy

$$\mathbf{R}_{AB}\mathbf{U}_B - \mathbf{U}_A = \mathbf{a} \otimes \mathbf{n}, \tag{2.29}$$

where $\mathbf{R}_{AB}$ is an orthogonal tensor that represents the relative rotation between two variants, $\mathbf{a}$ is the twin shear vector and $\mathbf{n}$ is the normal direction of the twin boundary in the reference configuration. Also, the average deformation of martensite $\mathbf{F}_{AB}$ must satisfy

$$\mathbf{F}_{AB} - \mathbf{I} = \mathbf{b} \otimes \mathbf{m}, \tag{2.30}$$

where $\mathbf{I}$ is the identity matrix that represents the undeformed austenite, $\mathbf{b}$ is the shear vector and $\mathbf{m}$ is the normal to the A-M interface. The average rotation of the martensite is $\mathbf{R}_m$, and the volume fraction of variant A is λ, then average deformation of martensite is given by

$$\mathbf{F}_{AB} = \mathbf{R}_m((1-\lambda)\mathbf{R}_{AB}\mathbf{U}_B + \lambda\mathbf{U}_A). \tag{2.31}$$

If the choice of variants is given, a solution of above CTM problem, which is a set of quantities of $\mathbf{R}_{AB}, \mathbf{R}_m, \lambda, \mathbf{a}, \mathbf{n}, \mathbf{b}, \mathbf{m}$, can be found. This set contains all the A-M interface microstructures that are theoretically possible in the material. More information on this can be found in the works of Ball and James [31] , Shield [29] and Hane [32].

The preferred martensite variants after phase transformation is determined by the applied stress and magnetic field during phase transformation. For example, when the sample is only loaded by an applied stress σ during the phase transformation, the preferred stretch matrix $\mathbf{U}_{pre}$ is obtained by

$$\mathbf{U}_{pre} = \{\mathbf{U}_i | \sigma : \varepsilon(\mathbf{U}_i) \geq 0, \quad i = 1, 2, 3; \} \tag{2.32}$$

where $\varepsilon(\mathbf{U}_i)$ are the possible phase transformation strains based on stretch matrices $\mathbf{U}_i$. And the possible A-M interfaces will be given later for the specific case of Ni_2MnGa material.

2.5 Ni_2MnGa Ferromagnetic Shape Memory Material

There are several alloys belong to ferromagnetic shape memory alloy (FSMA) family, such as Fe_7Pd_3, Ni_2MnGa, Ni_2MnSn, etc. Among them, Ni_2MnGa has been studied extensively in recent years because of its giant magnetic field induced strain under martensite. The research in this thesis is also focused on Ni_2MnGa material. Some of the background information about shape memory effects, material properties and ferromagnetic shape memory mechanism of Ni_2MnGa single crystal material will be introduced in this section.

2.5.1 Shape Memory Effects

Shape memory effects are due to the structural phase transformation between austenite and martensite phases without diffusion. Each lower symmetry martensite variant has a different shape change. If the austenite to martensite phase transformation is induced by a temperature change in the absence of other applied fields and loads, all variants are equally favored because they all have the same free energy. When a load is applied during phase transformation condition or even under martensite, certain variants will be preferred as mentioned in Section 2.4. For example, if uniaxial compression is applied to a sample after phase transformation, the martensite microstructure will consist of almost entirely the single variant whose short axis is best aligned with the uniaxial direction; at the same time, if the sample is cooled without any load, after phase transformation, all three variants will coexist in the microstructure of the specimen as shown in Figure 2.7. But when uniaxial compression is applied to the three-variants martensite sample, the variants will rearrange and favor a single variant microstructure. The variant favored is given by (2.32). This kind of variant rearrange process is also called detwinning.

2.5.2 Material Properties of Ni_2MnGa FSMA

Nickel2-manganese-gallium (Ni_2MnGa) is a Heusler alloy, which is a ferromagnetic alloy based on Heusler phase. The Heusler phase is intermetallic compound with a face-centered cubic (FCC) crystal structure, which was first researched by Heusler *et al.* in 1903 [33]. These alloys have compositions of the form X_2YZ and an $L2_1$-ordered structure. The unit cell schematic drawing of Ni_2MnGa is shown in Figure 2.8. In Ni_2MnGa, the manganese atoms carry most of the magnetic moment.

The austenite-martensite phase transformation for exact Ni_2MnGa is from cubic to tetragonal, as shown in Figure 2.4. Alloys near Ni_2MnGa but with different components of Ni, Mn, Ga may have complicated transformation behaviors. Kokorin and Martynov [34] showed martensitic phase transformation in the $Ni_{49.2}Mn_{29.6}Ga_{21.2}$ alloy is complex and the tetragonal phase contains a super structure arising along $(110)[110]_m$ system over 5 subcells. This is not the only transformation behavior in martensitic transformation for nickel-manganese-gallium alloys. Sozinov *et al.* [23] reported that, for the alloy $Ni_{48.8}Mn_{29.7}Ga_{21.5}$, there exists a cubic to orthorhombic A-M phase transformation, for which the subcells number in the super structure arising along $(110)[110]_m$ system is 7. Kokorin *et al.* also recently reported an intermartensitic phase transition for $Ni_{52}Mn_{24.4}Ga_{23.6}$ [35]. For the samples used in our experiment, which have nominal atomic composition of $Ni_{50}Mn_{27}Ga_{23}$, the A-M phase transformation appears to be only cubic to tetragonal. This was verified by the observing sample surface microsturcture during phase transformation process. In addition, differential scanning calorimeter (DSC) measurements show there is no intermartensite phase during phase transformation.

The Curie temperature of $Ni_{50}Mn_{27}Ga_{23}$ used in our experiments is much higher than room temperature. At room temperature and below, both austenite and martensite material are ferromagnetic. Based on the experimental measurements by Tickle [28], the saturation magnetization of $Ni_{51.3}Mn_{24.0}Ga_{24.7}$ is $m_s \approx 485$ emu/cm^3 for austenite at room temperature and $m_s \approx 602$ emu/cm^3 for martensite at -17 ^{o}C. These results are slightly smaller than our measurement on $Ni_{50}Mn_{27}Ga_{23}$ alloy. For $Ni_{50}Mn_{27}Ga_{23}$

material, the saturation magnetization of is $m_s \approx 548$ emu/cm^3 for austenite at room temperature and $m_s \approx 620$ emu/cm^3 for martensite at -5 ^{o}C without any stress applied. Another important magnetic parameter is the magnetic anisotropy constant, from Tickle's work, it is known that the martensitic magnetic anisotropy constant is $K_u = 2.45 \times 10^6$ ergs/cm^3 for $Ni_{51.3}Mn_{24.0}Ga_{24.7}$, which is about 100 times magnitude of austenite anisotropy constant. After measuring, the density of $Ni_{50}Mn_{27}Ga_{23}$ is obtained as 8.02 g/cm^3 from our preliminary work, which is same as the result of $Ni_{51.3}Mn_{24.0}Ga_{24.7}$.

The lattice parameters of austenite and martensite nickel-manganese-gallium alloy was first measured by Zasimchuk *et al* [36]. For the sample used here, the lattice parameters a_0, a and c are:

$$a_0 = 5.82\text{Å}, \quad a = 5.92\text{Å}, \quad c = 5.57\text{Å}, \tag{2.33}$$

where a_0 is lattice parameter of FCC austenite and a and c are lattice parameters of BCT martensite. The theoretical maximum phase transformation strains for compression and tension are

$$\varepsilon^C = \frac{c - a_0}{a_0} = -0.0430; \quad \varepsilon^T = \frac{a - a_0}{a_0} = 0.0172. \tag{2.34}$$

Figure 2.9 shows the differential scanning calorimeter (DSC) phase transformation process data of $Ni_{50}Mn_{27}Ga_{23}$ sample used to perform experiments in this thesis [37], without any applied stress or magnetic field. For the DSC measurement, the temperature rate was set as 10^{o}C/min. From the DSC data, it is known that the phase transformation temperatures and the latent heats for $Ni_{50}Mn_{27}Ga_{23}$ are:

$$\begin{aligned} &M_s = 6.0^o\text{C}, \quad M_f = 2.0^o\text{C}, \\ &A_s = 8.3^o\text{C}, \quad A_f = 12.1^o\text{C}, \\ &{Q_L}^C = -19\text{J/cm}^3, {Q_L}^H = 20\text{J/cm}^3, \end{aligned} \tag{2.35}$$

where M_s and M_f are the martensite start and finish temperatures, A_s and A_f are the austenite start and finish temperatures and ${Q_L}^C$ and ${Q_L}^H$ are the latent heats for cooling and heating phase transformation processes respectively.

2.5.3 Austenite-Martensite Interfaces for Ni_2MnGa Material

The results of A-M interface calculations in Section 2.4, using the lattice parameters for $Ni_{50}Mn_{27}Ga_{23}$ (2.33) are given here. They are grouped into three sets of eight solutions by the variants involved. Each set of eight has four solutions that involve type I terms and four that involve type II terms. There are two distinct solutions to which the cubic point group is apprised to generate these instances.

The solutions of A=3 and B=1 in (2.29) and (2.30) are shown below.
For κ_1=1 and κ_2=1, twins are Type I and it is found that $\lambda = 0.31$ and:

$$\mathbf{n} = \begin{pmatrix} 0.707 \\ 0.000 \\ \overline{0.707} \end{pmatrix}, \mathbf{a} = \begin{pmatrix} 0.082 \\ 0.000 \\ 0.087 \end{pmatrix}, \mathbf{m} = \begin{pmatrix} \overline{0.734} \\ 0.679 \\ 0.000 \end{pmatrix}, \mathbf{b} = \begin{pmatrix} 0.031 \\ 0.028 \\ 0.000 \end{pmatrix}. \tag{2.36}$$

For κ_1=1 and κ_2=1, twins are Type I and it is found that $\lambda = 0.69$ and:

$$\mathbf{n} = \begin{pmatrix} 0.707 \\ 0.000 \\ \overline{0.707} \end{pmatrix}, \mathbf{a} = \begin{pmatrix} 0.082 \\ 0.000 \\ 0.087 \end{pmatrix}, \mathbf{m} = \begin{pmatrix} 0.000 \\ 0.679 \\ \overline{0.734} \end{pmatrix}, \mathbf{b} = \begin{pmatrix} 0.000 \\ 0.028 \\ 0.031 \end{pmatrix}. \tag{2.37}$$

For κ_1=1 and κ_2=-1, twins are Type I and it is found that $\lambda = 0.31$ and:

$$\mathbf{n} = \begin{pmatrix} 0.707 \\ 0.000 \\ \overline{0.707} \end{pmatrix}, \mathbf{a} = \begin{pmatrix} 0.082 \\ 0.000 \\ 0.087 \end{pmatrix}, \mathbf{m} = \begin{pmatrix} \overline{0.734} \\ \overline{0.679} \\ 0.000 \end{pmatrix}, \mathbf{b} = \begin{pmatrix} 0.031 \\ \overline{0.028} \\ 0.000 \end{pmatrix}. \tag{2.38}$$

For κ_1=1 and κ_2=-1, twins are Type I and it is found that $\lambda = 0.69$ and:

$$\mathbf{n} = \begin{pmatrix} 0.707 \\ 0.000 \\ \overline{0.707} \end{pmatrix}, \mathbf{a} = \begin{pmatrix} 0.082 \\ 0.000 \\ 0.087 \end{pmatrix}, \mathbf{m} = \begin{pmatrix} 0.000 \\ \overline{0.679} \\ \overline{0.734} \end{pmatrix}, \mathbf{b} = \begin{pmatrix} 0.000 \\ \overline{0.028} \\ 0.031 \end{pmatrix}. \tag{2.39}$$

For κ_1=-1 and κ_2=1, twins are Type II and it is found that $\lambda = 0.31$ and:

$$\mathbf{n} = \begin{pmatrix} \overline{0.707} \\ 0.000 \\ \overline{0.707} \end{pmatrix}, \mathbf{a} = \begin{pmatrix} \overline{0.082} \\ 0.000 \\ 0.087 \end{pmatrix}, \mathbf{m} = \begin{pmatrix} \overline{0.734} \\ 0.679 \\ 0.000 \end{pmatrix}, \mathbf{b} = \begin{pmatrix} 0.031 \\ 0.028 \\ 0.000 \end{pmatrix}. \tag{2.40}$$

For κ_1=-1 and κ_2=1, twins are Type II and it is found that $\lambda = 0.69$ and:

$$\mathbf{n} = \begin{pmatrix} \overline{0.707} \\ 0.000 \\ \overline{0.707} \end{pmatrix}, \mathbf{a} = \begin{pmatrix} \overline{0.082} \\ 0.000 \\ 0.087 \end{pmatrix}, \mathbf{m} = \begin{pmatrix} 0.000 \\ 0.679 \\ \overline{0.734} \end{pmatrix}, \mathbf{b} = \begin{pmatrix} 0.000 \\ 0.028 \\ 0.031 \end{pmatrix}. \tag{2.41}$$

For κ_1=-1 and κ_2=-1, twins are Type II and it is found that $\lambda = 0.31$ and:

$$\mathbf{n} = \begin{pmatrix} \overline{0.707} \\ 0.000 \\ \overline{0.707} \end{pmatrix}, \mathbf{a} = \begin{pmatrix} \overline{0.082} \\ 0.000 \\ 0.087 \end{pmatrix}, \mathbf{m} = \begin{pmatrix} \overline{0.734} \\ \overline{0.679} \\ 0.000 \end{pmatrix}, \mathbf{b} = \begin{pmatrix} 0.031 \\ \overline{0.028} \\ 0.000 \end{pmatrix}. \tag{2.42}$$

For κ_1=-1 and κ_2=-1, twins are Type II and it is found that $\lambda = 0.69$ and:

$$\mathbf{n} = \begin{pmatrix} \overline{0.707} \\ 0.000 \\ \overline{0.707} \end{pmatrix}, \mathbf{a} = \begin{pmatrix} \overline{0.082} \\ 0.000 \\ 0.087 \end{pmatrix}, \mathbf{m} = \begin{pmatrix} 0.000 \\ \overline{0.679} \\ \overline{0.734} \end{pmatrix}, \mathbf{b} = \begin{pmatrix} 0.000 \\ \overline{0.028} \\ 0.031 \end{pmatrix}. \tag{2.43}$$

The solutions of A=2 and B=3 in (2.29) and (2.30) are shown below.

For κ_1=1 and κ_2=1, twins are Type I and it is found that $\lambda = 0.31$ and:

$$\mathbf{n} = \begin{pmatrix} 0.000 \\ 0.707 \\ \overline{0.707} \end{pmatrix}, \mathbf{a} = \begin{pmatrix} 0.000 \\ 0.082 \\ 0.087 \end{pmatrix}, \mathbf{m} = \begin{pmatrix} 0.679 \\ \overline{0.734} \\ 0.000 \end{pmatrix}, \mathbf{b} = \begin{pmatrix} 0.028 \\ 0.031 \\ 0.000 \end{pmatrix}. \tag{2.44}$$

For κ_1=1 and κ_2=1, twins are Type I and it is found that $\lambda = 0.69$ and:

$$\mathbf{n} = \begin{pmatrix} 0.000 \\ 0.707 \\ \overline{0.707} \end{pmatrix}, \mathbf{a} = \begin{pmatrix} 0.000 \\ 0.082 \\ 0.087 \end{pmatrix}, \mathbf{m} = \begin{pmatrix} 0.679 \\ 0.000 \\ \overline{0.734} \end{pmatrix}, \mathbf{b} = \begin{pmatrix} 0.028 \\ 0.000 \\ 0.031 \end{pmatrix}. \tag{2.45}$$

For κ_1=1 and κ_2=-1, twins are Type I and it is found that $\lambda = 0.31$ and:

$$\mathbf{n} = \begin{pmatrix} 0.000 \\ 0.707 \\ \overline{0.707} \end{pmatrix}, \mathbf{a} = \begin{pmatrix} 0.000 \\ 0.082 \\ 0.087 \end{pmatrix}, \mathbf{m} = \begin{pmatrix} \overline{0.679} \\ \overline{0.734} \\ 0.000 \end{pmatrix}, \mathbf{b} = \begin{pmatrix} \overline{0.028} \\ 0.031 \\ 0.000 \end{pmatrix}. \tag{2.46}$$

For κ_1=1 and κ_2=-1, twins are Type I and it is found that $\lambda = 0.69$ and:

$$\mathbf{n} = \begin{pmatrix} 0.000 \\ 0.707 \\ \overline{0.707} \end{pmatrix}, \mathbf{a} = \begin{pmatrix} 0.000 \\ 0.082 \\ 0.087 \end{pmatrix}, \mathbf{m} = \begin{pmatrix} \overline{0.679} \\ 0.000 \\ \overline{0.734} \end{pmatrix}, \mathbf{b} = \begin{pmatrix} \overline{0.028} \\ 0.000 \\ 0.031 \end{pmatrix}. \tag{2.47}$$

For κ_1=-1 and κ_2=1, twins are Type II and it is found that $\lambda = 0.31$ and:

$$\mathbf{n} = \begin{pmatrix} 0.000 \\ \overline{0.707} \\ \overline{0.707} \end{pmatrix}, \mathbf{a} = \begin{pmatrix} 0.000 \\ \overline{0.082} \\ 0.087 \end{pmatrix}, \mathbf{m} = \begin{pmatrix} 0.679 \\ \overline{0.734} \\ 0.000 \end{pmatrix}, \mathbf{b} = \begin{pmatrix} 0.028 \\ 0.031 \\ 0.000 \end{pmatrix}. \tag{2.48}$$

For κ_1=-1 and κ_2=1, twins are Type II and it is found that $\lambda = 0.69$ and:

$$\mathbf{n} = \begin{pmatrix} 0.000 \\ \overline{0.707} \\ \overline{0.707} \end{pmatrix}, \mathbf{a} = \begin{pmatrix} 0.000 \\ \overline{0.082} \\ 0.087 \end{pmatrix}, \mathbf{m} = \begin{pmatrix} 0.679 \\ 0.000 \\ \overline{0.734} \end{pmatrix}, \mathbf{b} = \begin{pmatrix} 0.028 \\ 0.000 \\ 0.031 \end{pmatrix}. \tag{2.49}$$

For κ_1=-1 and κ_2=-1, twins are Type II and it is found that $\lambda = 0.31$ and:

$$\mathbf{n} = \begin{pmatrix} 0.000 \\ \overline{0.707} \\ \overline{0.707} \end{pmatrix}, \mathbf{a} = \begin{pmatrix} 0.000 \\ \overline{0.082} \\ 0.087 \end{pmatrix}, \mathbf{m} = \begin{pmatrix} \overline{0.679} \\ \overline{0.734} \\ 0.000 \end{pmatrix}, \mathbf{b} = \begin{pmatrix} \overline{0.028} \\ 0.031 \\ 0.000 \end{pmatrix}. \tag{2.50}$$

For κ_1=-1 and κ_2=-1, twins are Type II and it is found that $\lambda = 0.69$ and:

$$\mathbf{n} = \begin{pmatrix} 0.000 \\ \overline{0.707} \\ \overline{0.707} \end{pmatrix}, \mathbf{a} = \begin{pmatrix} 0.000 \\ \overline{0.082} \\ 0.087 \end{pmatrix}, \mathbf{m} = \begin{pmatrix} \overline{0.679} \\ 0.000 \\ \overline{0.734} \end{pmatrix}, \mathbf{b} = \begin{pmatrix} \overline{0.028} \\ 0.000 \\ 0.031 \end{pmatrix}. \tag{2.51}$$

The solutions of A=1 and B=2 in (2.29) and (2.30) are shown below.

For κ_1=1 and κ_2=1, twins are Type I and it is found that $\lambda = 0.31$ and:

$$\mathbf{n} = \begin{pmatrix} \overline{0.707} \\ 0.707 \\ 0.000 \end{pmatrix}, \mathbf{a} = \begin{pmatrix} 0.087 \\ 0.082 \\ 0.000 \end{pmatrix}, \mathbf{m} = \begin{pmatrix} 0.000 \\ \overline{0.734} \\ 0.679 \end{pmatrix}, \mathbf{b} = \begin{pmatrix} 0.000 \\ 0.031 \\ 0.028 \end{pmatrix}. \tag{2.52}$$

For κ_1=1 and κ_2=1, twins are Type I and it is found that $\lambda = 0.69$ and:

$$\mathbf{n} = \begin{pmatrix} \overline{0.707} \\ 0.707 \\ 0.000 \end{pmatrix}, \mathbf{a} = \begin{pmatrix} 0.087 \\ 0.082 \\ 0.000 \end{pmatrix}, \mathbf{m} = \begin{pmatrix} \overline{0.734} \\ 0.000 \\ 0.679 \end{pmatrix}, \mathbf{b} = \begin{pmatrix} 0.031 \\ 0.000 \\ 0.028 \end{pmatrix}. \tag{2.53}$$

For κ_1=1 and κ_2=-1, twins are Type I and it is found that $\lambda = 0.31$ and:

$$\mathbf{n} = \begin{pmatrix} \overline{0.707} \\ 0.707 \\ 0.000 \end{pmatrix}, \mathbf{a} = \begin{pmatrix} 0.087 \\ 0.082 \\ 0.000 \end{pmatrix}, \mathbf{m} = \begin{pmatrix} 0.000 \\ \overline{0.734} \\ \overline{0.679} \end{pmatrix}, \mathbf{b} = \begin{pmatrix} 0.000 \\ 0.031 \\ \overline{0.028} \end{pmatrix}. \tag{2.54}$$

For κ_1=1 and κ_2=-1, twins are Type I and it is found that $\lambda = 0.69$ and:

$$\mathbf{n} = \begin{pmatrix} \overline{0.707} \\ 0.707 \\ 0.000 \end{pmatrix}, \mathbf{a} = \begin{pmatrix} 0.087 \\ 0.082 \\ 0.000 \end{pmatrix}, \mathbf{m} = \begin{pmatrix} \overline{0.734} \\ 0.000 \\ \overline{0.679} \end{pmatrix}, \mathbf{b} = \begin{pmatrix} 0.031 \\ 0.000 \\ \overline{0.028} \end{pmatrix}. \tag{2.55}$$

For κ_1=-1 and κ_2=1, twins are Type II and it is found that $\lambda = 0.31$ and:

$$\mathbf{n} = \begin{pmatrix} \overline{0.707} \\ \overline{0.707} \\ 0.000 \end{pmatrix}, \mathbf{a} = \begin{pmatrix} 0.087 \\ \overline{0.082} \\ 0.000 \end{pmatrix}, \mathbf{m} = \begin{pmatrix} 0.000 \\ \overline{0.734} \\ 0.679 \end{pmatrix}, \mathbf{b} = \begin{pmatrix} 0.000 \\ 0.031 \\ 0.028 \end{pmatrix}. \tag{2.56}$$

For κ_1=-1 and κ_2=1, twins are Type II and it is found that $\lambda = 0.69$ and:

$$\mathbf{n} = \begin{pmatrix} \overline{0.707} \\ \overline{0.707} \\ 0.000 \end{pmatrix}, \mathbf{a} = \begin{pmatrix} 0.087 \\ \overline{0.082} \\ 0.000 \end{pmatrix}, \mathbf{m} = \begin{pmatrix} \overline{0.734} \\ 0.000 \\ 0.679 \end{pmatrix}, \mathbf{b} = \begin{pmatrix} 0.031 \\ 0.000 \\ 0.028 \end{pmatrix}. \tag{2.57}$$

For κ_1=-1 and κ_2=-1, twins are Type II and it is found that $\lambda = 0.31$ and:

$$\mathbf{n} = \begin{pmatrix} \overline{0.707} \\ \overline{0.707} \\ 0.000 \end{pmatrix}, \mathbf{a} = \begin{pmatrix} 0.087 \\ \overline{0.082} \\ 0.000 \end{pmatrix}, \mathbf{m} = \begin{pmatrix} 0.000 \\ \overline{0.734} \\ \overline{0.679} \end{pmatrix}, \mathbf{b} = \begin{pmatrix} 0.000 \\ 0.031 \\ \overline{0.028} \end{pmatrix}. \tag{2.58}$$

For κ_1=-1 and κ_2=-1, twins are Type II and it is found that $\lambda = 0.69$ and:

$$\mathbf{n} = \begin{pmatrix} \overline{0.707} \\ \overline{0.707} \\ 0.000 \end{pmatrix}, \mathbf{a} = \begin{pmatrix} 0.087 \\ \overline{0.082} \\ 0.000 \end{pmatrix}, \mathbf{m} = \begin{pmatrix} \overline{0.734} \\ 0.000 \\ \overline{0.679} \end{pmatrix}, \mathbf{b} = \begin{pmatrix} 0.031 \\ 0.000 \\ \overline{0.028} \end{pmatrix}. \tag{2.59}$$

If specific cooling or heating phase transformation conditions are considered, the specific A-M boundary and martensite twins microstructure will be determined by the loadings, because the favored microstructure is determined by the applied stress and magnetic field. For example, when the sample is in applied uniaxial tension along [001] direction, from (2.32), the stretch matrices $\mathbf{U}_1$ and $\mathbf{U}_2$ are equally favored, and thus only the A-M interfaces in (2.52-2.59) will be present in the sample under this loading condition.

Because only one surface of the sample can be observed during experiments, even if the favored stretch matrices are known, this may not allow the specific solution (2.36)-(2.59) to be determined. An example is shown in Figure 2.10. All four microstructures appear the same if they are observed on a (100) plane.

2.5.4 Ferromagnetic Shape Memory Mechanism of Ni_2MnGa Material

For ferromagnetic materials that undergo the shape memory transformation process, the variants of microstructure may not only be biased by the applied load, but also by the applied magnetic field. There are three possible mechanisms that can produce a shape change when a magnetic field is applied to a ferromagnetic sample that undergoes a reversible austenite-martensite phase transformation.

First, the application of the magnetic field to the austenite phase can induce the phase transformation, similar to iron-nickel [38]. This kind of mechanism typically requires a very large field. This effect is partially due to the large difference in the saturation magnetizations of the austenite and martensite phases [39]. Some research on this mechanism in Ni_2MnGa are introduced in Chapter 1. Additional measurements of this effect will be presented later.

Second, the applied magnetic field can rotate the spontaneous magnetization related with the crystal lattice [40], resulting in conventional magnetostriction. This does not involve a phase transformation and typically results in very small strains. While this effect is probably present to some amount in Ni_2MnGa, it is neglectable compared to the third mechanism, variant rearrangement, and will not be considered here.

Third, an applied magnetic field can rearrange martensite variants in the same manner as stress as shown in Figure 2.7. This gives rise to the ferromagnetic shape memory (FSM) effect, which is the primary focus of this thesis. For tetragonal Ni_2MnGa, with

an easy axis in the short c lattice direction, the FSM effect works as shown in Figure 2.11 [41]. In the figure, step 1 shows the variants in the tetragonal (martensite) phase, arrows show the spontaneous magnetization directions of variants; step 2 shows the actuation is accomplished by using an applied magnetic field to offset the effect of the compression. Martensite twins with compatible magnetization directions are shown in step 3 and step 4. The microstructure of ferromagnetic shape memory alloy (FSMA) can be further rearranged and controlled by the applied magnetic field in step 5 and step 6. Note that the field that opposes the compressive stress is in the direction that has the largest demagnetization factor (the short sample direction) and thus a given field has a smaller effect. For applied tension, the situation is reversed and thus larger work output may be possible in this case.

The rearrangement of variants by applied magnetic field can produce large strains, and this large strain is the so called magnetic field induced strain (MFIS). This mechanism requires high mobility of the twin boundaries between variants and a large magnetic anisotropy (K_u) to constrain the spontaneous magnetization along the easy axis of variant. This constraint is necessary to generate enough driving force on the twin boundaries by the applied magnetic field to overcome the applied stress and cause variant rearrangement.

In Figure 2.12, a comparison of low and high magnetic anisotropy materials is shown. Here, the criterion from O'Handley's work [13] is used to quantify the effect by comparing Zeeman energy and the magnetic anisotropy energy. If $h_a = \mathbf{H} \cdot \mathbf{M}_s / K_u \ll 1$, that is to say the magnetic anisotropy energy, K_u is much larger than the Zeeman energy, $\mathbf{H} \cdot \mathbf{M}_s$, the material is said to have high magnetic anisotropy. If $h_a = \mathbf{H} \cdot \mathbf{M}_s / K_u \gg 1$, that is, the magnetic anisotropy energy, K_u is much smaller than the Zeeman energy, $\mathbf{H} \cdot \mathbf{M}_s$, the material is said to have low magnetic anisotropy. Otherwise, the material is called with intermediate magnetic anisotropy.

If the applied horizontal magnetic field, $\mathbf{H}_h$, is increased from 0 (top) to saturation

(bottom), as shown in Figure 2.12, without the large magnetic isotropy energy and mobile twin boundaries, variant rearrangement will not happen, and there will only be a much smaller shape change due to magnetostriction [13]. In the case of high magnetic anisotropy energy, and low applied stress, variants rearrangement will be preferred. But when the applied stress level is so high that the variants rearrangement is prevented, magnetization rotation is preferred energetically, and the applied stress is said to be the *blocking stress*. Under the blocking stress, the MFIS is very small, and the work output is relatively small. The blocking stress of an FSMA is an important parameter for the design of actuator [25].

The alloys, Ni_2MnGa and Fe_7Pd_3, are two common materials observed to exhibit the FSM effect at ordinary magnetic fields [44]. And Ni_2MnGa exhibits a giant MFIS (0.058 in tetragonal and 0.094 in orthorhombic) compared to less than 0.01 of Fe_7Pd_3, which makes Ni_2MnGa preferred for use in actuators and sensors.

2.5.5 A Simple Theoretical Model of Ni_2MnGa FSMA

In order to model the magneto-mechanical mechanism, in particular, the magnetic field induced strain under different stress and applied magnetic field, for comparison to experimental results and evaluation of the various parts of ferromagnetic shape memory mechanism, a simple model is presented next.

The simple lumped phase model is shown in Figure 2.13. The martensite of a single crystal sample is assumed to be two variants, each one is assumed to be a single magnetic domain, with spontaneous magnetization at angles θ_1 and θ_2 from the easy axis. The volume fraction of one variant is λ, and then the other is 1-λ. The strains of variants, ε_1 and ε_2, will be calculated directly from the martensitic lattice parameters a and c of Ni_2MnGa. So the total free energy of the single crystal sample under applied magnetic field and dead load can be minimized by varying θ_1, θ_2 and λ for a given applied field and uniaxial stress. Here the mechanical work done by the dead load, the magnetic

energies in (2.26) are minimized, but twins boundary energy is ignored. In order to include twin boundary energy, the model would have to predict the number of twin interfaces on the material and this is beyond the scope of this work.

2.6 Effects of Stress and Magnetic Field on Phase Transformation

The reversible diffusionless austenite-martensite phase transformation is the main shape memory mechanism on Ni_2MnGa alloy. Both load and magnetic field applied on the material will influence the phase transformation process and change the phase transformation temperature. The influence of loading conditions, including stress and magnetic field, on the irreversible phase transformation between austenite and martensite has been studied from the 1960's. At that time, the first studied material was steel, followed by FeNi, FeNiCoTi alloys. Shimizu [42] reviewed the previous results on effects of stresses and magnetic field on martensite phase transformations. In order to understand the effects of stress and magnetic field on Ni_2MnGa phase transformation temperatures, the theoretical analysis in the work of Cui *et al.* [19] will be used. This theory will be summarized next.

2.6.1 Effect of Stress on Phase Transformation Temperatures

The relation between stress and changes of transforamtion temperature can be explained using the Clausius-Clapeyron (C-C) equation (derivation of the equation can be found in the paper by Patel and Cohen [46] and the book by Ericksen [43]),

$$\frac{\partial \sigma_M^*}{\partial \theta_c} = -\frac{Q_L}{\varepsilon^{PT} \theta_c}, \tag{2.60}$$

where σ_M^* is the dead load during the transformation, θ_c is the phase transformation temperature (assuming there is no hysteresis such that martensite start, martensite finish, austenite start and austenite finish temperatures are same, and the cooling or

heating is sufficiently slow such that the sample is in equilibrium throughout the test). The latent heat is Q_L, ε^{PT} is the transformation strain. This result assumes the applied stress is sufficiently large to result in a transformation to a single variant and thus it may not work well at small stress levels. If the martensite is not a single variant, then the volume fractions of the variants would have to be known. While transformation under large stresses probably does not result in a pure single variant state, it will be close enough to reasonably predict the slope of transformation temperature versus stress for Ni_2MnGa alloy.

2.6.2 Effect of Magnetic Field on Phase Transformation Temperatures

The effect of magnetic fields on the phase transformation temperatures can also be explained by a magnetic version of C-C equation. Consider the free energy density of a Ni_2MnGa sample under both load and magnetic field,

$$\Psi(\varepsilon(\mathbf{H}_0,\sigma),\mathbf{M}(\mathbf{H}_0,\sigma),\theta)-\mathbf{H}_0\cdot\mathbf{M}(\mathbf{H}_0,\sigma)\mathrm{det}\mathbf{U}-\sigma\cdot\varepsilon(\mathbf{H}_0,\sigma)+\frac{1}{2}\mathbf{M}\cdot\mathbf{DM}, \quad (2.61)$$

where $\varepsilon(\mathbf{H}_0,\sigma)$ is the strain of the specimen; $\mathbf{M}(\mathbf{H}_0,\sigma)$ is the spontaneous magnetization of the specimen; θ is the temperature of the sample. All variables mentioned above except temperature are function of independent variables: $\mathbf{H}_0 = h\mathbf{e}_h$, which is the applied magnetic field, and σ, the applied stress. The term $\mathbf{M}\cdot\mathbf{DM}/2$ is the demagnetization energy of the domain with a uniform $\mathbf{M}$, and $\mathbf{D}$ is the demagnetization matrix of the domain. It is assumed constant during the phase transformation by assuming the shape changes of the sample in austenite state and in martensite state are small.

Let θ_c denote the critical temperature and σ^* denotes the critical stress at which the phase transformation occurs. If the temperature θ in (2.61) is evaluated at θ_c, then θ depends on the two variables $\mathbf{H}_0$ and σ. The partial derivatives of (2.61) with respect to the magnitude of the applied magnetic field are the same for both austenite and martensite,

$$\frac{\partial\Psi(\varepsilon_\mathrm{A},\mathbf{M}_\mathrm{A},\theta_c)}{\partial\varepsilon_\mathrm{A}}\frac{\partial\varepsilon_\mathrm{A}}{\partial h}+\frac{\partial\Psi(\varepsilon_\mathrm{A},\mathbf{M}_\mathrm{A},\theta_c)}{\partial\mathbf{M}_\mathrm{A}}\frac{\partial\mathbf{M}_\mathrm{A}}{\partial h}+\frac{\partial\Psi(\varepsilon_\mathrm{A},\mathbf{M}_\mathrm{A},\theta_c)}{\partial\theta_c}\frac{\partial\theta_c}{\partial h}-$$

$$\mathbf{e}_h \cdot \mathbf{M}_\mathrm{A}\mathrm{det}\mathbf{U}_\mathrm{A} - \mathbf{H}_0 \cdot \frac{\partial(\mathbf{M}_\mathrm{A}\mathrm{det}\mathbf{U}_\mathrm{A})}{\partial h} - \sigma^*_\mathrm{A} \cdot \frac{\partial \varepsilon_\mathrm{A}}{\partial h} + \frac{1}{2}\frac{\partial(\mathbf{M}_\mathrm{A} \cdot \mathbf{DM}_\mathrm{A})}{\partial \mathrm{h}} =$$
$$\frac{\partial \Psi(\varepsilon_\mathrm{M}, \mathbf{M}_\mathrm{M}, \theta_c)}{\partial \varepsilon_\mathrm{M}}\frac{\partial \varepsilon_\mathrm{M}}{\partial h} + \frac{\partial \Psi(\varepsilon_\mathrm{M}, \mathbf{M}_\mathrm{M}, \theta_c)}{\partial \mathbf{M}_\mathrm{M}}\frac{\partial \mathbf{M}_\mathrm{M}}{\partial h} + \frac{\partial \Psi(\varepsilon_\mathrm{M}, \mathbf{M}_\mathrm{M}, \theta_c)}{\partial \theta_c}\frac{\partial \theta_c}{\partial h} -$$
$$\mathbf{e}_h \cdot \mathbf{M}_\mathrm{M}\mathrm{det}\mathbf{U}_\mathrm{M} - \mathbf{H}_0 \cdot \frac{\partial(\mathbf{M}_\mathrm{M}\mathrm{det}\mathbf{U}_\mathrm{M})}{\partial h} - \sigma^*_\mathrm{M} \cdot \frac{\partial \varepsilon_\mathrm{M}}{\partial h} + \frac{1}{2}\frac{\partial(\mathbf{M}_\mathrm{M} \cdot \mathbf{DM}_\mathrm{M})}{\partial \mathrm{h}} \quad (2.62)$$

where ε_A and ε_M are the strain at which the martensite transition starts and finishes; $\mathbf{M}_\mathrm{A}$ and $\mathbf{M}_\mathrm{M}$ are the average spontaneous magnetization of the austenite and martensite of the specimen; σ^*_A and σ^*_M are the dead loads at which the martensite transition starts and finishes; det$\mathbf{U}_\mathrm{A}$ and det$\mathbf{U}_\mathrm{M}$ are the determinants of the stretch tensors of austenite and martensite. To simplify the situation, assume the austenite transforms into single variant martensite which is favored by the dead loads. Then det$\mathbf{U}_\mathrm{A}$=1 and det$\mathbf{U}_\mathrm{M}$= det$\mathbf{U}_1$. In addition, when the austenite and martensite are in equilibrium,

$$\frac{\partial}{\partial \mathbf{M}_\mathrm{A}}(\Psi(\varepsilon_\mathrm{A}, \mathbf{M}_\mathrm{A}, \theta_c) - \mathbf{H}_0 \cdot \mathbf{M}_\mathrm{A}(\mathbf{H}_0, \sigma) - \sigma \cdot \varepsilon(\mathbf{H}_0, \sigma) + \frac{1}{2}\mathbf{M}_\mathrm{A} \cdot \mathbf{DM}_\mathrm{A}) = 0, \quad (2.63)$$

which reduces to

$$\frac{\partial}{\partial \mathbf{M}_\mathrm{A}}\Psi(\varepsilon_\mathrm{A}, \mathbf{M}_\mathrm{A}, \theta_c) = \mathbf{H}_0 + \mathbf{DM}_\mathrm{A}. \quad (2.64)$$

Similarly, for the martensite

$$\frac{\partial}{\partial \mathbf{M}_\mathrm{M}}\Psi(\varepsilon_\mathrm{M}, \mathbf{M}_\mathrm{M}, \theta_c) = \mathbf{H}_0\mathrm{det}\mathbf{U}_1 + \mathbf{DM}_\mathrm{M}. \quad (2.65)$$

In addition,

$$\frac{\partial \Psi(\varepsilon_\mathrm{A}, \mathbf{M}_\mathrm{A}, \theta_c)}{\partial \varepsilon_\mathrm{A}} = \sigma^*_\mathrm{A}, \quad \frac{\partial \Psi(\varepsilon_\mathrm{M}, \mathbf{M}_\mathrm{M}, \theta_c)}{\partial \varepsilon_\mathrm{M}} = \sigma^*_\mathrm{M}. \quad (2.66)$$

Then (2.62) becomes

$$\frac{\partial \Psi(\varepsilon_\mathrm{A}, \mathbf{M}_\mathrm{A}, \theta_c)}{\partial \theta_c}\frac{\partial \theta_c}{\partial h} - \mathbf{e}_h \cdot \mathbf{M}_\mathrm{A} = \frac{\partial \Psi(\varepsilon_\mathrm{M}, \mathbf{M}_\mathrm{M}, \theta_c)}{\partial \theta_c}\frac{\partial \theta_c}{\partial h} - \mathbf{e}_h \cdot \mathbf{M}_\mathrm{M}\ \mathrm{det}\mathbf{U}_1. \quad (2.67)$$

Furthermore, define

$$\eta_\mathrm{A} = -\frac{\partial \Psi(\varepsilon_\mathrm{A}, \mathbf{M}_\mathrm{A}, \theta_c)}{\theta_c}, \quad \eta_\mathrm{M} = -\frac{\partial \Psi(\varepsilon_\mathrm{M}, \mathbf{M}_\mathrm{M}, \theta_c)}{\theta_c}, \quad (2.68)$$

which are the entropy of austenite and martensite at critical temperature θ_c, stress σ^*, and magnetization $\mathbf{M}_\mathrm{A}$, and $\mathbf{M}_\mathrm{M}$, respectively. If the stress and magnetic field are zero, then the entropy difference between the martensite and austenite is the latent heat divided by the temperature Q_L/θ_c. Substitution of (2.68) into (2.67) gives

$$\frac{\partial \theta_c}{\partial h} = \frac{-\mathbf{e}_h \cdot (\mathbf{M}_\mathrm{M}\mathrm{det}\mathbf{U}_1 - \mathbf{M}_\mathrm{A})}{\eta_\mathrm{M} - \eta_\mathrm{A}} = -\frac{\mathbf{e}_h \cdot [|\mathbf{M}|]}{\eta_\mathrm{M} - \eta_\mathrm{A}}, \quad (2.69)$$

where $[|\mathbf{M}|]$ represents the jump of the magnetization during the martensitic phase transformation. This jump depends on many factors, such as the microstructures and magnetic domains of the martensite and austenite, the shape of the sample, the stress, and the applied magnetic field, etc.

Table 2.1: There are seven point groups for a Bravais lattice.

Symmetric type	Rotations
Triclinic	$\mathbf{I}$.
Monoclinic	$\mathbf{I}$, $\mathbf{R}(\mathbf{e}_3, \pi)$.
Orthorhombic	$\mathbf{I}$, $\mathbf{R}(\mathbf{e}_1, \pi)$, $\mathbf{R}(\mathbf{e}_2, \pi)$, $\mathbf{R}(\mathbf{e}_3, \pi)$.
Tetragonal	$\mathbf{I}$, $\mathbf{R}(\mathbf{e}_3, \pi/2)$, $\mathbf{R}(\mathbf{e}_3, \pi)$, $\mathbf{R}(\mathbf{e}_3, 3\pi/2)$, $\mathbf{R}(\mathbf{e}_1, \pi)$,$\mathbf{R}(\mathbf{e}_2, \pi)$, $\mathbf{R}(\frac{\mathbf{e}_1+\mathbf{e}_2}{\sqrt{2}}, \pi)$, $\mathbf{R}(\frac{\mathbf{e}_1-\mathbf{e}_2}{\sqrt{2}}, \pi)$.
Cubic	$\mathbf{I}$, $\mathbf{R}(\mathbf{e}_1, \pi/2)$, $\mathbf{R}(\mathbf{e}_1, \pi)$, $\mathbf{R}(\mathbf{e}_1, 3\pi/2)$, $\mathbf{R}(\mathbf{e}_2, \pi/2)$, $\mathbf{R}(\mathbf{e}_2, \pi)$, $\mathbf{R}(\mathbf{e}_2, 3\pi/2)$, $\mathbf{R}(\mathbf{e}_3, \pi/2)$, $\mathbf{R}(\mathbf{e}_3, \pi)$, $\mathbf{R}(\mathbf{e}_3, 3\pi/2)$, $\mathbf{R}(\frac{\mathbf{e}_1+\mathbf{e}_2}{\sqrt{2}}, \pi)$, $\mathbf{R}(\frac{\mathbf{e}_1-\mathbf{e}_2}{\sqrt{2}}, \pi)$, $\mathbf{R}(\frac{\mathbf{e}_2+\mathbf{e}_3}{\sqrt{2}}, \pi)$, $\mathbf{R}(\frac{\mathbf{e}_2-\mathbf{e}_3}{\sqrt{2}}, \pi)$, $\mathbf{R}(\frac{\mathbf{e}_3+\mathbf{e}_1}{\sqrt{2}}, \pi)$, $\mathbf{R}(\frac{\mathbf{e}_3-\mathbf{e}_1}{\sqrt{2}}, \pi)$, $\mathbf{R}(\frac{\mathbf{e}_1+\mathbf{e}_2+\mathbf{e}_3}{\sqrt{3}}, 2\pi/3)$, $\mathbf{R}(\frac{-\mathbf{e}_1+\mathbf{e}_2+\mathbf{e}_3}{\sqrt{2}}, 2\pi/3)$, $\mathbf{R}(\frac{\mathbf{e}_1-\mathbf{e}_2+\mathbf{e}_3}{\sqrt{3}}, 2\pi/3)$, $\mathbf{R}(\frac{\mathbf{e}_1+\mathbf{e}_2-\mathbf{e}_3}{\sqrt{2}}, 2\pi/3)$, $\mathbf{R}(\frac{\mathbf{e}_1+\mathbf{e}_2+\mathbf{e}_3}{\sqrt{3}}, 4\pi/3)$, $\mathbf{R}(\frac{-\mathbf{e}_1+\mathbf{e}_2+\mathbf{e}_3}{\sqrt{2}}, 4\pi/3)$. $\mathbf{R}(\frac{\mathbf{e}_1-\mathbf{e}_2+\mathbf{e}_3}{\sqrt{3}}, 4\pi/3)$, $\mathbf{R}(\frac{\mathbf{e}_1+\mathbf{e}_2-\mathbf{e}_3}{\sqrt{2}}, 4\pi/3)$.
Trigonal	$\mathbf{I}$, $\mathbf{R}(\mathbf{e}_3, 2\pi/3)$, $\mathbf{R}(\mathbf{e}_3, 4\pi/3)$, $\mathbf{R}(\mathbf{e}_1, \pi)$, $\mathbf{R}(\frac{\mathbf{e}_1+\sqrt{3}\mathbf{e}_2}{2}, \pi)$, $\mathbf{R}(\frac{-\mathbf{e}_1+\sqrt{3}\mathbf{e}_2}{2}, \pi)$.
Hexagonal	$\mathbf{I}$, $\mathbf{R}(\mathbf{e}_3, \pi/3)$, $\mathbf{R}(\mathbf{e}_3, 2\pi/3)$, $\mathbf{R}(\mathbf{e}_3, \pi)$, $\mathbf{R}(\mathbf{e}_3, 4\pi/3)$, $\mathbf{R}(\mathbf{e}_3, 5\pi/3)$, $\mathbf{R}(\mathbf{e}_1, \pi)$, $\mathbf{R}(\mathbf{e}_2, \pi)$, $\mathbf{R}(\frac{\sqrt{3}\mathbf{e}_1+\mathbf{e}_2}{2}, \pi)$, $\mathbf{R}(\frac{\mathbf{e}_1+\sqrt{3}\mathbf{e}_2}{2}, \pi)$, $\mathbf{R}(\frac{-\sqrt{3}\mathbf{e}_1+\mathbf{e}_2}{2}, \pi)$, $\mathbf{R}(\frac{-\mathbf{e}_1+\sqrt{3}\mathbf{e}_2}{2}, \pi)$.

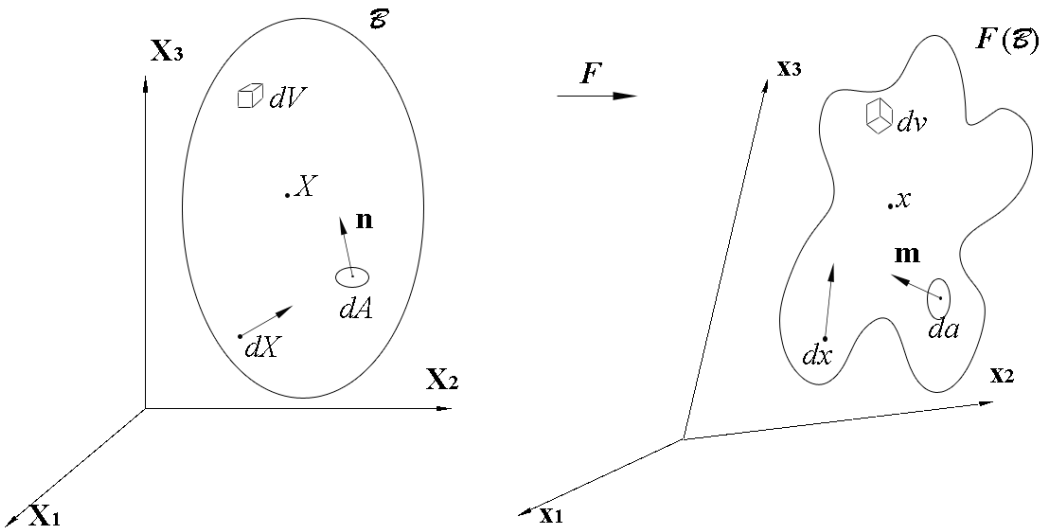

Figure 2.1: Deformation takes the left reference configuration to the right deformed configuration.

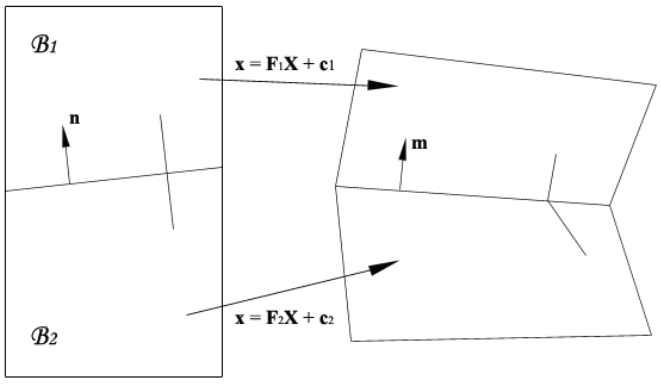

Figure 2.2: A piecewise homogeneous deformation satisfies kinematic compatibility condition across an interface that has normal **n** in the reference configuration and normal **m** in the deformed configuration, as shown.

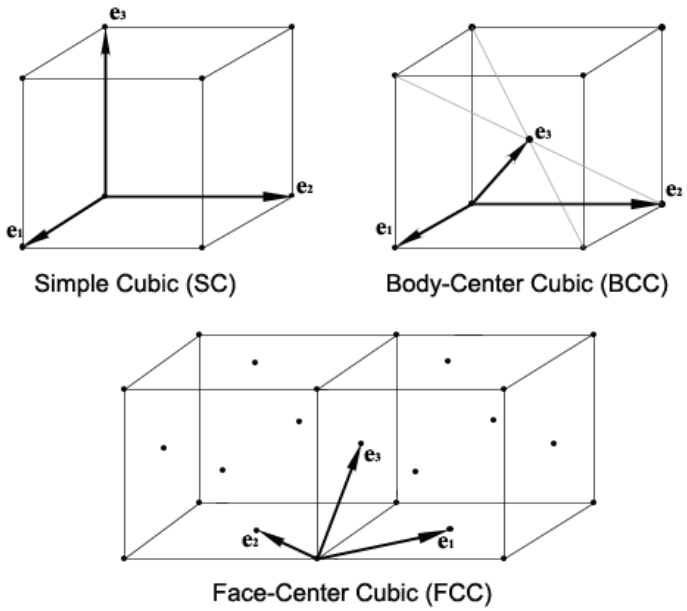

Figure 2.3: Three examples of Bravais lattice and their lattice vectors are shown.

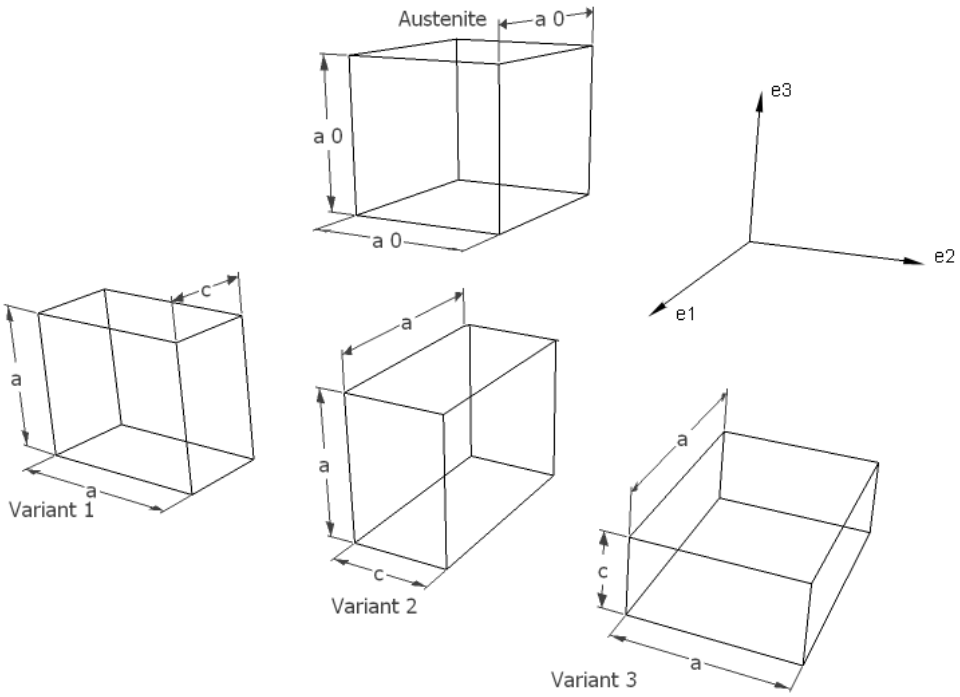

Figure 2.4: Three variants of tetragonal martensite and cubic austenite are shown. Strains are exaggerated for clarity.

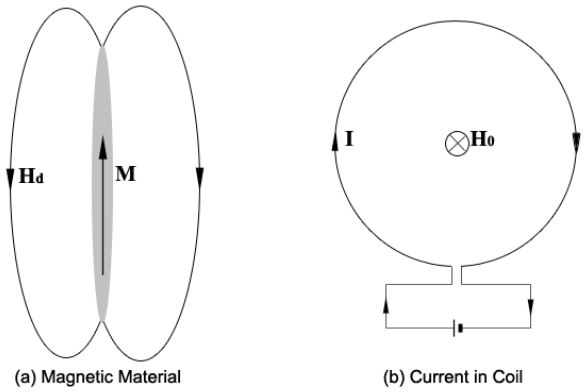

Figure 2.5: A magnetic field can be produced either by a) a magnetic material or b) current in the coil.

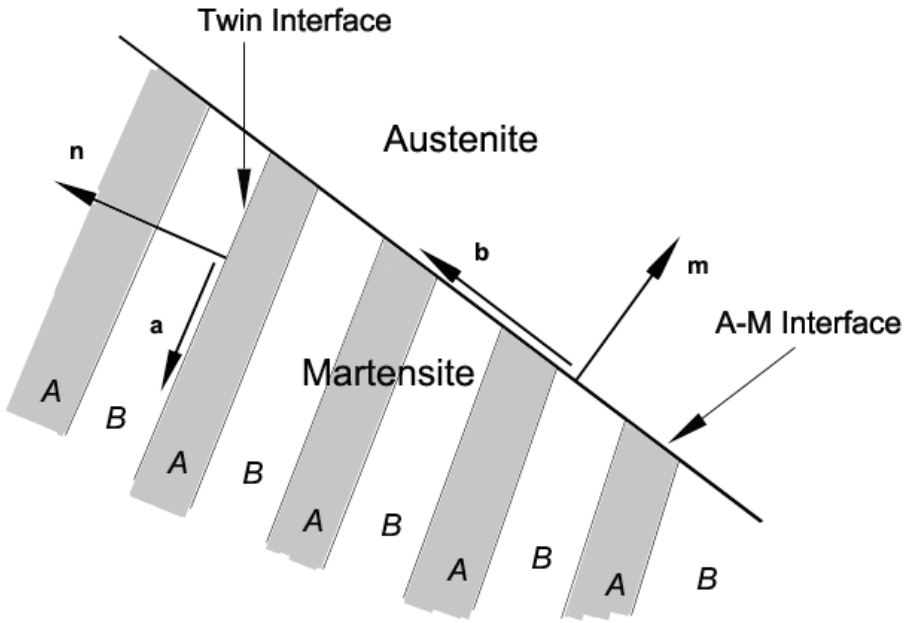

Figure 2.6: A sketch of austenite-martensite interface structure is presented above. The variants of martensite are labeled as A and B.

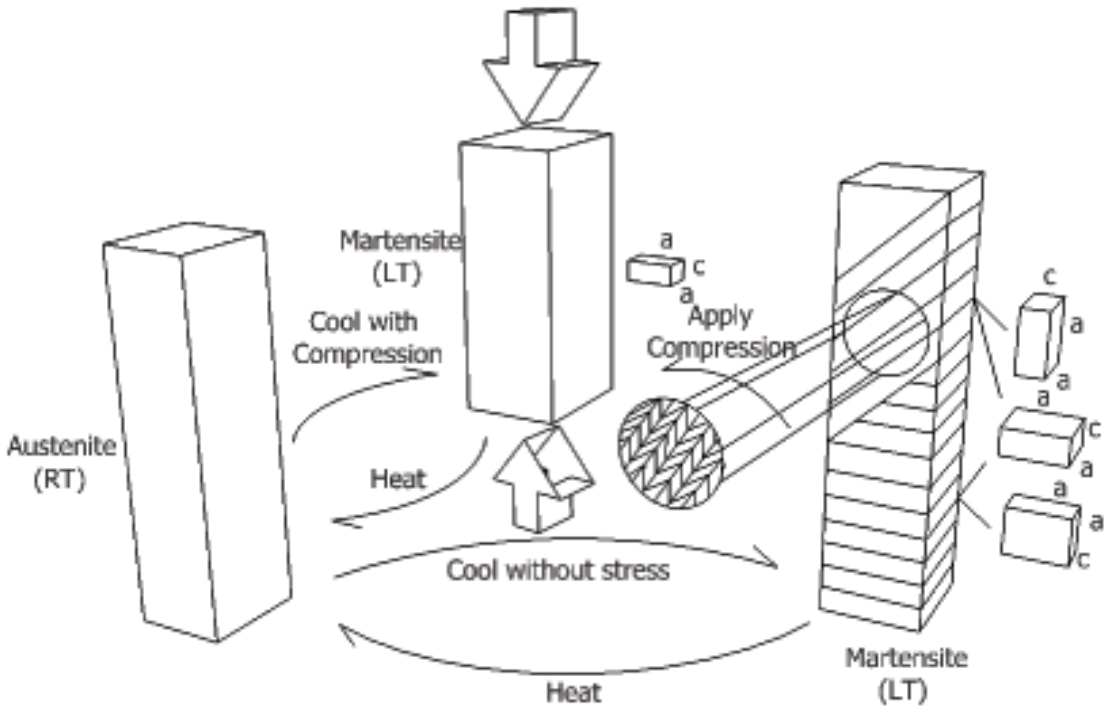

Figure 2.7: Shape memory behavior is based on austenite-martensite phase transformation process and martensite variants rearrangement [20].

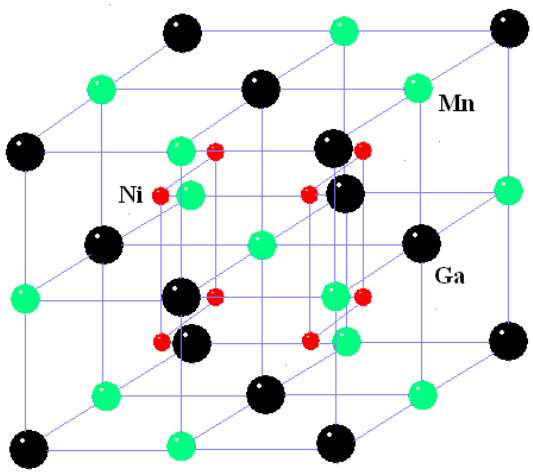

Figure 2.8: In an austenite Heusler unit cell of Ni_2MnGa material, the red atoms are nickel atoms, the green atoms are manganese ones and the black atoms are gallium ones. The unit cell has a face-centered-cubic structure.

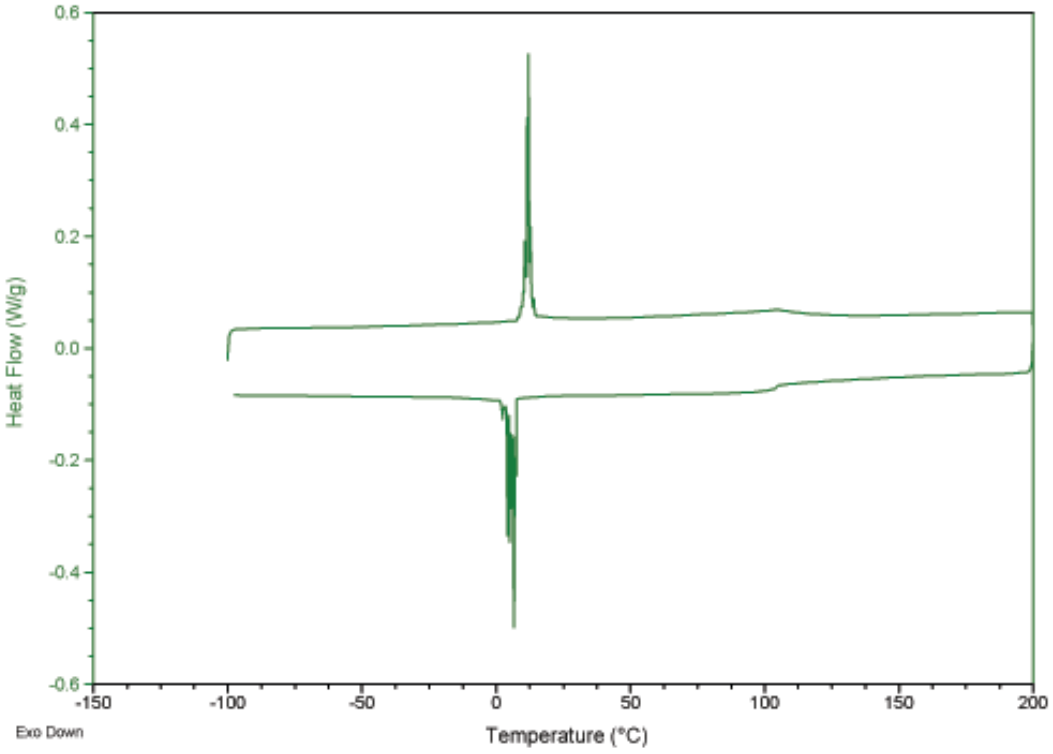

Figure 2.9: Differential scanning calorimeter (DSC) measures the heat flow through the nominal $Ni_{50}Mn_{27}Ga_{23}$ sample during austenite-martensite phase transformation process. The upper curve shows the sample being heated from martensite to austenite, and the lower curve shows the sample being cooled from austenite to martensite [37].

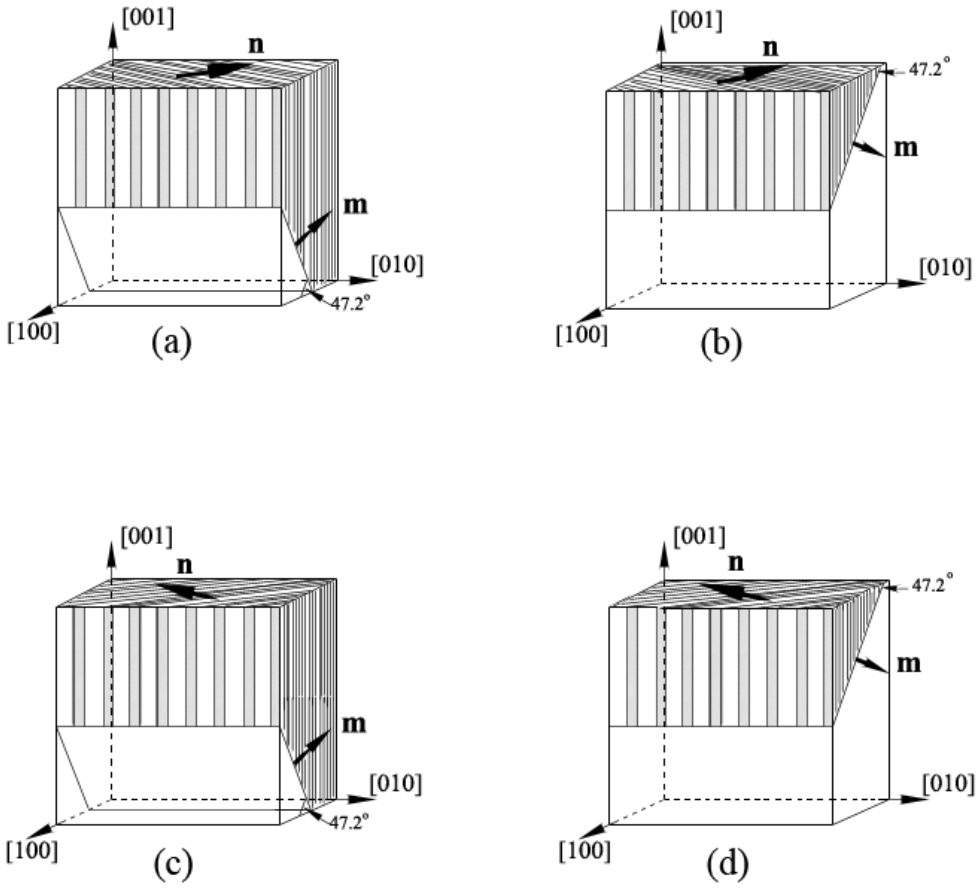

Figure 2.10: The microstructure in (a) represents the solution of (2.53), the one in (b) represents (2.55), the one in (c) represent (2.57) and (d) is (2.59). The microstructures are observed on (100) plane appear the same.

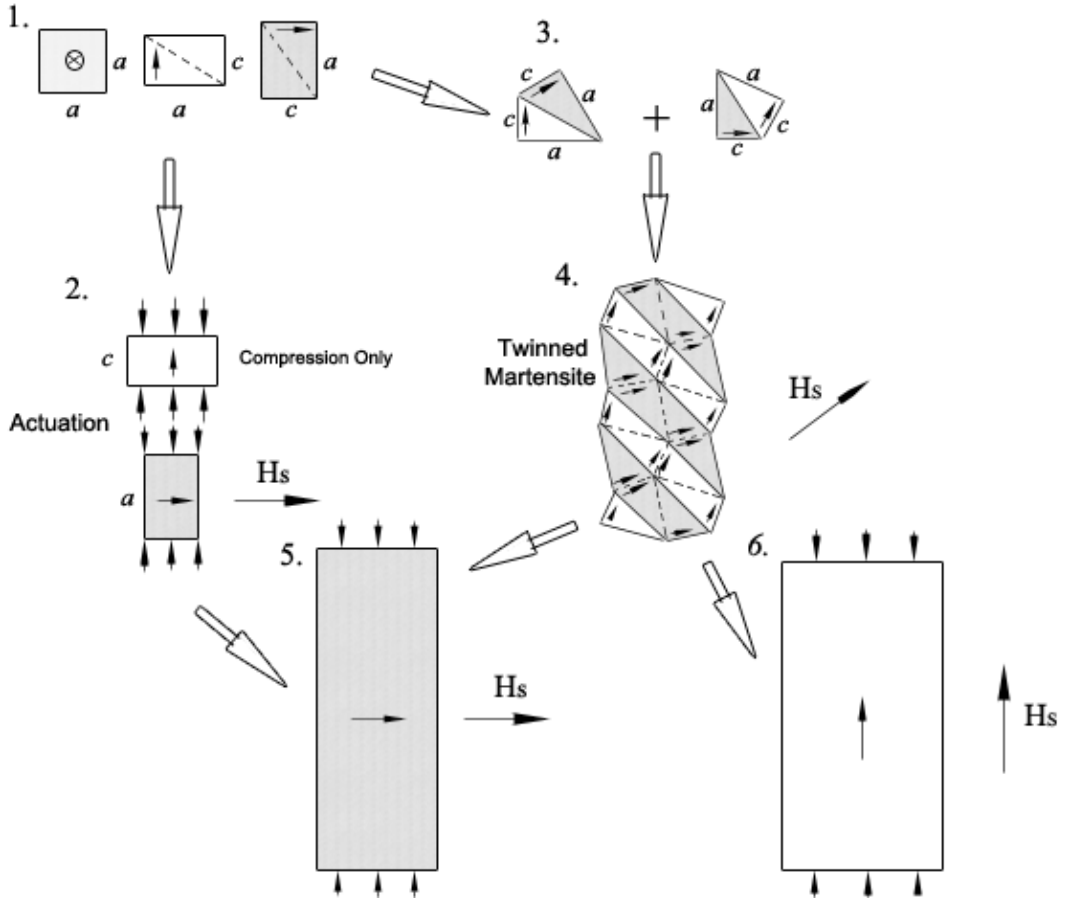

Figure 2.11: The mechanism of ferromagnetic shape memory behavior in a Ni_2MnGa single crystal sample is shown [43]. Part 1 shows the martensite variants, and arrows represent the spontaneous magnetization directions of variants. Part 2 gives the possible actuation of variants under loading stress or magnetic field. Parts 3 and 4 indicate the forming of martensite twins. Parts 5 and 6 give the martensite variants rearrangement cases under different applied magnetic fields.

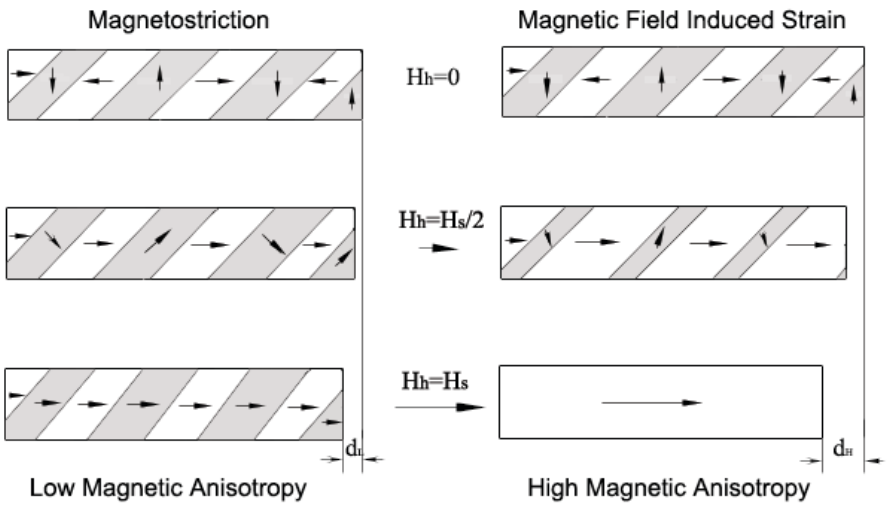

Figure 2.12: The mechanisms of magnetostriction and magnetic field induced strain (MFIS) are shown. The arrows here indicate the directions of spontaneous magnetization.

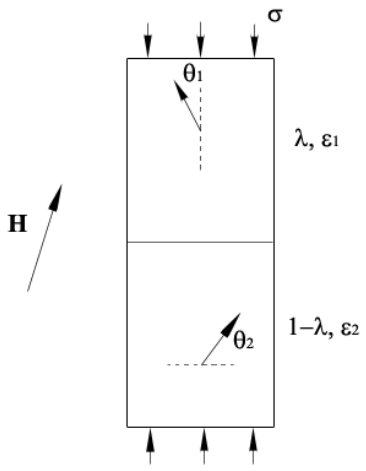

Figure 2.13: In this lumped phase model, a martensitic single crystal sample is assumed to be two variants that are single magnetic domains.

Chapter 3

Sample Preparation and Experimental Apparatus

This chapter presents information on the Ni_2MnGa single crystal sample preparation and experimental apparatus that used to perform the experiments.

3.1 Sample Preparation

In order to study the Ni_2MnGa FMSA austenite-martensite phase transformation and magneto-mechanical properties, a 2mm×2mm×10mm rectangular single crystal sample with (100), (010) and (001) faces was prepared. Using single crystals avoids the complications of polycrystalline samples. Because of the limited number of variant rearrangement modes in tetragonal martensite, polycrystalline samples are not expected to exhibit FSMA behavior.

All of the mechanisms presented in the previous chapter assumed the tetragonal variants were aligned with the sample faces. The orientation is defined by the sample coordinate system (x,y,z), shown in Figure 3.1. The orientation of z is along the [001] cubic crystallographic direction of sample, which is 10mm long, x and y are along [100] and

[010], respectively, which are both 2mm wide. Mechanical loading will always be with z-direction.

3.1.1 Sample Preparation Processes

Four samples, NMG3-P6, P7, P8 and P9 were cut from the same No.3 nickel-manganese-gallium low-defect concentration crystal boule (NMG3), which was grown by the Bridgman method and bought from Ames National Laboratories. The crystal has the nominal atomic composition of Ni 50%, Mn 27%, Ga 23%. The Mitsubishi DWC90C Electrical Discharge Machine (EDM) was used to cut samples to designed dimensions and orientation, which uses a moving wire electrode that goes through the workpiece with a $\pm$0.0001inch (0.002mm) accuracy. The wire cutting path and speed are controlled by the computer numerically control system (CNC). The EDM can provide fast and accurate cutting of conductive materials without mechanical deformation and stress concentration on the cutting surface. After cutting, all samples were mechanically polished with same processes at room temperature. Samples NMG3-P6 and P7 were used to finish some other preliminary experiments sample NMG3-P8 and P9 were used with final experiments. The final dimensions of each sample are listed in Table 3.1. The sample preparation processes are briefly introduced below, more details are given in Appendix A.

First, the crystal was placed in a keyed holder, and it was orientated by using X-ray Micro-diffraction. Then, three plates from this boule with a [100] normal were cut by using EDM. All samples were cut from the same single crystal grain with [100] normal direction in the three pieces. After machining, all four 2mm$\times$2mm$\times$10mm samples, named as NMG3-P6, P7, P8 and P9, had the designed orientation, which was checked by X-ray Micro-diffraction again. It was found that the orientation errors were less than 1^{o}. Ames Laboratory provided a composition profile along the length of the boule and this was used to determined that all four samples have the same composition of Ni 49%, Mn 28%, Ga 23%.

The BUEHLER Minimet/Carbinmet^{TM} system was used to finish the mechanical polishing. For each sample, there was one surface with [100] normal mechanically polished. All samples were polished at room temperature as austenite. The final optically reflective surfaces are obtained in six steps by using 320 Grit, 600 Grit, 800 Grit, 1200 Grit polishing paper and 1μm, 0.5μm alumina polishing suspension. The rough grit (320, 600, 800, 1200) polishing usually needed 4-5 runs each depending on the finishing results, and the fine grit (5μm, 1μm, 0.5μm) polishing only needed one. After 0.5μm fine polishing, polishing remains and grease need to be removed from the surface, which is done by using de-ionized water, acetone and ethyl alcohol. More details of polishing and cleaning are in Appendix A.

3.2 Experimental Apparatus

The primary experiments were carried out on the Magneto-Mechanical Test Machine (MMTM). Figure 3.2 shows the front view of Magneto-Mechanical Test Machine (MMTM) locating at Akerman Hall 24. The MMTM system is made up of three main parts, loading and control system, sample fixture on MMTM and data and images recording system. Each of them will be introduced briefly below, and more details can be found in Appendix B.

3.2.1 Loading and Control System

Loading and control system on MMTM has three main sub-systems [43]. One is the Instron 4467 mechanical testing machine with 1300 N load cell. Its loading rod is made of non-magnetic aluminum bronze (alloy 642), which has a magnetic permeability near 1.0. The resolution of the displacement and load control are 0.5μm and 0.05N. The second sub-system is the water-cooled electromagnet. When it is at its full power, a maximum magnetic field of 8500 G can be generated in the center of the 100mm pole gap. The function of the four coplanar pole pieces is to allow the magnetic field to be

rotated in a plane that contains the mechanical loading axis. The third sub-system is the temperature control system that has a range of -50 to 150°C when using the appropriate fluids and a maximum rate of 1°C/min.

3.2.2 Sample Fixture

In the center of the pole gap of MMTM, a sample fixture sits on top of the bottom loading rod and holds a loading head and a loading pin that contacts the sample as shown in Figure 3.3. The top loading rod is connected to the Instron machine crosshead and applies force to the sample through the loading head and loading pin. Different with the original compressive sample fixture in the MMTM, which only has a loading pin and can only apply compression to the sample, the modified loading head-loading pin fixture gives the ability to applied both compression and tension to the sample as shown in Figure 3.4. Beside the modification of the loading head part, the sample also need to glue with the loading pin at the top and with the fixture at the bottom in order to apply tensions. The position of the fixture can be adjusted along the loading direction by the bottom spacers which are a series of circular disks with various thickness, such that the center of the sample coincides with the center of the pole gap. Inside the fixture are cavities through which the temperature controlled fluid is circulated. In addition, the fixture, the loading head, the loading frame, the loading pin, and the spacers are all made of the same alloy used to make the loading rod, the non-magnetic aluminum bronze (alloy 642). The sensors, which are used to record the sample temperature, magnetic field around sample, and the sample displacement, are attached to the fixture. The fixture is enclosed in a camber that is flushed with dry nitrogen gas to avoid condensation or frost formation when operating below the dew point.

3.2.3 Program Control and Data and Recording System

The Magneto-Mechanical Test machine is controlled by a program called mmtm-control running under Linux. All load paths, which include load and magnetic field, can be set and modified through the program. All the instruments are connected to the computer using an IEEE-488 interface. These instruments include an eight-channel 16 bit A/D converter (Iotech 488/ ADC8SA), a two-channel 16 bit D/A converter (Iotech 488/ DA2HR) to control the magnet currents, the Instron load frame, and a three-channel Gaussmeter (Lakeshore Model 460). In addition, this computer provides a overlay graphics display on the video from the camera on the microscope at the back side of MMTM, by using a Magni Systems MagniCoder. This allows synchronization of the video and data streams on playback for later analysis.

At the the back side of the MMTM, there is a Nikon optical microscope with differential interference contrast (DIC), which is used to observe the changes of microstructure of the specimen surface during phase transformation and variants rearrangement, as shown in Figure 3.5. This microscope is connected to a digital camera, and all images from the digital camera are stored on the disk of an SGI O2 workstation. The video can also be recorded and saved on a video tape recorder.

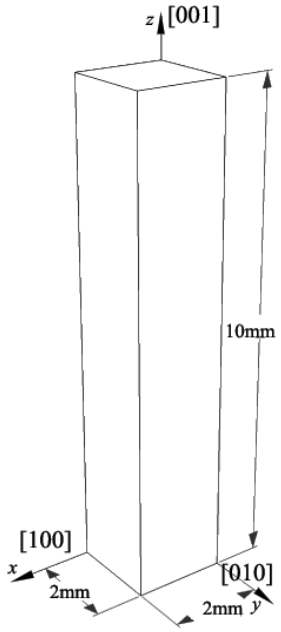

Figure 3.1: The sample orientation is defined by the (x, y, z) sample coordinate system. Typical sample dimensions are shown.

Table 3.1: The final dimensions of samples NMG3-P6, P7, P8 and P9 are shown.

Sample ID	Dimensions (mm)
NMG3-P6	2.00×1.68×9.15
NMG3-P7	2.05×2.01×10.01
NMG3-P8	2.00×2.00×10.02
NMG3-P9	2.00×2.00×9.28

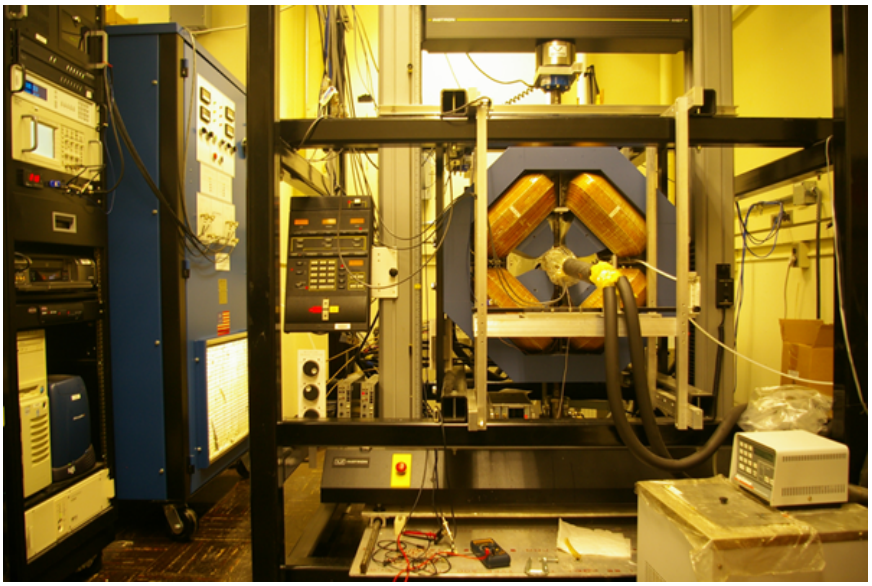

Figure 3.2: The magneto-mechanical test machine (MMTM) is located in Akerman Hall 24. The MMTM is made up of three main parts, loading and control system, sample fixture and data and images recording system.

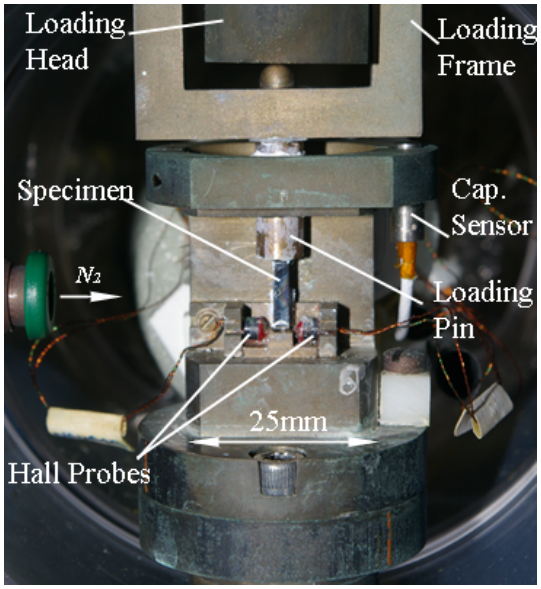

Figure 3.3: In the center of the pole gap of MMTM, a sample fixture sits on top of the bottom loading rod and holds a loading head and a loading pin that contacts the sample. Sensors are attached in the fixture to measure the displacement, the temperature of the sample and the magnetic field around the sample.

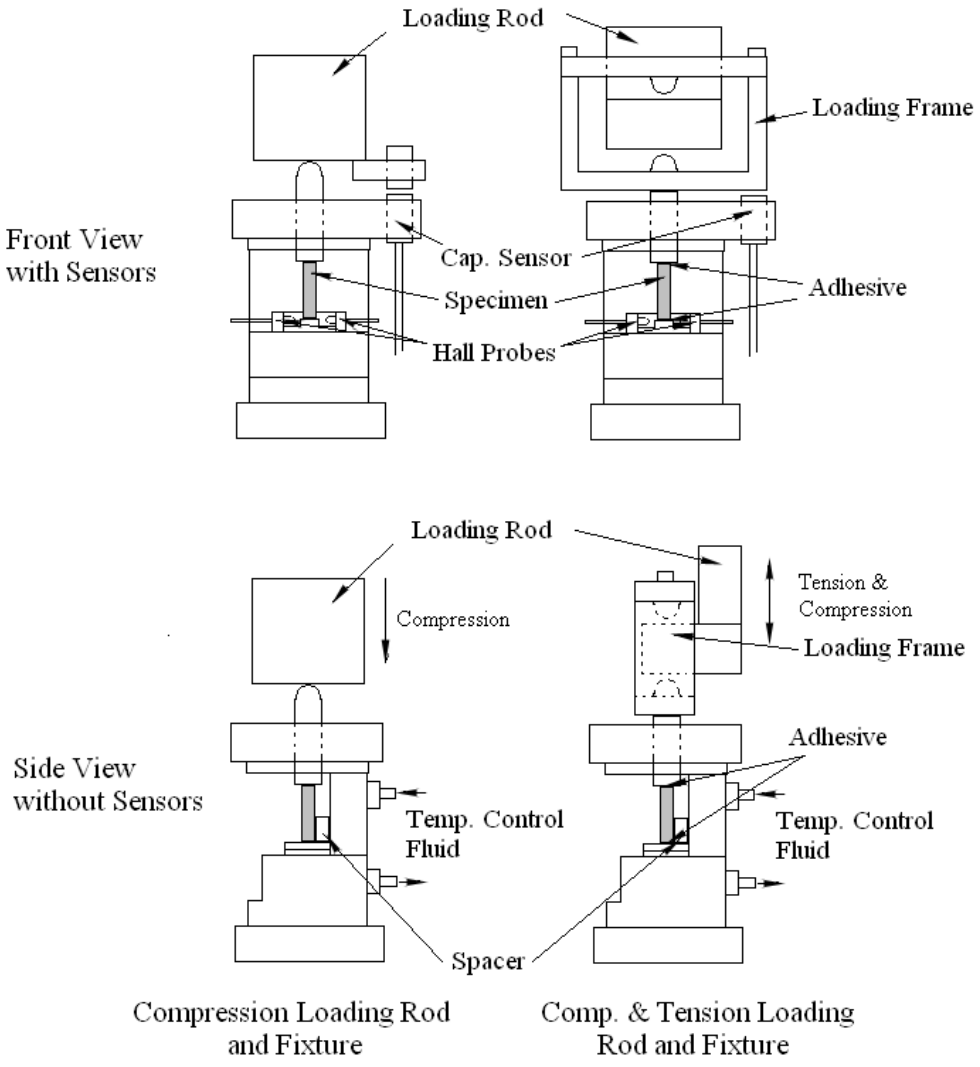

Figure 3.4: Different with the left side original compressive sample fixture in the MMTM, which only has a loading pin and can only apply compression to the sample, the right side modified loading head-loading pin fixture gives the ability to applied both compression and tension to the sample as shown.

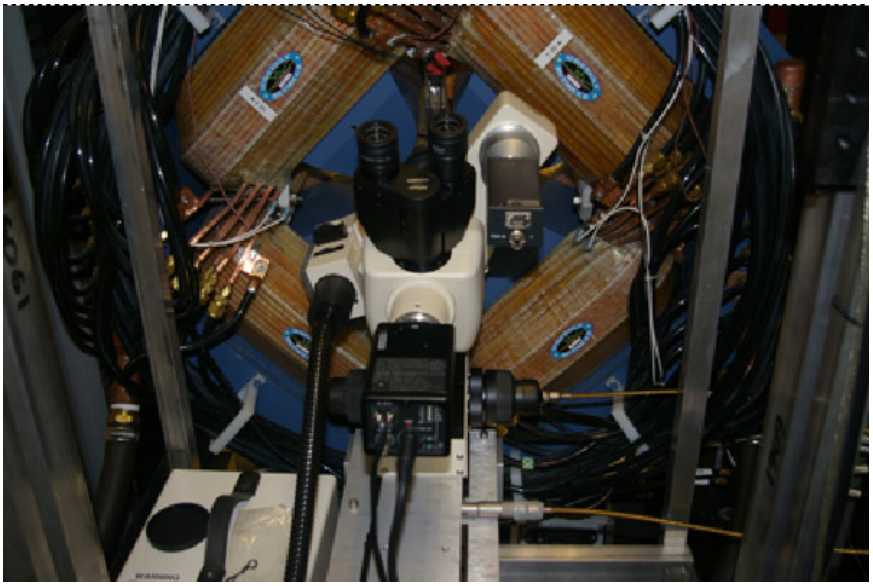

Figure 3.5: A Nikon optical microscope on back of MMTM is used to observe the surface microstructure of the sample during experiments.

Chapter 4

Phase Transformation Experiments

These experiments were performed on sample NMG3-P8 using the Magneto-Mechanical Test Machine (MMTM). The goal of these experiments was to study the effects of applied stress and magnetic field on the phase transformation process of Ni_2MnGa material.

4.1 Experimental Conditions

Because the reversible austenite-martensite phase transformation process is the key to the shape memory mechanism, the effect of phase transformation conditions on the phase transformation process becomes an interesting research topic. In order to study the differences between compression and tension, different amounts of compression and tension were chosen. During preliminary experiments, it was found that the sample could support a maximum 8 MPa compression without breaking, thus, an 8 MPa compression was the maximum compression applied. It was also found that below martensite finish temperature, M_f, the adhesive used between the stress loading pin and the sample could support a maximum 3 MPa tension without failure, thus a 3 MPa tension was the maximum tension applied. Table 4.1 shows the details of NMG3-P9 sample austenite-martensite phase transformation experimental conditions. At each stress level, different magnetic fields are applied to study the combined effect of stress and magnetic field. As discussed in Section 2.5.4, different directions of applied magnetic field, parallel or

normal to the applied stress direction, should have different effects on the phase transformation process, so for each stress condition, magnetic fields with different directions and magnitudes were chosen. In Table 4.1, vertical magnetic field is the [001] direction of our rectangular sample, which is the loading direction. Horizontal magnetic field is the [010] direction, which is the transverse (short) direction of the rectangular sample and normal to the applied stresses.

4.2 Ni_2MnGa Phase Transformation Process

Figures 4.1 and 4.2 show two strain vs. temperature data of Ni_2MnGa phase transformation processes between austenite and martensite under compression and tension without applied magnetic field. The result in Figure 4.1 are for starting conditions of an 8 MPa compression at room temperature without any applied magnetic field. The section of the data labelled 1 is prior to the phase transformation occurring. The slope of curve in part 1 is primarily due to the thermal contraction of the material. After an initial transient, the curve in section 1 is quite linear. When the temperature reaches the martensite start temperature (M_s), the sample begins transforming to martensite starting at the ends that are in contact with the fixture. In part 2, martensite that compatibly coexists with austenite in the sample grows until the entire sample is martensite at the martensite finish temperature (M_f). Because of the applied compression, variants that result in a shorter sample are favored. Thermal contraction of the martensite occurs in part 3. After the sample was cooled to -1 ^{o}C, the sample is heated back, and part 4 shows the temperature of the martensitic sample is increasing smoothly. When the sample temperature reaches the austenite start temperature (A_s), the phase transformation begins and continues during part 5 until the austenite finish temperature (A_f). In part 6, the sample has been fully transformed back to austenite and thermal expansion is again the primary cause of the observed strain change.

The result in Figure 4.2 are for starting conditions of a 3 MPa tension at room temperature without any applied magnetic field. Part 1 in the figure also shows the austenitic

sample is cooled without main phase transformation. The initial slope of curve in part 1 is due to thermal contraction of the material. The lower section of part 1 is probably caused by a small part of sample transforming to martensite and temperature gradients in the sample. But the bulk of the sample is still austenite. When the temperature is lowered to the martensite start temperature (M_s), the main austenite to martensite phase transformation begins. In part 2, there is more and more martensite that compatibly coexists with austenite in the sample until the transformation completes at the martensite finish temperature (M_f). In this case, the martensitic sample is longer than the austenite one, because different variants are favored under tension than compression. Only martensite exists in the sample in part 3 and the sample thermally contracts with the further cooling. After the sample was cooled below 0 ^{o}C, heating was started. The temperature of the martensitic sample is increasing smoothly until austenite start temperature (A_s) in part 4 and the lack of expansion is probably due to some early reverse transformation. The phase transformation begins at A_s and continues going in part 5 until the austenite finish temperature (A_f). In part 6, the main part of the sample has been transformed back to austenite and the data exhibits similar features to those in part 1.

The phase transformation temperature values (M_s, M_f, A_s, A_f) of sample under different loading conditions were also determined through a series measured results like those in Figures 4.1 and 4.2. From Figures 4.1 and 4.2, it can be observed that the thermal contraction and expansion results in both austenite and martensite are almost linear, and the results of phase transformation processes are also linear. So the phase transformation temperatures are chosen by following the rules: If the curve changes sharply, then the point at which the curve changes sharply will be chosen as phase transformation point and related temperature will be selected as phase transformation temperature; If the curve change smoothly, temperature is that at which curve starts to depart from the linear part which is fit to the last linear portion of the curves. For some conditions, it is hard to chose the accurate phase transformation points and temperature from temperature versus strain results based on either methods above. For example, the phase transformation results under 2 MPa tension and 2750 G vertical magnetic field are shown in Figure 4.3, and from the figure, it is hard to figure out the accurate

phase transformation points.

From average values of parts 2 and 5 measured strain results in Figures 4.1 and 4.2, it is found that the phase transformation strains under compression and tension are:

$$\varepsilon_m{}^C = -0.025; \quad \varepsilon_m{}^T = 0.017, \tag{4.1}$$

where subscript m means the measured result. Compare these values with the theoretical values in (2.34), it can be seen that the tension strain agrees well with the theoretical prediction, but the compression strain is much smaller than the theoretical one. The strains measured relate to the volume fractions of the variants present. The theoretical calculations assume a pure single variant state. In compression only one of the three variants is energetically favored, while tension equally favors two variants (in the absence of applied magnetic field). Thus there are more deformation modes (microstructures) possible in the tension case that make it easier for the variants favored by the tension to accommodate the sample end conditions. This might account for the closer agreement in the tension case.

4.3 Microstructure Images of A-M Boundary and Martensitic Twins

As discussed in Section 2.5.3, during the austenite-martensite phase transformation process, two kinds of interfaces will be observed: A-M boundary, and twin boundaries. Figure 4.4 shows a series of images during austenite to martensite (cooling) phase transformation process under a small uniaxial compression and a large horizontal magnetic field. The images are labelled in chronological order.

In Section 2.5.3, the possible A-M boundary and martensitic twins were given. The observed microstructures are determined by the variants favored by the loading conditions. Figures 4.5 and 4.6 show different surface microstructures during heating under

3 MPa tension with horizontal 2750 G magnetic field and during cooling under 1 MPa compression without any field. In Figure 4.5, the A-M boundary is almost horizontal and twin boundaries are vertical, but in Figure 4.6, the A-M boundary is almost vertical and twin boundaries are horizontal.

It is difficult to identify the microstructure in Figure 4.5 or 4.6 with a unique solution (2.36)-(2.59), because only one sample surface can be observed, even if the variants favored by the loading conditions are known. But some conclusions can be reached, for example, it is known that the martensite to austenite (heating) phase transformation in Figure 4.5 occurred under a large uniaxial tension and a moderate horizontal magnetic field, so variant 2 with stretch matrix $\mathbf{U}_2$ in (2.18) will be favored, so the four possible CTM solutions are (2.53), (2.55), (2.57) and (2.59). If microstructure images of two orthogonal surfaces were obtained, the possible solutions could be reduced to two. If images of three sample surfaces were obtained, the solution could be determined. Figure 4.6 shows another surface microstructure during austenite to martensite (cooling) phase transformation under a small uniaxial compression without any magnetic field. Here, $\mathbf{U}_3$ in (2.18) is favored, and the four possible CTM solutions are (2.36), (2.38), (2.40) and (2.42).

Returning to the phase transformation images in Figure 4.4, because the sample is under a small compression and a large horizontal magnetic field, the stretch matrix of $\mathbf{U}_2$ in (2.18) will be favored, so either (2.44) or (2.46) matches the experimental results. There are only two possible solutions, instead of four for Figures 4.5 and 4.6, because none of any other results will match both A-M boundary and twin boundaries orientations.

4.4 Stress and Magnetic Field Effects on Phase Transformation Temperature

Recently, Liang *et al.* [18] reported a simple model to theoretically calculate either stress or magnetic field effects on the phase transformation temperature of both FePd and Ni_2MnGa FSMAs. For Ni_2MnGa, they reported about a 0.32 K/MPa stress coefficient and a 3.2×10^{-4} K/G magnetic field coefficient. But this work did not consider on the differences between longitude and transverse magnetic field. Nor can these results be found in any other publications. In this section, the difference between the uniaxial compression and tension on the phase transformation temperature and the combination effects of different stresses and magnetic fields are considered.

4.4.1 Results and Discussion

The effects of stress on Ni_2MnGa single crystal alloy phase transformation temperature are shown in Table 4.2. In this table, the phase transformation temperatures under different stress conditions are shown in the left column. The sixth column shows the stress coefficients, which are from a linear fit of phase transformation temperature versus stress results in Figure 4.7. The last column is the theoretical results based on (2.60) in Section 2.6.1 by using the material constants given in Section 2.5.2.

It is found that the calculated results based in particular large stresses are nearer to the measurements. The reason for this is that the small stresses are not sufficient to bias the sample into a single variant state during the phase transformation process, and (2.60) assumes the transformation is from austenite to single variant. If the transformation id not to a single variant state, then the volume fractions of the variants must be known to make a prediction. Cooling and heating under larger stresses may not produce single variant states either, however, the volume fraction of one variant likely be much larger than the others. In these case, (2.60) agrees well with the experimental data. These results for cooling under tension are also far from the predictions, because it is hard to

determine the phase transformation temperatures under small tension level, such as 1 MPa result in Figure 4.3.

The effect of compression on the phase transformation is about 0.2∼0.4 K/MPa, which is similar with the result of Liang *et al*. But the effect of tension on A_s/A_f is of only about 0.1∼0.2 K/MPa. Equation (2.60) can explain where this difference comes from. In the right side of (2.60), the latent heat is not influenced by either compression and tension, nor is the phase transformation temperature. But the transformation strains under compression and tension are different. From the lattice constants, that the phase transformation strain under compression is almost two and a half times the strain under tension. This is why the effect of compression on transformation temperature is about two and a half times the effect of tension. It is not clear why the experimental data shows such a large effect of tension on M_s/M_f.

Figure 4.7 combines the results of phase transformation experiments at -8, -2, -1, 1, 2, 3 MPa and stress-free DSC measurement. In addition the M_s and A_s data agrees better than the finish temperatures. It is hard to determined phase transformation temperatures accurately for the tension tests, as previous mentioned, and these measurements may have large uncertainty.

The effects of different magnetic field conditions on phase transformation temperatures are listed separately in Tables 4.3, 4.4, 4.5 and 4.6. From these tables, it can be seen that only some of the experimental data agree with the theoretical calculations. Some measurements even have the opposite effects with the results of calculations. The effect of stress on phase transformation temperatures increase the phase transformation temperatures for both tension and compression, and the effect is about 0.2∼0.4 K/MPa for compression and 0.1K/MPa for tension. And from the theoretical model of magnetic field effect, is can be calculated that the magnetic field effect is about 0.05 K/kG, that means 5500 Gauss magnetic field can only give the similar effect with 1 MPa compression or 2 MPa tension compared with early calculation in Table 4.2. Second, from Section

2, it is known that vertical magnetic field will help compression and compete with tension, and the horizontal magnetic field will help tension and compete with compression, because the existence of short magnetic easy axis in Ni_2MnGa. So under the applied stress and magnetic field at the same time, the effect on phase transformation may be complex. We can draw the different combination conditions of stress and magnetic field separately in Figures 4.8, 4.9, 4.10 and 4.11, and then give the explanations. In Figures 4.8 and 4.11, which the stress and magnetic field will help each other, it can be found that the under small compression and all tension conditions except 1MPa heating without field, the magnetic field will increase the phase transformation temperatures as expectation. But the effects are much smaller than the temperature jumps from different stress levels. And the magnetic field under large compression will slightly decrease the temperatures, which seems unreasonable, and it is most possible coming from the measurement errors, it is similar for data point of 1 MPa tension cooling without field.

In Figures 4.9 and 4.10, where the stress and magnetic field will compete each other, that is to say the simple assumption in the theoretical analysis that the austenite transforms into single dead load favored variant martensite may be not satisfied. So the effect will become complex. For the small level stresses (1 MPa compression and tension), the magnetic field effects follow the increasing expectation, that is because the magnetic fields here have much larger effects on the martensitic variant than the small stresses, and the variant will favor a single condition related with the fields and neglect the small stresses. Then the mechanism is similar with the zero load condition. But under large stress level (8 MPa compression and 3 MPa tension), because of the competition of the stress and field, the variant condition is complex, either stress or magnetic field will dominate the variant condition. So the effects keep changing.

Table 4.1: The conditions of which experiments where performed to study stress and magnetic field effects on transformation temperatures are listed.

Experiment Number	20 °C (Austenite) → -5 °C (Martensite) → 20 °C (Austenite)	
	Load (MPa)	Field (Gauss)
PT Temp. 1	-8	0
PT Temp. 2	-8	Vertical 2750
PT Temp. 3	-8	Vertical 5500
PT Temp. 4	-8	Horizontal 2750
PT Temp. 5	-8	Horizontal 5500
PT Temp. 6	-2	0
PT Temp. 7	-2	Vertical 2750
PT Temp. 8	-2	Vertical 5500
PT Temp. 9	-2	Horizontal 2750
PT Temp. 10	-2	Horizontal 5500
PT Temp. 11	-1	0
PT Temp. 12	-1	Vertical 2750
PT Temp. 13	-1	Vertical 5500
PT Temp. 14	-1	Horizontal 2750
PT Temp. 15	-1	Horizontal 5500
PT Temp. 16	1	0
PT Temp. 17	1	Vertical 2750
PT Temp. 18	1	Vertical 5500
PT Temp. 19	1	Horizontal 2750
PT Temp. 20	1	Horizontal 5500
PT Temp. 21	2	0
PT Temp. 22	2	Vertical 2750
PT Temp. 23	2	Vertical 5500
PT Temp. 24	2	Horizontal 2750
PT Temp. 25	2	Horizontal 5500
PT Temp. 26	3	0
PT Temp. 27	3	Vertical 2750
PT Temp. 28	3	Vertical 5500
PT Temp. 29	3	Horizontal 2750
PT Temp. 30	3	Horizontal 5500

Table 4.2: The effect of stress on Ni_2MnGa single crystal alloy phase transformation temperature is shown. The phase transformation temperatures under different stress conditions are shown in the first column. The sixth column is the stress effects on the phase transformation from the linear fit slopes in Figure 4.6. The last column is the theoretical calculation results based on C-C equation.

	Strain	PT Temperature (°C)				
Stress	Change	Start	End	Average	Slope	$-\frac{\varepsilon^{PT}\theta_{avg}}{Q_L}$
σ (MPa)	${\varepsilon_m}^{PT}$	M_s/A_s	M_f/A_f	θ_{avg}	(K/MPa)	(K/MPa)
——— Cooling (Compression) ———						
-1	-0.018	6.1	3.3	4.7		-0.62
-2	-0.020	6.1	3.4	4.75	M_s:-0.32	-0.62
-8	-0.024	7.4	6.3	6.85	M_f:-0.45	-0.63
——— Cooling (Tension) ———						
1	0.008	5.2	4.4	4.8		0.23
2	0.013	6.7	5.0	5.85	M_s:0.75	0.23
3	0.014	6.7	6.0	6.35	M_f:0.8	0.23
——— Heating (Compression) ———						
-1	0.018	10.5	12.5	11.5		-0.64
-2	0.021	10.7	12.7	11.7	A_s:-0.32	-0.64
-8	0.025	12.7	14.9	13.8	A_f:-0.34	-0.64
——— Heating (Tension) ———						
1	-0.008	12.4	13.6	13.0		0.23
2	-0.014	12.0	13.6	12.8	A_s: 0.15	0.23
3	-0.015	12.1	13.7	12.9	A_f: 0.05	0.23

Table 4.3: The combinational effects of compressions and vertical magnetic fields on the phase transformation temperatures are shown. The sixth column from left shows the quantities of the effects from phase transformation temperature vs. magnetic field. The last column is the theoretical calculation results based on (2.69) in Section 2.6.2.

h (G)	$\hat{\mathbf{e}}_h$	M_s/A_s (°C)	M_f/A_f (°C)	θ_{avg} (°C)	Slope ($\times 10^{-4}\frac{K}{G}$)	$\hat{\mathbf{e}}_h \cdot [\![\mathbf{m}]\!]$ ($\frac{emu}{cm^3}$)	$-\frac{\hat{\mathbf{e}}_h \cdot [\![\mathbf{m}]\!]}{Q_L/\theta_{avg}}$ ($\times 10^{-4}\frac{K}{G}$)
				Cool at -1 MPa			
0	-	6.1	3.3	4.7			
2750	[001]	6.1	4.6	5.35		39	0.6
5500	[001]	6.1	5.0	5.55	1.45	72	1.1
				Heat at -1 MPa			
0	-	10.5	12.5	11.5			
2750	[001]	10.6	12.8	11.7		-39	0.5
5500	[001]	10.8	12.8	11.8	0.55	-72	1.0
				Cool at -2 MPa			
0	-	6.1	3.4	4.75			
2750	[001]	6.2	4.7	5.45		30	0.4
5500	[001]	6.0	5.0	5.5	1.36	74	1.1
				Heat at -2 MPa			
0	-	10.7	12.7	11.7			
2750	[001]	10.9	12.7	11.8		-30	0.4
5500	[001]	10.8	12.9	11.85	0.27	-74	1.0
				Cool at -8 MPa			
0	-	7.4	6.3	6.85			
2750	[001]	7.2	6.4	6.8		4	0.1
5500	[001]	6.7	6.0	6.35	-0.91	80	1.2
				Heat at -8 MPa			
0	-	12.7	14.9	13.8			
2750	[001]	12.7	14.9	13.8		-4	0.1
5500	[001]	12.2	14.6	13.4	-0.73	-80	1.1

Table 4.4: The combinational effects of tensions and vertical magnetic fields on the phase transformation temperatures are shown. The sixth column from left shows the quantities of the effects from phase transformation temperature vs. magnetic field. The last column is the theoretical calculation results based on (2.69) in Section 2.6.2.

h (G)	$\hat{\mathbf{e}}_h$	M_s/A_s (°C)	M_f/A_f (°C)	θ_{avg} (°C)	Slope ($\times 10^{-4}\frac{K}{G}$)	$\hat{\mathbf{e}}_h \cdot [\![\mathbf{m}]\!]$ ($\frac{emu}{cm^3}$)	$-\frac{\hat{\mathbf{e}}_h \cdot [\![\mathbf{m}]\!]}{Q_L/\theta_{avg}}$ ($\times 10^{-4}\frac{K}{G}$)
				Cool at 1 MPa			
0	-	5.2	4.4	4.8			
2750	[001]	6.7	4.1	5.4		-76	-1.1
5500	[001]	6.6	4.3	5.45	1.18	2	0
				Heat at 1 MPa			
0	-	12.4	13.6	13.0			
2750	[001]	10.7	12.7	11.7		76	-1.1
5500	[001]	11.1	13.0	12.05	-1.72	-2	0
				Cool at 2 MPa			
0	-	6.7	5.0	5.85			
2750	[001]	6.6	4.9	5.75		-101	-1.5
5500	[001]	6.9	4.0	5.45	-0.73	-4	-0.1
				Heat at 2 MPa			
0	-	12.0	13.6	12.8			
2750	[001]	10.3	12.5	11.4		101	-1.4
5500	[001]	9.6	12.2	10.9	-3.45	4	-0.1
				Cool at 3 MPa			
0	-	6.7	6.0	6.35			
2750	[001]	6.6	4.6	5.6		-141	-2.1
5500	[001]	6.0	4.4	5.2	-2.09	-12	-0.2
				Heat at 3 MPa			
0	-	12.1	13.7	12.9			
2750	[001]	9.9	12.7	11.3		141	-2.0
5500	[001]	10.7	11.7	11.2	-3.09	12	-0.2

Table 4.5: The combinational effects of compressions and horizontal magnetic fields on the phase transformation temperatures are shown. The sixth column from left shows the quantities of the effects from phase transformation temperature vs. magnetic field. The last column is the theoretical calculation results based on (2.69) in Section 2.6.2.

h (G)	$\hat{\mathbf{e}}_h$	M_s/A_s (°C)	M_f/A_f (°C)	θ_{avg} (°C)	Slope ($\times 10^{-4}\frac{K}{G}$)	$\hat{\mathbf{e}}_h \cdot [\![\mathbf{m}]\!]$ ($\frac{emu}{cm^3}$)	$-\frac{\hat{\mathbf{e}}_h \cdot [\![\mathbf{m}]\!]}{Q_L/\theta_{avg}}$ ($\times 10^{-4}\frac{K}{G}$)
				Cool at -1 MPa			
0	-	6.1	3.3	4.7			
2750	[010]	7.2	4.2	5.7		-103	-1.5
5500	[010]	7.1	5.5	6.3	2.91	-33	-0.5
				Heat at -1 MPa			
0	-	10.5	12.5	11.5			
2750	[010]	11.8	13.0	12.4		103	-1.4
5500	[010]	11.0	13.0	12.0	0.91	33	-0.5
				Cool at -2 MPa			
0	-	6.1	3.4	4.75			
2750	[010]	6.2	4.3	5.25		-112	-1.6
5500	[010]	5.7	3.3	4.5	-0.45	-33	-0.5
				Heat at -2 MPa			
0	-	10.7	12.7	11.7			
2750	[010]	10.5	12.8	11.65		112	-1.6
5500	[010]	10.5	12.1	11.3	-0.73	33	-0.5
				Cool at -8 MPa			
0	-	7.4	6.3	6.85			
2750	[010]	6.7	6.0	6.35		-205	-3.0
5500	[010]	6.9	6.3	6.6	-0.45	-27	-0.4
				Heat at -8 MPa			
0	-	12.7	14.9	13.8			
2750	[010]	12.7	15.2	13.95		205	-2.9
5500	[010]	11.7	14.0	12.85	-1.73	27	-0.4

Table 4.6: The combinational effects of tensions and horizontal magnetic fields on the phase transformation temperatures are shown. The sixth column from left shows the quantities of the effects from phase transformation temperature vs. magnetic field. The last column is the theoretical calculation results based on (2.69) in Section 2.6.2.

h (G)	$\hat{\mathbf{e}}_h$	M_s/A_s (°C)	M_f/A_f (°C)	θ_{avg} (°C)	Slope ($\times 10^{-4}\frac{K}{G}$)	$\hat{\mathbf{e}}_h \cdot [\![\mathbf{m}]\!]$ ($\frac{emu}{cm^3}$)	$-\frac{\hat{\mathbf{e}}_h \cdot [\![\mathbf{m}]\!]}{Q_L/\theta_{avg}}$ ($\times 10^{-4}\frac{K}{G}$)
				Cool at 1 MPa			
0	-	5.2	4.4	4.8			
2750	[010]	7.0	4.9	5.95		-114	-1.7
5500	[010]	6.4	5.5	5.95	2.09	17	0.2
				Heat at 1 MPa			
0	-	12.4	13.6	13.0			
2750	[010]	10.3	13.0	11.65		114	-1.6
5500	[010]	10.1	13.4	11.75	-2.27	-17	0.2
				Cool at 2 MPa			
0	-	6.7	5.0	5.85			
2750	[010]	7.5	5.4	6.45		-120	-1.7
5500	[010]	7.5	5.6	6.55	1.27	16	0.2
				Heat at 2 MPa			
0	-	12.0	13.6	12.8			
2750	[010]	12.0	13.6	12.8		120	-1.7
5500	[010]	11.9	13.5	12.7	-0.18	-16	0.2
				Cool at 3 MPa			
0	-	6.7	6.0	6.35			
2750	[010]	7.3	5.7	6.5		-124	-1.8
5500	[010]	7.8	6.3	7.05	1.27	13	0.2
				Heat at 3 MPa			
0	-	12.1	13.7	12.9			
2750	[010]	12.0	13.9	12.95		124	-1.8
5500	[010]	12.2	14.6	13.4	0.91	-13	0.2

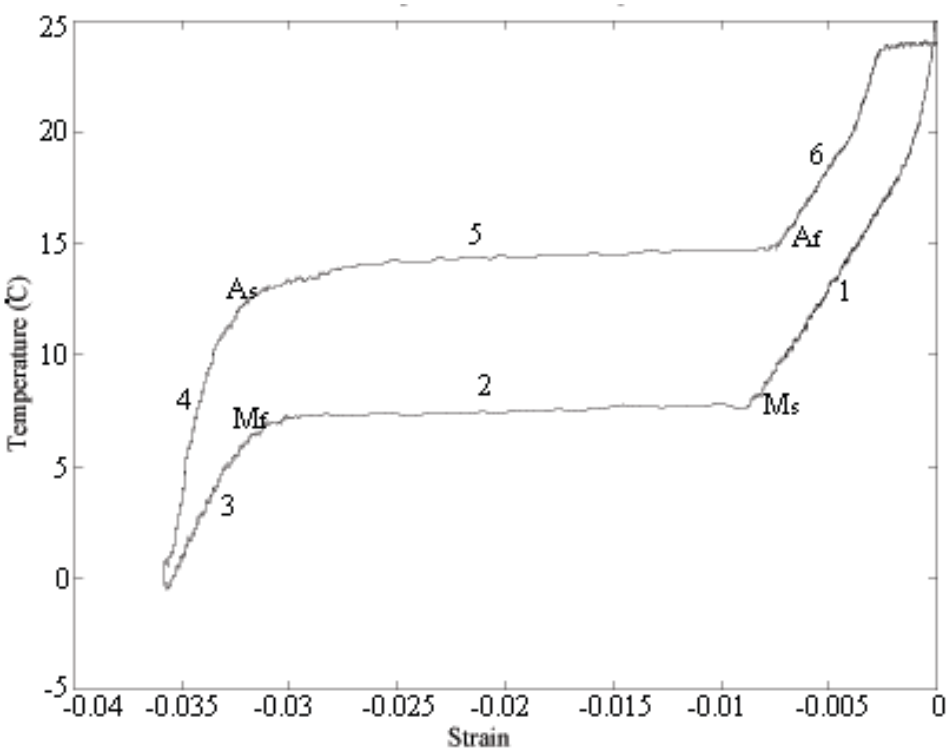

Figure 4.1: Sample NMG3-P8 is applied 8 MPa compression without any magnetic field at room temperature. Then it is cooled down from austenite to martensite through process 1, 2 and 3, and then heated back from martensite to austenite through process 4, 5 and 6. The martensite start temperature is M_s, M_f is the martensite finish temperature, A_s is the austenite start temperature and A_f is the austenite finish temperature in the figure.

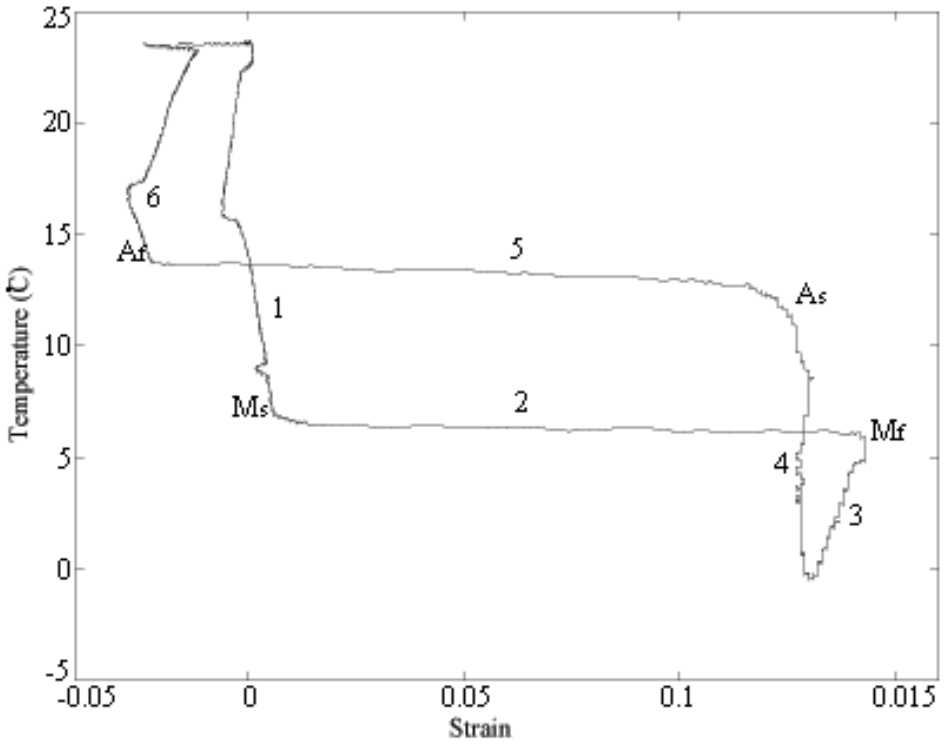

Figure 4.2: Sample NMG3-P8 is applied 3 MPa tension without any magnetic field at room temperature. Then it is cooled down from austenite to martensite through process 1, 2 and 3, and then heated back from martensite to austenite through process 4, 5 and 6. M_s is the martensite start temperature, M_f is the martensite finish temperature, A_s is the austenite start temperature and A_f is the austenite finish temperature in the figure.

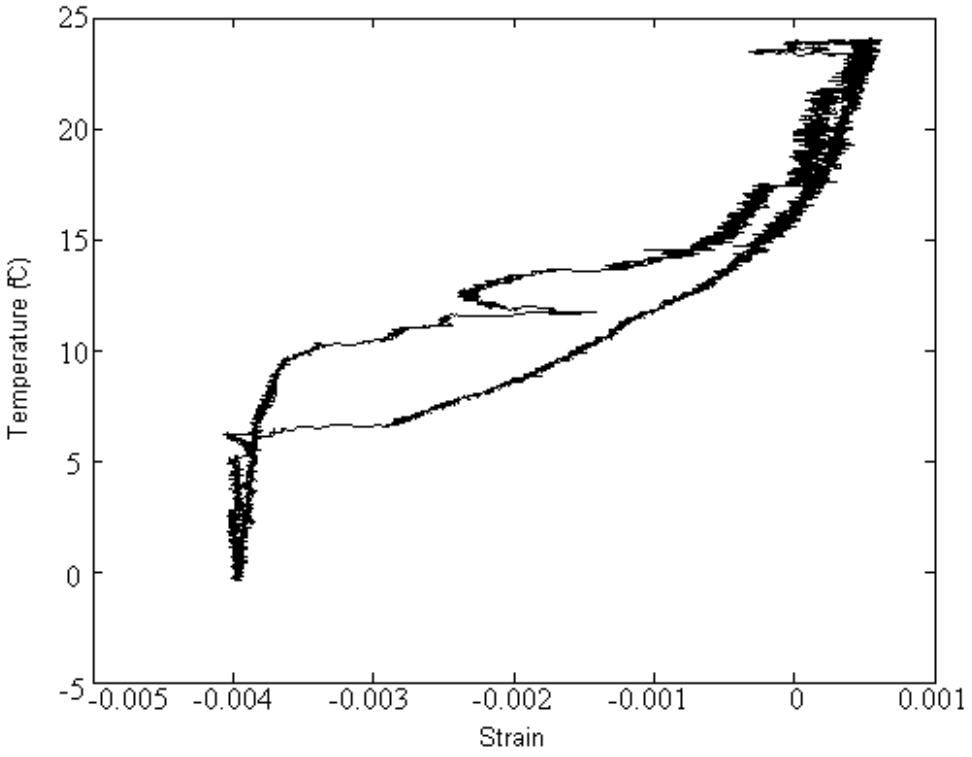

Figure 4.3: Sample NMG3-P8 is applied 2 MPa tension and 2750 G magnetic field at room temperature. Then it is cooled down from austenite to martensite, and then heated back. From the figure, it is hard to figure the accurate values of M_s, M_f, A_s and A_f.

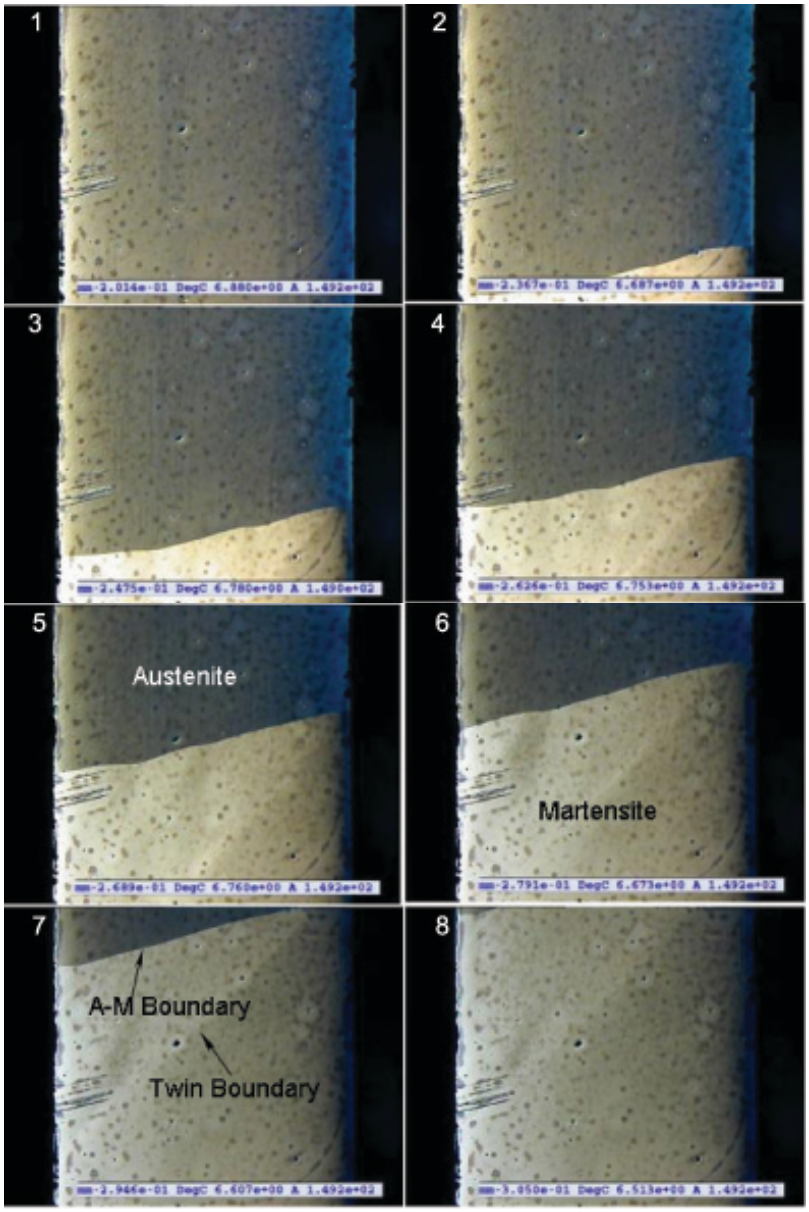

Figure 4.4: The Ni_2MnGa sample is applied with 1 MPa compression and 5500 G horizontal magnetic field and cooled from room temperature. There are two kinds of interfaces can be seen during A-M phase transformation. One is the A-M boundary that about $15^o \sim 20^o$ off horizontal in the figure, the other is the twin boundaries that 45^o off horizontal direction. The number in the corner of each small figure shows the time order during experiment process.

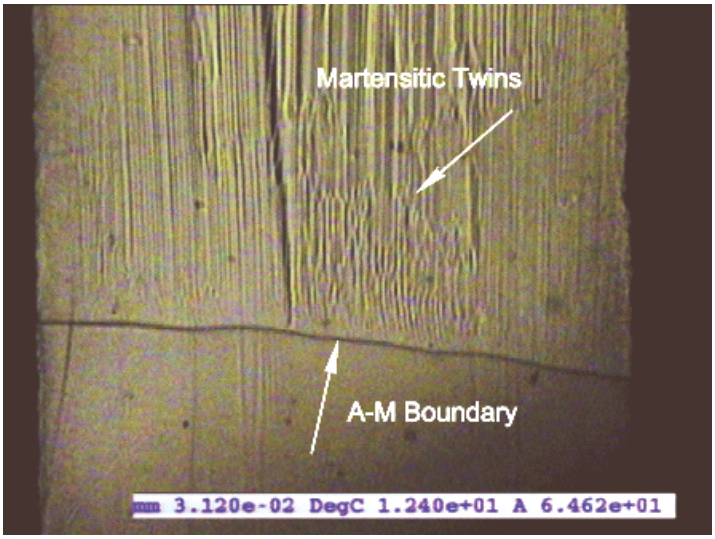

Figure 4.5: The sample is heated up from martensite to austenite under 3 MPa tension with horizontal 2750 G magnetic field, the A-M boundary is near horizontal and the twin boundaries are near vertical.

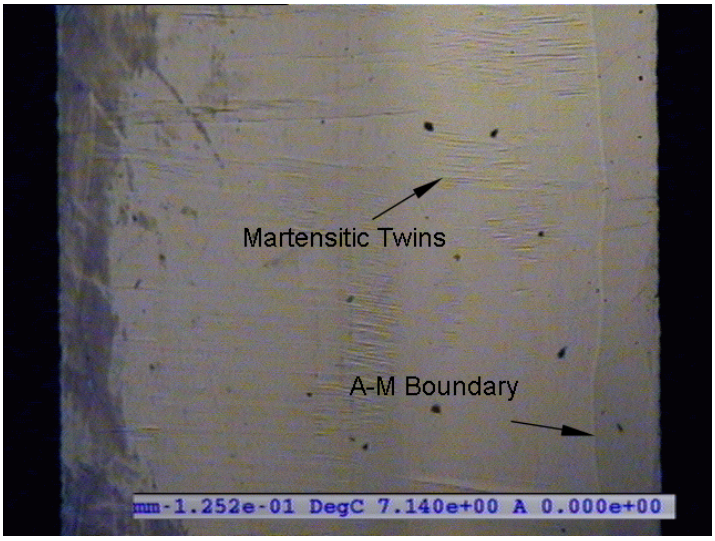

Figure 4.6: The sample is cooled down from austenite to martensite under 1 MPa compression without any magnetic field, the A-M boundary is near vertical and the twin boundaries are near horizontal.

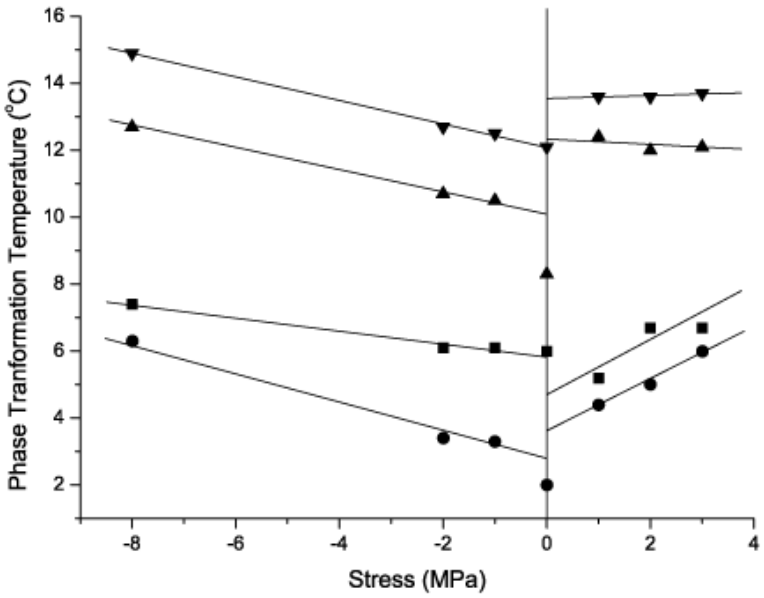

Figure 4.7: The results combination of phase transformation experiments (-8, -2, -1, 1, 2, 3 MPa) and DSC measurement (0 MPa) on Ni_2MnGa single crystal sample is shown in above figure, where the squares represent martensite start temperatures, the rounds represent martensite finish temperatures, upward triangles represent austenite start temperatures and downward triangles represent austenite finish temperatures. The lines are least squares fits and they do not include DSC data.

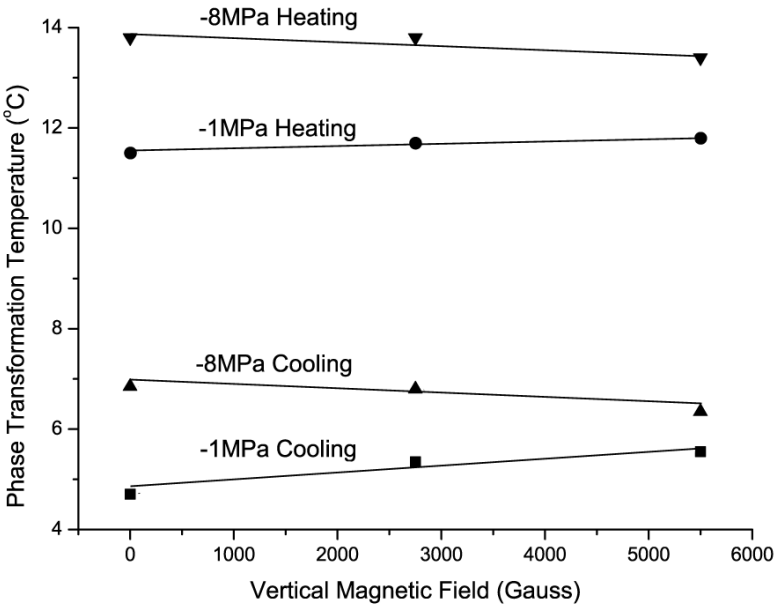

Figure 4.8: The combined effects of vertical magnetic fields and compressions on phase transformation temperatures of single crystal Ni_2MnGa sample is shown in figure above, where squares represent average phase transformations under -1 MPa compression during cooling processes, rounds represent average phase transformations under -1 MPa compression during heating processes, upward triangles represent average phase transformations under -8 MPa compression during cooling processes and downward triangles represent average phase transformations under -8 MPa compression during heating processes.

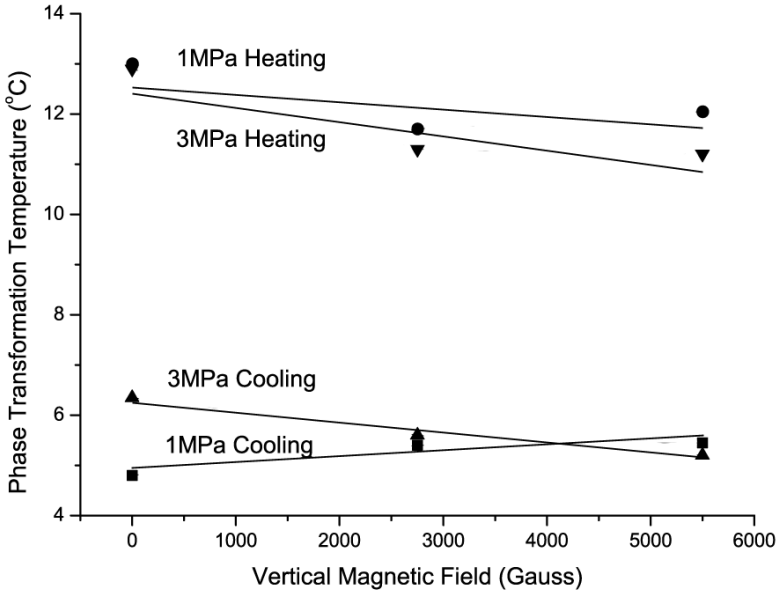

Figure 4.9: The combined effects of vertical magnetic fields and tensions on phase transformation temperatures of single crystal Ni_2MnGa sample is shown in figure above, where squares represent average phase transformations under 1 MPa tension during cooling processes, rounds represent average phase transformations under 1 MPa tension during heating processes, upward triangles represent average phase transformations under 3 MPa tension during cooling processes and downward triangles represent average phase transformations under 3 MPa tension during heating processes.

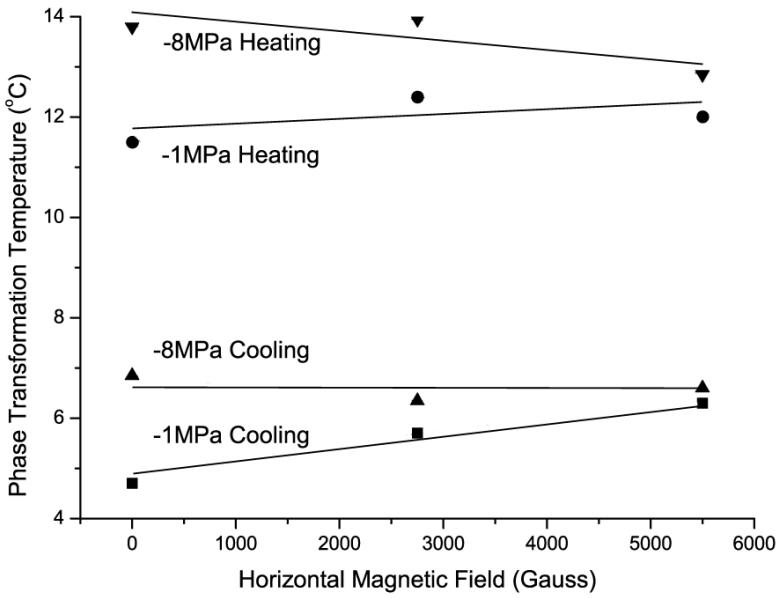

Figure 4.10: The combined effects of horizontal magnetic fields and compressions on phase transformation temperatures of single crystal Ni_2MnGa sample is shown in figure above, where squares represent average phase transformations under -1 MPa compression during cooling processes, rounds represent average phase transformations under -1 MPa compression during heating processes, upward triangles represent average phase transformations under -8 MPa compression during cooling processes and downward triangles represent average phase transformations under -8 MPa compression during heating processes.

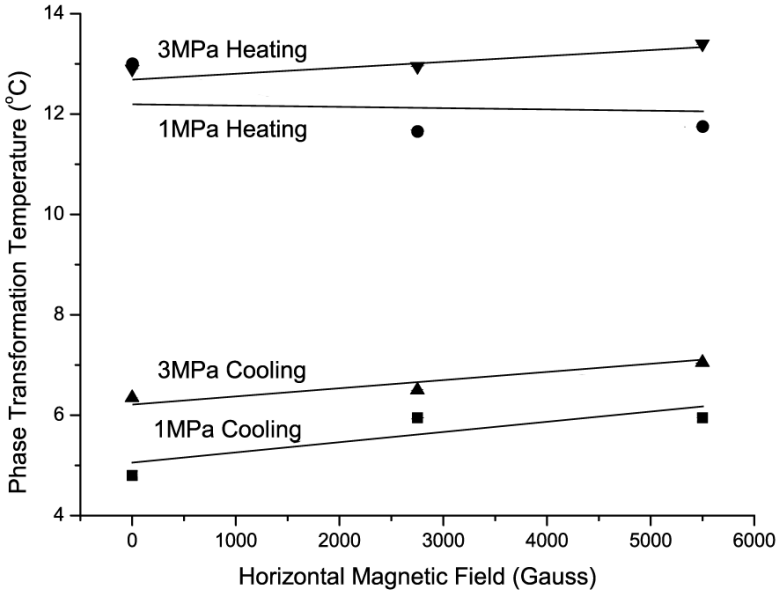

Figure 4.11: The combined effects of horizontal magnetic fields and tensions on phase transformation temperatures of single crystal Ni_2MnGa sample is shown in figure above, where squares represent average phase transformations under 1 MPa tension during cooling processes, rounds represent average phase transformations under 1 MPa tension during heating processes, upward triangles represent average phase transformations under 3 MPa tension during cooling processes and downward triangles represent average phase transformations under 3 MPa tension during heating processes.

Chapter 5

Magneto-Mechanical Experiments

All of our magneto-mechanical experiments were performed with sample NMG3-P9 on Magneto-Mechanical Test Machine (MMTM). The experiments performed include the first set of experiments to apply tension to Ni_2MnGa and measurements of the magnetization of the sample during magnetic field induced variant rearrangement.

5.1 Preliminary Experiments

In order to investigate the relationship between the applied magnetic field, magnetization of the sample and the magnetic field induced strain (MFIS), some preliminary experiments were done before detailed measurements of Ni_2MnGa FSMA magnetic field induced strain behavior were carried out. One of the main goals of these experiments was to determine the best way to transform to a single variant state.

Table 5.1 and Figure 5.1 show the preliminary phase transformation experimental results for a range of conditions. In Figure 5.1, the yellow curve is cooling under -8 MPa and vertical magnetic field, the green one is under -1 MPa and vertical field, the black one is without any stress or field applied, the blue one is under 1 MPa and horizontal field and the red one is for 3 MPa and horizontal field. Table 5.2 and Figure 5.2 give the

preliminary training process experimental results for different training paths. In Figure 5.2, the blue data curve is the result of training path TR1 with TRtest1, the black curve is that of TR2 with TRtest2 and the red one is that of TR3 with TRtest3. These series of experiments in Tables 5.1 and 5.2 were used to determine the best austenite-martensite phase transformation and detwinning process. The best process gives the most uniform single variant state and largest MFIS. From Table 5.1 and Figure 5.1, it is found that phase transformation path PT1 gives the maximum negative strain value and PT5 gives the maximum positive strain value, which agrees with the results of sample NMG3-P8 in Chapter 4. These phase transformation paths made the martensite microstructure after phase A-M transformation nearest to a single variant state under compression and tension, respectively. Variant rearrangement from one single variant microstructure to the other single variant microstructure is the theoretical maximum MFIS, so MFIS performance will be better the closer to a single variant microstructure the sample is after phase transformation. Thus, the A-M phase transformation paths PT1 and PT5 are the best choices among the phase transformation paths considered. Because the CA6 adhesive performance fails under large tension, it was determined that PT1 is the best A-M phase transformation path choice. From Table 5.2 and Figure 5.2, it can be seen that the training process TR4 based on phase transformation path PT1 achieves the maximum training strain value. So, paths PT1 and TR4 were selected as the standard A-M phase transformation and training process paths before each MFIS experiment. In order to eliminate the microstructure influences between the preliminary experiments and later MFIS experiments, after each experiment the sample is transformed back to austenite (room temperature) without any magnetic field or load applied.

To minimize the influences of residual spontaneous magnetization, the sample needs to be demagnetized after detwinning. Two different starting demagnetization magnitudes 3400 Gauss and 1700 Gauss with 1440^{o} spirals to zero field were tried, which are shown in Table 5.3 and in Figure 5.3. And it was found that they provided same demagnetization effects and the 1700 Gauss amplified is expected to have a smaller influence on the detwined microstructure. Thus, starting at 1700 Gauss with 1440^{o} demagnetization spiral was selected as the standard demagnetization path. The demagnetization is performed after before every MFIS experiment starting.

Table 5.4 gives the range of stress levels in the MFIS preliminary experiments and Table 5.5 indicates the magnetic field paths used in the experiments. The details of experimental conditions of MFIS preliminary experiments using the standard A-M phase transformation and training process paths, are shown in Table 5.6. First, magnetic field loadings with circular paths in the *yoz* plane in Figure 3.1 are performed. The 9 different circular field path radii are designed to determine the effect of field magnitude on MFIS. Then, different uniaxial stresses will be applied to the sample to study stress influences on MFIS. Two stress levels for either compression or tension were selected. It was also considered with two different types of magnetic field load paths, in order to study the different magnetic domain conditions and applied field influences on the MFISs. One is the circular magnetic field as mentioned, the other is the magnetic field changing linearly along the lengthwise [001] (vertical) or transverse [010] (horizontal) direction of the rectangular sample. In order to minimize the influence of the field applied rate, the magnetic field control currents were changed as 1 Amps/s and delays of 60 seconds at the field maximum where inserted to allow the apparatus to stablize applied loads.

5.2 Magnetic Field Induced Strains

Magnetic field induced strains are the basis for using ferromagnetic shape memory alloys as actuators. Tickle *et al.* [9] reported 1.3% magnetic field induced strain with a compression stress between 1.4 MPa at -15°C, Heczko *et al.* [10] and Murray *et al.* [11] reported near 6% magnetic field induced strain under 2 MPa compression of 25°C. Recently, Karaca *et al.* [20] reported 5.8% magnetic field induced strain under 5 MPa compression and -95°C, Bechtold *et al.* [21] reported 5.5% magnetic field induced strain under 0.1 MPa compression below 32°C and Malla *et al.* [22] reported 4.1% induced stain without applied stress also below 32°C. The maximum magnetic field induced strain was reported as 10% by Sozinov [23] for the Ni_2MnGa 7M orthorhombic type martensite.

5.2.1 Magnetic Field Induced Strain Experiments

The preliminary experiments described in Table 5.6 are shown in Table 5.7. From these results, it can be seen that large magnitude magnetic field paths, such as paths L3, L4, R17 and R18, provide larger MFISs under small compressive or tensile loads, and the maximum MFIS value was achieved under a small amount of tension and the largest magnitude circular magnetic field path. It was also found that the MFIS values keep increasing slowly and become unchanged after the holding at maximum magnetic field points for about 40 seconds. This strain response delay is caused by load control method limiting the cross head speed, and this time is shorter for smaller MFISs. So in order to obtain consistent MFIS results, the magnetic field was held for at least 60 seconds at the maximum field magnitude points.

Table 5.7 shows that large applied stresses may result in near zero MFIS for any magnitude applied magnetic field. This indicates there is a blocking stress. From the results in Table 5.7, it is also seen that under the same applied stress with linear or rotary magnetic field paths having the same maximum vertical and horizontal field magnitudes, there were slight differences in MFISs. These paths were originally chosen to see if the presence of 180 magnetic domain wall that must occur during the linear paths near zero field influenced to the MFIS process. This does not appear to be a significant effect, although it may account for the differences observed.

Figure 5.4 shows the load changes during a magnetic field induced strain experiment with -0.5 MPa compression and Figure 5.5 shows that with 0.5 MPa tension. And it can be seen that the MFIS processes are consistent under same applied magnetic field path and same applied stress. Here, only small stress level (0.5 MPa) and large magnetic field level (5500 G) experimental results are shown, because the load changes in large stress (3 MPa) and small field (less than 3690 G) experiments were smaller and smoother due to the smaller microstructure changes during MFIS processes. The results of our preliminary experiments are close to other reported results, even though the experimental conditions, during phase transformations and training process may be much different.

Based on the results above, the magnetic field induced strain experiments were designed as shown in Table 5.8. Two reference experiments for the magnetization measurements using the same field paths as in Table 5.8 and without a sample in the fixture were run before and after final MFIS experiments. These results are used to subtract the applied field from the field measurement.

5.2.2 Magnetic Field Induced Strain Experiments Results and Discussion

Relation Between Applied Magnetic Field and MFIS on Sample

Figure 5.6 shows the linear magnetic field paths L1, L2, L3 and L4. Figure 5.7 gives the MFIS result under initial vertical linear field path with 0.5 MPa compression, and Figure 5.8 shows that under initial horizontal field path with 0.5 MPa compression. They are obtained through the same experimental process and the data with relevant experiment segments are marked with capital letters in the figures. Figure 5.9 gives the magnetic field paths of the circular magnetic field paths R11, R12, R17 and R18. And Figures 5.10 and 5.11 show the MFIS results under initial vertical and initial horizontal circular applied magnetic field components with 0.5 MPa compression, respectively. The relation between MFISs and vertical linear applied magnetic field under different applied compressions from 0.5 MPa to 3 MPa is shown in Figure 5.12 and those strains vs. horizontal components of the linear magnetic field under those compressions is shown in Figure 5.13. In Figures 5.12 and 5.13, the blue curves are at 0.5 MPa, the black ones are at 1 MPa, the red ones are at 1.5 MPa and the green ones are at 3 MPa, and colors will be the same for all similar figures. The strains vs. vertical and horizontal circular magnetic field components under different compression conditions are given in Figure 5.14 and 5.15, respectively. The MFIS under 5 MPa compression is too small to be seen (almost 0), so there is no experimental data shown in figures.

Figures 5.16 and 5.17 show the MFIS results under vertical and horizontal linear applied magnetic field components with 0.5 MPa tension, respectively. The MFIS results under

initial vertical and horizontal circular applied magnetic field components with 0.5 MPa tension are given in Figures 5.18 and 5.19. In Figure 5.20, the relation between MFISs and vertical linear applied magnetic field under different applied tensions from 0.5 MPa to 3 MPa is shown, and Figure 5.21 gives those strains vs. horizontal components of the linear magnetic field. Figures 5.22 and 5.23 indicate those strains vs. vertical and horizontal circular magnetic field components under different tension conditions. Also, because of the limitation of the maximum bonding strength of the 3M CA6 instant adhesive, the proposed experiment MFIS10 at 5 MPa tension was not possible.

Under compression, the MFISs due to 3690 G vertical fields are much smaller than those due to 5500 G. A fairly high level horizontal magnetic field is needed to achieve a large MFIS value under compression. But under some tension conditions, even 3690 G vertical fields can produced up to 85% MFISs of those due to 5500 G. Also the MFIS under a tension is always larger than that under the same magnitude compression, and the maximum MFISs under 1 and 1.5 MPa tension are very near the theoretical maximum MFIS values. This indicates that a maximum MFIS will be achieved under tension 5500 G magnetic field. This applies to the design of actuators that need a low level magnetic field to achieve a large value of MFIS.

Comparing the linear field and the circular field results, it is found that there is not a large difference between these MFIS results, but the MFIS responses due to circular field paths are always more symmetric and consistent than due to linear field paths. Also, comparing initially horizontal magnetic field components results with initially vertical magnetic field results, the MFIS-magnetic field loops are very different. This is caused by not only different demagnetization factors in different directions, but also the magnetic easy axis condition of Ni_2MnGa material. For the initially horizontal fields, if we consider the differences between linear field and circular field results, they are similar to the initially vertical magnetic field paths.

Because the MFIS is caused by the variant rearrangement in the Ni_2MnGa single crystal sample, the effects of those on the variants rearrangement need to be measured. We

studied these effects in two ways: by observing the microstructure and by measuring magnetization of the sample.

Microstructure Change During Magnetic Field Rotating

Because the MFIS is directly related to the variant rearrangement in the Ni_2MnGa sample, the microstructure was observed through the MMTM microscope. This microscope employs differential interference contrast (DIC) to make the surface relief due to the microstructure visible.

Figures 5.24 shows the surface microstructure changes during a 5500 G 360^o rotation process under 0.5 MPa tension. The microstructure of horizontal lines in Figure 5.24 image 1 becomes an almost single variant microstructure in Figure 2.11 image 5, which occurs at a 5500 G applied horizontal field. When the field was rotated to vertical, through Figure 5.24 image 2, the horizontal-lines microstructure vanished and a vertical-lines microstructure, which also becomes an almost single variant microstructure in Figure 2.11 image 6, appeared in Figure 5.24 image 3. Then this vertical-lines microstructure was changed back to a horizontal-lines microstructure through Figure 5.24 image 4 to 5.24 image 5, as the field changed to horizontal and it returned to vertical-lines in Figure 5.24 image 7 when the field rotated to vertical. From the figures, it can also be seen that the sample became narrower when the applied magnetic field is rotated to horizontal, and became wider when the field is changed to vertical. All of these observations agree with the FSM mechanism discussed previously in Chapter 2.

The surface microstructure changes during a 5500 G 360^o rotation field path under 0.5 MPa compression are given in Figure 5.25. Here, in Figure 5.25 image 1 the vertical-lines structure can be seen clearly, but in Figure 5.25 image 2, the horizontal-lines structure can not be seen clearly under the same 5500 G applied horizontal field. This indicates that the microstructure of the sample is not fully rearranged to another single variant condition as it was under tension. When the applied field is vertical, the vertical-lines

structure returned, and the horizontal-lines structure was not remained under a vertical field. This may explain why the MFIS is less than under tension. It can be also seen that sample became narrower under compression for horizontal fields and became wider for vertical fields, but the changes are much smaller than those for 0.5 MPa tension (as expected by the strain measurements).

If we look at the surface microstructure changes during a rotating field path under 3 MPa compression as shown in in Figure 5.26, it can be seen that there is no microstructure changes observed, which means that there is primarily a single variant in this part of sample and that the variant was not rearranged by the magnetic field. This agrees with the value of MFIS under 3 MPa compression that is much smaller than under 0.5 MPa compression. As expected from the lack of strain measured, there is also no sample width change observed.

Relation Between Applied Magnetic Field and Magnetization of Sample

The MFIS is also connected to the magnetization of the sample, so measurement of the magnetization is important. In the model of the magnetic field induced strain process, the calculation of the total magnetic energy in (2.27) is a key part. Equation (2.27) shows that not only applied magnetic field, but also demagnetization field and magnetization of the sample influence the result. The demagnetization field of the sample is related to the applied field and the demagnetization factors of the sample. The magnetization of the sample is determined by applied magnetic field, the microstructure and the saturation magnetization of the material. So understanding the relation between applied magnetic field, demagnetization field and magnetization of the sample will help us understand the magnetic energy. For an example, under some compression levels, a 5500 G magnetic field can almost magnetize the sample to saturation in vertical direction but may not in the horizontal direction because of the demagnetization factor differences in the different directions. This may be one of the reasons why even under some small compression levels, the MFIS is much smaller than the maximum theoretical

possible value for our sample geometry.

In the MMTM, the magnetization measurement is performed by measuring the stray field produced by the sample in the fixture using Hall probes. The applied field is subtracted from the field measurement with the sample to obtain the stray field [41]. A series of referential experiments without a sample in the fixture, which have the same magnetic field paths as the MFIS experiments, are run before and after the MFIS experiments to obtain the applied field measurements for this substraction process.

Figure 5.27 shows the vertical magnetization of sample vs. vertical component of the applied field under compressions of 0.5 to 3 MPa on the linear portion of the field path. As in the figures of MFIS vs. applied magnetic field, the blue curves are the ones under 0.5 MPa stress, the black ones are under 1 MPa, the red ones are under 1.5 MPa and the green ones are under 3 MPa on all figures. Here, in order to clearly show the curves, only magnetic field paths of 5500 G magnitudes are shown. The vertical magnetization of sample vs. vertical component on a circular field path under different compressions is shown in Figure 5.28. The vertical magnetization of sample vs. vertical field component on linear field path under different tensions is given in Figure 5.29 and the vertical magnetization of sample vs. vertical component on a circular field path under different tensions is shown in Figure 5.30. From the figures, it can be seen that under compression and vertical 5500 G magnetic field, the Ni_2MnGa sample almost reached saturation. For linear field paths, the magnetization-magnetic field loops have similar hysteresis, which are much smaller than those during circular field paths. For circular field conditions, not only make hysteresis loops larger, but they also depend on compression level. Under tension and vertical 5500 G field, the sample only reached saturated magnetization conditions with 0.5, 1 and 1.5 MPa, but not with 3 MPa. Thus, under large applied tension, with applied field along the longitudinal direction that with a larger demagnetization factor, the sample did not reach the saturation under a 5500 G field and a larger magnitude field is needed to saturate the sample. This might also result in a larger MFIS. Comparing the linear and circular magnetic field paths under the same tension, it is found that the hysteresis loops are quite different. The hysteresis

differences under same stress between linear and circular magnetic field paths come from the differences of magnetic domains under linear or circular field paths and may also be affected by the magnetic anisotropy of the material. These differences may be the main reason for the differences between MFISs under the same stress with linear and circular field paths.

Figure 5.31 shows the horizontal magnetization of sample vs. horizontal of component of applied field of a linear field path under different compressions and Figure 5.32 gives this for circular field paths. Figure 5.33 and Figure 5.34 are the equivalent figures for applied tension. From these figures, it can be seen that under both 0.5 and 1 MPa compressions and all 0.5, 1 and 1.5 MPa tensions, the sample was almost saturated, and it is interesting that the magnetization-magnetic field loops under different stresses are similar for the same linear field or circular field path. For these results, the circular field results have much larger hysteresis than those of linear field. And under 1.5 and 3 MPa compressions and 3 MPa tension, the sample is far from saturated. The maximum horizontal magnetization is smaller than the vertical magnetization under same stress conditions. Similar to the results for reaching the saturation magnetization, the circular field paths always gives larger hysteresis than the linear field path.

From the figures discussed above, it appears that the magnetization vector favors vertical direction more than horizontal direction. This is because of the different demagnetization factors in different directions. It also appears that under the circular magnetic field paths, the magnetic anisotropy causes the magnetization to have a much larger hysteresis than that of linear magnetic field paths under all stress conditions.

Relation Between Magnetization of Sample and MFIS

From the discussions in above subsections, it is clear that the MFIS may be critically influenced by the magnetization of sample. Under a certain level of applied stress, the

sample saturation is a necessary requirement that the sample can attain a single variant microstructure, and this will determine the maximum possible MFIS during variant rearrangement. So we need to consider the relationship between the magnetization of sample and the MFIS under different applied magnetic field and stress conditions.

Figures 5.35 shows the MFIS vs. vertical magnetization component of sample under applied linear field paths, Figure 5.36 shows the same for applied circular fields, Figure 5.37 shows applied linear field paths and different tensions and Figure 5.38 shows tension and applied circular field paths. The relationship between MFISs and horizontal magnetization component of sample under similar stresses and magnetic field conditions are given in Figures 5.39 - 5.42. The first observation is that the sample is almost saturated vertically under all compression conditions, but the sample is far from saturated horizontally under 1.5 and 3 MPa. The MFISs under these loadings are much smaller than those of 0.5 and 1 MPa, and under 0.5 and 1 MPa compression, when the sample is saturated in both directions. At the same time, under 1 and 1.5 MPa tensions, the sample was almost saturated in both directions, and MFISs are same and larger than that of 0.5 MPa tension. And all 0.5, 1 and 1.5 MPa tension results are larger than those of maximum compression MFIS value under 0.5 MPa. Second, the values of MFIS only increase dramatically when the magnetization of sample reaches a certain magnitude (about 400 emu/cm^3) and they decrease rapidly when the magnetization of sample is less than 200 emu/cm^3 under most of stress conditions, which introduces the hysteresis in the MFIS-magnetization results. The linear relationship between MFIS and magnetization in these regions of rapid change is expected based on the model in Chapter 2.

Under compression, this result agrees with others [8-10, 20-22]. But there are no published results for tension. It can be also seen that, under 1 MPa and 1.5 MPa tension, the maximum MFISs are very near to the theoretically predicted MFIS (6.01%) between two single variant structures. These results can be explained by the magnetic properties of the sample. For the long rectangularly shaped sample NMG3-P9, the ratio of

demagnetization factors in longitude direction (vertical) and transverse direction (horizontal) is only about 0.2, that is to say, the sample is much easier magnetized along vertical direction than horizontal direction. The minimum value of applied horizontal field H_s, which can magnetize sample to saturation magnetization in Figure 2.11 image 5, will be much larger than the required vertical field H_s in Figure 2.11 image 6. From Figure 2.11, it can be seen that the compression and vertical field will help each other to achieve single variant to satisfy the minimum free energy requirement and compression and horizontal field will compete with each other and not reach a single variant state in Figure 2.11 image 5 under the applied field less than H_s. Then it will be hard to obtain MFISs near maximum possible MFIS result. And for applied tension, even the required applied magnetic field is smaller than H_s, because of the tension on the sample, a single variant structure (Figure 2.11 image 5) will be favored under the requirement of the minimum free energy. Then when the applied vertical magnetic field is large enough to saturate the sample in the vertical direction, even under applied tension, the microstructure of sample will still be rearranged to the single variant structure (Figure 2.11 image 6). Because the tension and vertical field compete with each other, when the tension is larger than a certain value, single variant structure in Figure 2.11 image 6 will not be possible any more. Thus the MFIS under 3 MPa tension is much less than that under 0.5 - 1.5 MPa.

Comparison of Theoretical and Experimental Results

By using the simple model in Section 2.4.4 with material parameters in Section 2.5.2, the calculated MFIS vs. vertical applied magnetic field for field path R17 under 0.5 MPa compression are compared to experimental results with same field and stress conditions in Figure 5.43. The comparison of MFIS vs. horizontal applied magnetic field component is given in Figure 5.44. A comparison of MFIS vs. vertical applied magnetic field for field path R18 under 1 MPa tension is shown in Figure 5.45 and MFIS vs. horizontal applied field is given in Figure 5.46. Comparing Figures 5.43 and 5.45 or Figures 5.44 and 5.46, it is found that MFISs vs. magnetic field loops always fit model

calculation results better for tension conditions than for compression conditions. Note that this simple model can not show any hysteresis but the experimental results have large hysteresis.

By using the simple model in Section 2.4.4 with material parameters in Section 2.5.2 again, the model prediction of MFISs vs. sample vertical or horizontal magnetization component loops under 0.5 MPa compression and 1 MPa tension with the maximum MFISs are compared with the experimental measurements in Figures 5.47-5.50. Comparing Figures 5.47 and 5.49 or Figures 5.48 and 5.50 again, it is also found that MFISs vs. magnetization component loops fit model calculation results better for tension conditions than for compression conditions and the experimental results have large hysteresis loops. The calculation fits the magnetization values in the increasing parts of the curves much better than where the magnetization values are decreasing. If we want a better simulation of the MFIS behaviors of Ni_2MnGa material, we need to figure out how to model the hysteresis in FSM behavior.

Blocking Stress and Work Output Under Compression and Tension

Based on our experimental data, the relation between MFIS and stress under fields of 3690 and 5500 G are compared with other reported values in Figure 5.51. Here, all MFIS values of our results are the maximum MFIS value in each loading cycle. From Figure 5.51, it can be seen that the blocking compression stress of sample NMG3-P9 under 5500 G applied magnetic field is about 5 MPa, which is near the result of Heczko *et al*. [10]. For the tension part, we predict the blocking tension stress of long rectangular sample NMG3-P9 under 5500 G applied field is about 7 MPa, which larger than that of compression. It is also found that the MFIS value vs. compression stress curves have the similar slopes in the near vertical part for our results, results of Heczko *et al*. and Karaca *et al*. [20], they are offset parallel to left with larger applied magnetic fields. And the result of Tickle *et al*. [9] is also offset parallel to left comparing with near horizontal part of our result with larger applied fields. There are many possible explanations,

including alloy composition and experimental method differences. Such as, the results of Tickle *et al*. were obtained from $Ni_{51.3}Mn_{24.0}Ga_{24.7}$ alloy under 12000 G applied magnetic field and -15 °C, the results of Heczko *et al*. were from $Ni_{48.0}Mn_{31.0}Ga_{21.0}$ alloy under 11300 G applied magnetic field and near room temperature, the results of Karaca *et al*. were from $Ni_{51.1}Mn_{24.0}Ga_{24.9}$ under 15000 G applied magnetic field and -95 °C and our results were from $Ni_{49.0}Mn_{28.0}Ga_{23.0}$ under -5 °C.

If we consider the work output results in Figure 5.52, it can be seen that a larger applied magnetic field will produce larger work output on the Ni_2MnGa material. The work output curve of a long rectangular shape Ni_2MnGa sample under tension covers a much larger area than that for the same conditions under compression. Under tension, the same work output is achieved with a smaller magnetic field. In addition, the tension geometry makes it easier to construct a coil around the material and thus the tension application has several advantages for sensors and actuators.

Table 5.1: The experimental conditions of preliminary phase transformation (PT) tests are shown. Here, V in the field column means vertical magnetic field, H means horizontal magnetic field, and they are same in other tables.

A-M Phase Transformation 20 °C (Austenite) → -5 °C (Martensite)				
Test Name	PT Path	Stress (MPa)	Field (Gauss)	PT Strain
PTtest1	PT1	-8	5500 (V)	-0.0345
PTtest2	PT2	-1	5500 (V)	-0.0330
PTtest3	PT3	0	0	0.0034
PTtest4	PT4	1	5500 (H)	0.0125
PTtest5	PT5	3	5500 (H)	0.0170

Table 5.2: The experimental conditions of preliminary detwinning processes, which is the training processes on the sample, are shown.

Test Name	Training Path	PT Path	Field (Gauss)	Stress (MPa)	Training Strain
TRtest1	TR1	PT1	Unchanged	→ -0.5	0.0025
TRtest2	TR2	PT1	→ 5500 (H)	→ -0.5	0.0045
TRtest3	TR3	PT1	→ 5500 (H)	→ 3	0.036

Table 5.3: Different demagnetization loops and their influences on the magnetization of the sample after demagnetization process are shown in table below.

Demag. Magn.	Mag. Before Demag.	Mag. After Demag.	Stress
1700 G	230 emu/cm^3	20 emu/cm^3	0.25 MPa
3400 G	230 emu/cm^3	18 emu/cm^3	0.6 MPa

Table 5.4: Two compression magnitudes and two tension magnitudes were selected to perform preliminary MFIS experiments.

Stress Path	Stress Details (MPa)
C1	-0.5
C2	-3
T1	0.5
T2	3

Table 5.5: Eighteen groups of circular magnetic field paths and four groups of linear magnetic field paths were selected to perform preliminary MFIS experiments.

Field Path	Field Path Details (Gauss)
R1	0 → 615 (V) $\circlearrowleft^{90}$ -615 (H) $\circlearrowleft^{90}$ -615 (V) $\circlearrowleft^{90}$ 615 (H) $\circlearrowleft^{90}$ 615 (V) → 0
R2	0 → 615 (H) $\circlearrowleft^{90}$ 615 (V) $\circlearrowleft^{90}$ -615 (H) $\circlearrowleft^{90}$ -615 (V) $\circlearrowleft^{90}$ 615 (H) → 0
R3	0 → 1230 (V) $\circlearrowleft^{90}$ -1230 (H) $\circlearrowleft^{90}$ -1230 (V) $\circlearrowleft^{90}$ 1230 (H) $\circlearrowleft^{90}$ 1230 (V) → 0
R4	0 → 1230 (H) $\circlearrowleft^{90}$ 1230 (V) $\circlearrowleft^{90}$ -1230 (H) $\circlearrowleft^{90}$ -1230 (V) $\circlearrowleft^{90}$ 1230 (H) → 0
R5	0 → 1845 (V) $\circlearrowleft^{90}$ -1845 (H) $\circlearrowleft^{90}$ -1845 (V) $\circlearrowleft^{90}$ 1845 (H) $\circlearrowleft^{90}$ 1845 (V) → 0
R6	0 → 1845 (H) $\circlearrowleft^{90}$ 1845 (V) $\circlearrowleft^{90}$ -1845 (H) $\circlearrowleft^{90}$ -1845 (V) $\circlearrowleft^{90}$ 1845 (H) → 0
R7	0 → 2460 (V) $\circlearrowleft^{90}$ -2460 (H) $\circlearrowleft^{90}$ -2460 (V) $\circlearrowleft^{90}$ 2460 (H) $\circlearrowleft^{90}$ 2460 (V) → 0
R8	0 → 2460 (H) $\circlearrowleft^{90}$ 2460 (V) $\circlearrowleft^{90}$ -2460 (H) $\circlearrowleft^{90}$ -2460 (V) $\circlearrowleft^{90}$ 2460 (H) → 0
R9	0 → 3075 (V) $\circlearrowleft^{90}$ -3075 (H) $\circlearrowleft^{90}$ -3075 (V) $\circlearrowleft^{90}$ 3075 (H) $\circlearrowleft^{90}$ 3075 (V) → 0
R10	0 → 3075 (H) $\circlearrowleft^{90}$ 3075 (V) $\circlearrowleft^{90}$ -3075 (H) $\circlearrowleft^{90}$ -3075 (V) $\circlearrowleft^{90}$ 3075 (H) → 0
R11	0 → 3690 (V) $\circlearrowleft^{90}$ -3690 (H) $\circlearrowleft^{90}$ -3690 (V) $\circlearrowleft^{90}$ 3690 (H) $\circlearrowleft^{90}$ 3690 (V) → 0
R12	0 → 3690 (H) $\circlearrowleft^{90}$ 3690 (V) $\circlearrowleft^{90}$ -3690 (H) $\circlearrowleft^{90}$ -3690 (V) $\circlearrowleft^{90}$ 3690 (H) → 0
R13	0 → 4305 (V) $\circlearrowleft^{90}$ -4305 (H) $\circlearrowleft^{90}$ -4305 (V) $\circlearrowleft^{90}$ 4305 (H) $\circlearrowleft^{90}$ 4305 (V) → 0
R14	0 → 4305 (H) $\circlearrowleft^{90}$ 4305 (V) $\circlearrowleft^{90}$ -4305 (H) $\circlearrowleft^{90}$ -4305 (V) $\circlearrowleft^{90}$ 4305 (H) → 0
R15	0 → 4920 (V) $\circlearrowleft^{90}$ -4920 (H) $\circlearrowleft^{90}$ -4920 (V) $\circlearrowleft^{90}$ 4920 (H) $\circlearrowleft^{90}$ 4920 (V) → 0
R16	0 → 4920 (H) $\circlearrowleft^{90}$ 4920 (V) $\circlearrowleft^{90}$ -4920 (H) $\circlearrowleft^{90}$ -4920 (V) $\circlearrowleft^{90}$ 4920 (H) → 0
R17	0 → 5500 (V) $\circlearrowleft^{90}$ -5500 (H) $\circlearrowleft^{90}$ -5500 (V) $\circlearrowleft^{90}$ 5500 (H) $\circlearrowleft^{90}$ 5500 (V) → 0
R18	0 → 5500 (H) $\circlearrowleft^{90}$ 5500 (V) $\circlearrowleft^{90}$ -5500 (H) $\circlearrowleft^{90}$ -5500 (V) $\circlearrowleft^{90}$ 5500 (H) → 0
L1	0 → 3690 (V) → 0 → -3690 (H) → 0 → -3690 (V) → 0 → 3690 (H) → 0
L2	0 → 3690 (H) → 0 → 3690 (V) → 0 → -3690 (H) → 0 → -3690 (V) → 0
L3	0 → 5500 (V) → 0 → -5500 (H) → 0 → -5500 (V) → 0 → 5500 (H) → 0
L4	0 → 5500 (H) → 0 → 5500 (V) → 0 → -5500 (H) → 0 → -5500 (V) → 0

Table 5.6: The experimental conditions of preliminary magnetic field induced strain tests are shown. And all these tests were followed by training path TR3 after sample NMG3-P9 was transformed to martensite with path PT1 and held at -5 °C.

Test Name	Combination of Stress and Magnetic Field Paths
PMFIS1	C1 + R1 + R3 + R5 + R7 + R9 + R11 + R13 + R15 + R17
PMFIS2	T1 + R2 + R4 + R6 + R8 + R10 + R12 + R14 + R16 + R18
PMFIS3	C1 + L3 + R17 + L3 + R17
PMFIS4	C2 + L3 + R17 + L3 + R17
PMFIS5	T1 + L4 + R18 + L4 + R18
PMFIS6	T2 + L4 + R18 + L4 + R18

Table 5.7: The results of preliminary magnetic field induced strain experiments are shown.

Without Holding at Maximum Magnetic Field Points			
Exp. Condition	MFIS Value	Exp. Condition	MFIS Value
PMFIS1 C1 + R1	0	PMFIS2 T1 + R2	0
PMFIS1 C1 + R3	0	PMFIS2 T1 + R4	0.0001
PMFIS1 C1 + R5	0.0001	PMFIS2 T1 + R6	0.0002
PMFIS1 C1 + R7	0.0003	PMFIS2 T1 + R8	0.0005
PMFIS1 C1 + R9	0.0042	PMFIS2 T1 + R10	0.0083
PMFIS1 C1 + R11	0.0175	PMFIS2 T1 + R12	0.0125
PMFIS1 C1 + R13	0.0200	PMFIS2 T1 + R14	0.0225
PMFIS1 C1 + R15	0.0317	PMFIS2 T1 + R16	0.0333
PMFIS1 C1 + R17	0.0350	PMFIS2 T1 + R18	0.0450
With 60s Holding at Maximum Magnetic Field Points			
PMFIS3 C1 + L3 (1st)	0.0370	PMFIS5 T1 + L4 (1st)	0.0545
PMFIS3 C1 + R17 (1st)	0.0380	PMFIS5 T1 + R18 (1st)	0.0555
PMFIS3 C1 + L3 (2nd)	0.0370	PMFIS5 T1 + L4 (2nd)	0.0545
PMFIS3 C1 + R17 (2nd)	0.0380	PMFIS5 T1 + R18 (2nd)	0.0555
PMFIS4 C2 + L3 (1st)	0.0022	PMFIS6 T2 + L4 (1st)	0.0100
PMFIS4 C2 + R17 (1st)	0.0027	PMFIS6 T2 + R18 (1st)	0.0105
PMFIS4 C2 + L3 (2nd)	0.0022	PMFIS6 T2 + L4 (2nd)	0.0100
PMFIS4 C2 + R17 (2nd)	0.0027	PMFIS6 T2 + R18 (2nd)	0.0105

Table 5.8: Final magnetic field induced strain experimental conditions were selected as shown.

Test Number	PT Path	Training Path	Stress (MPa)	Magnetic Field Paths
MFIS1	PT1	TR4	-0.5	L1 + R11 + L3 + R17
MFIS2	PT1	TR3	-1	L1 + R11 + L3 + R17
MFIS3	PT1	TR3	-1.5	L1 + R11 + L3 + R17
MFIS4	PT1	TR3	-3	L1 + R11 + L3 + R17
MFIS5	PT1	TR3	-5	L1 + R11 + L3 + R17
MFIS6	PT1	TR3	0.5	L2 + R12 + L4 + R18
MFIS7	PT1	TR3	1	L2 + R12 + L4 + R18
MFIS8	PT1	TR3	1.5	L2 + R12 + L4 + R18
MFIS9	PT1	TR3	3	L2 + R12 + L4 + R18
MFIS10	PT1	TR3	5 (if possible)*	L2 + R12 + L4 + R18

*Depends on the maximum available adhesive strength of CA6 glue.

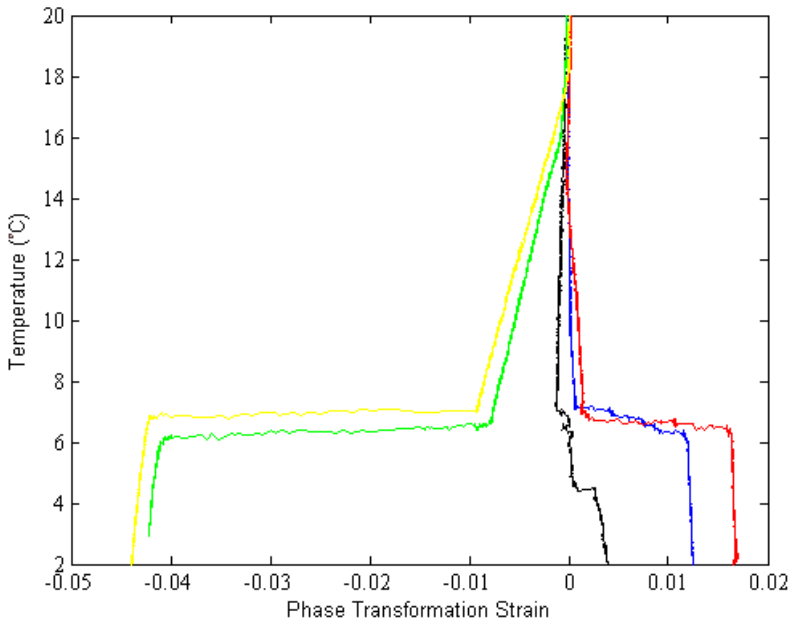

Figure 5.1: The phase transformation strain results vs. experimental temperature of sample NMG3-P9 during different preliminary phase transformation experiments. The yellow curve indicates the sample cooling process of test PTtest1 under -8 MPa and vertical magnetic field, the green one indicates that of PTtest2 under -1 MPa and vertical field, the black one shows that of PTtest3 without any stress or field applied, the blue one indicates that of PTtest4 under 1 MPa and horizontal field and the red one shows that of PTtest5 under 3 MPa and horizontal field.

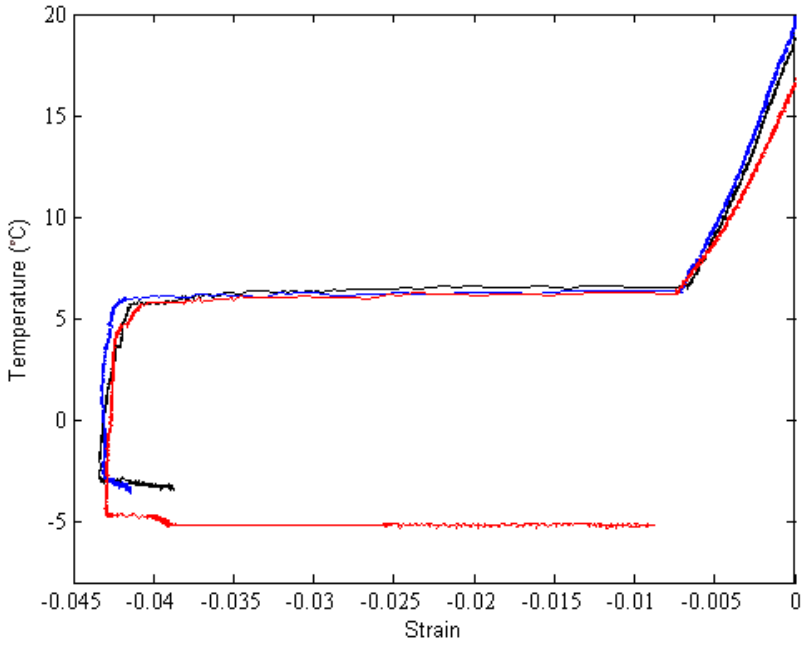

Figure 5.2: The different detwinning (training) processes based on the same phase transformation path PT1 are shown. The blue curve is the result of training path TR1 with TRtest1, the black curve is that of TR2 with TRtest2 and the red one is that of TR3 with TRtest3.

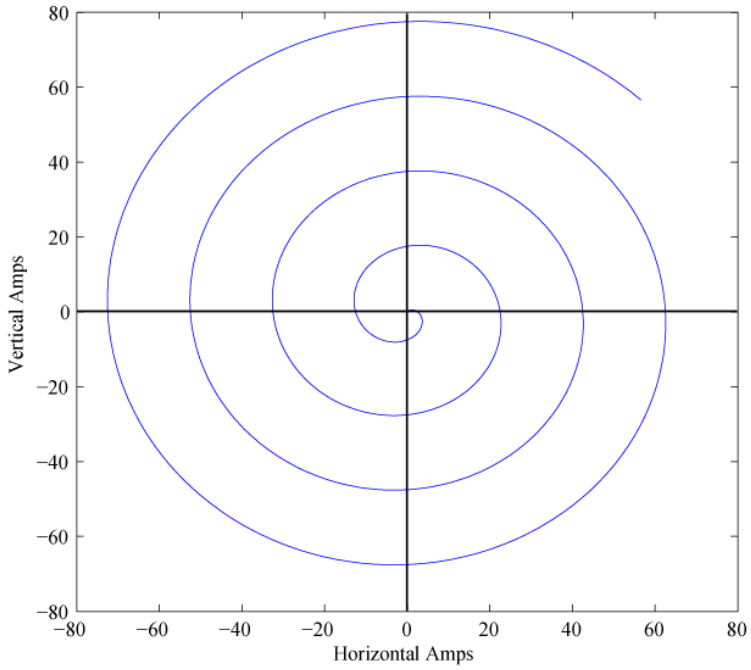

Figure 5.3: The demagnetization spirals are made of four cycles (1440°) that take 60 seconds.

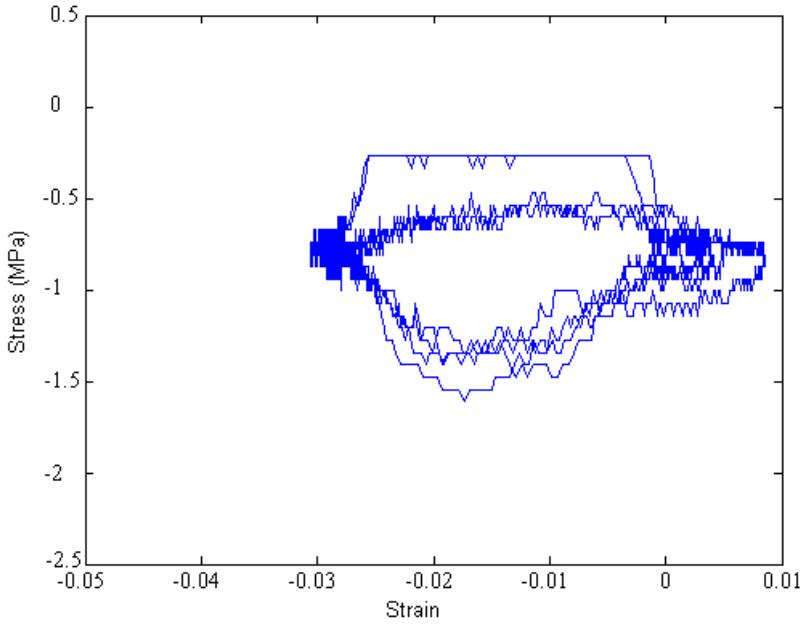

Figure 5.4: In order to check if the stress fluctuating is consistent during the holding process in the same magnetic field paths, stress fluctuating in test PMFIS3 is shown.

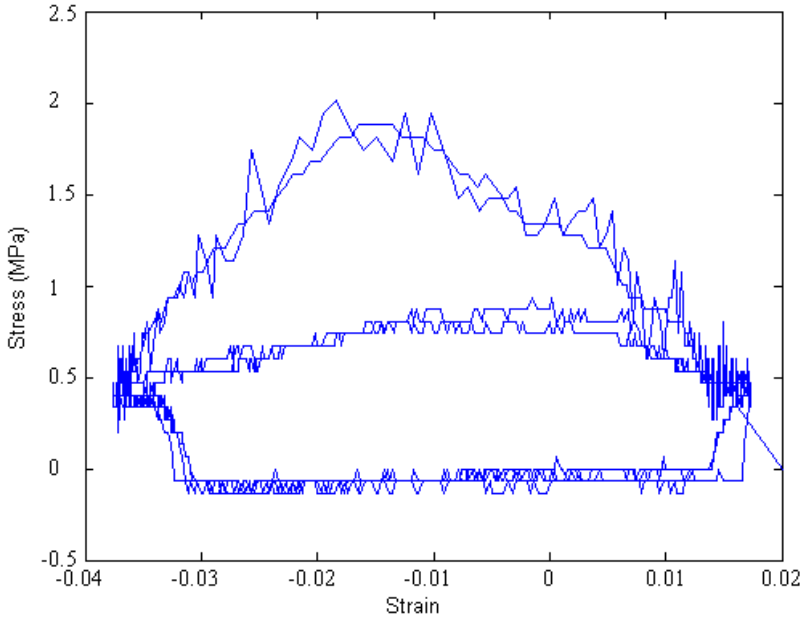

Figure 5.5: In order to check if the stress fluctuating is consistent during the holding process in the same magnetic field paths, stress fluctuating in test PMFIS5 is shown.

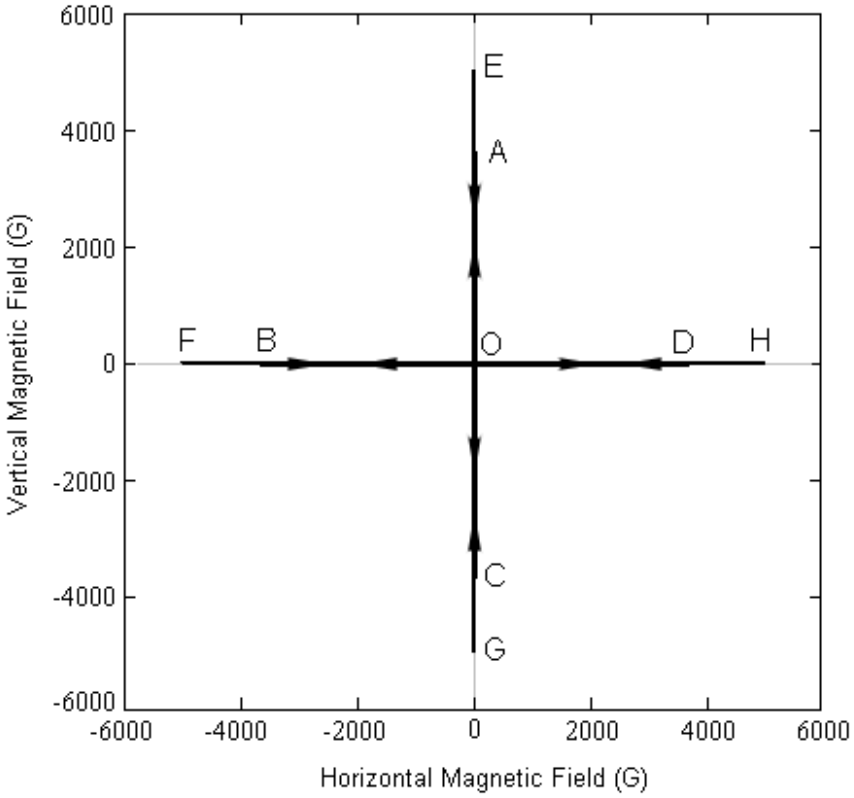

Figure 5.6: The linear magnetic field paths are shown here. For field path L1, it goes from O to A to O to B to O to C to O to D to O. For field path L2, it goes from O to D to O to A to O to B to O to C to O. For field path L3, it goes from O to E to O to F to O to G to H to O. For field path L4, it goes from O to H to O to E to O to F to O to G to O.

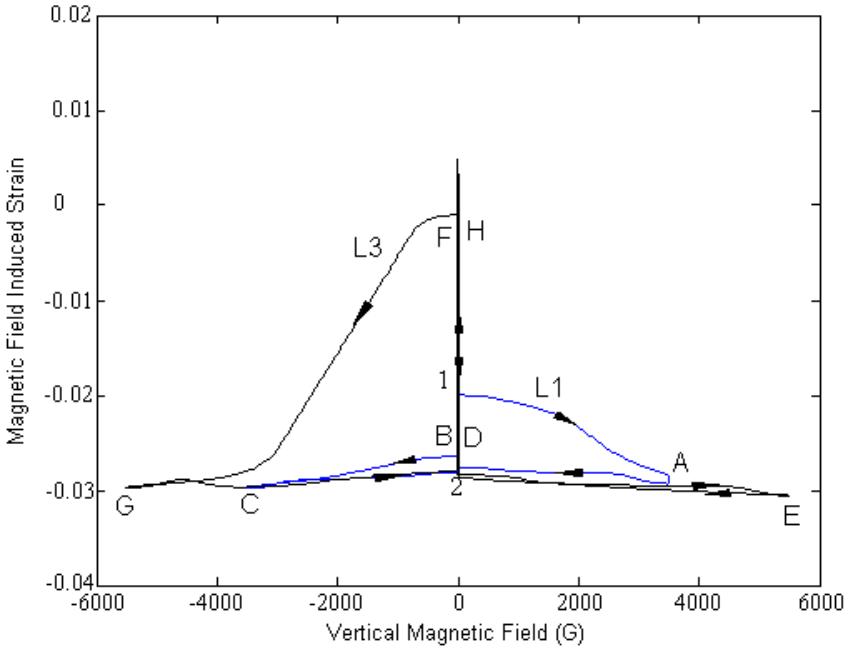

Figure 5.7: The result of magnetic field induced strain vs. vertical magnetic field in the linear field part of test MFIS1 is shown here. The blue curve shows the MFIS path of 3690 G initial vertical linear field under 0.5 MPa compression, and the black curve shows the that of 5500 G initial vertical linear field under 0.5 MPa compression. The points marked with a capital letter are the same ones in Figure 5.4. The curve of L1 starts from point 1, and curve L3 starts from point 2.

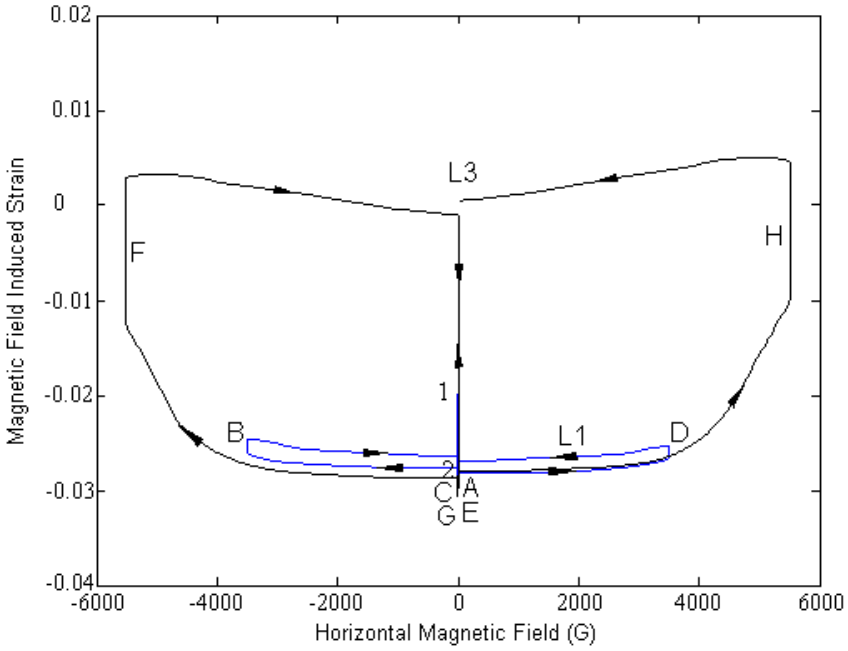

Figure 5.8: The result of magnetic field induced strain vs. horizontal magnetic field in the linear field part of test MFIS1 is shown here.The blue curve shows the MFIS path of 3690 G initial horizontal linear field under 0.5 MPa compression, and the black curve shows the that of 5500 G initial horizontal linear field under 0.5 MPa compression. The capital letter marked points are the same ones in Figure 5.4. The curve of L1 starts from point 1, and curve L3 starts from point 2.

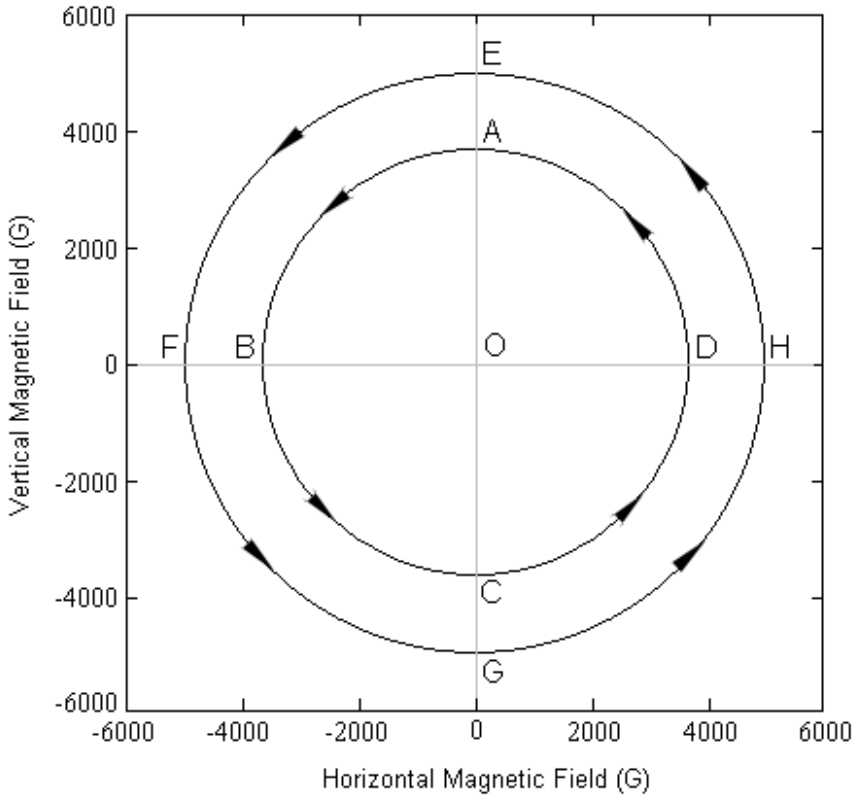

Figure 5.9: The circular magnetic field paths are shown here. For field path R11, it rotates from A to B to C to D. For field path R12, it rotates from D to A to B to C. For field path R17, it rotates from E to F to G to H. For field path R18, it rotates from H to E to F to G.

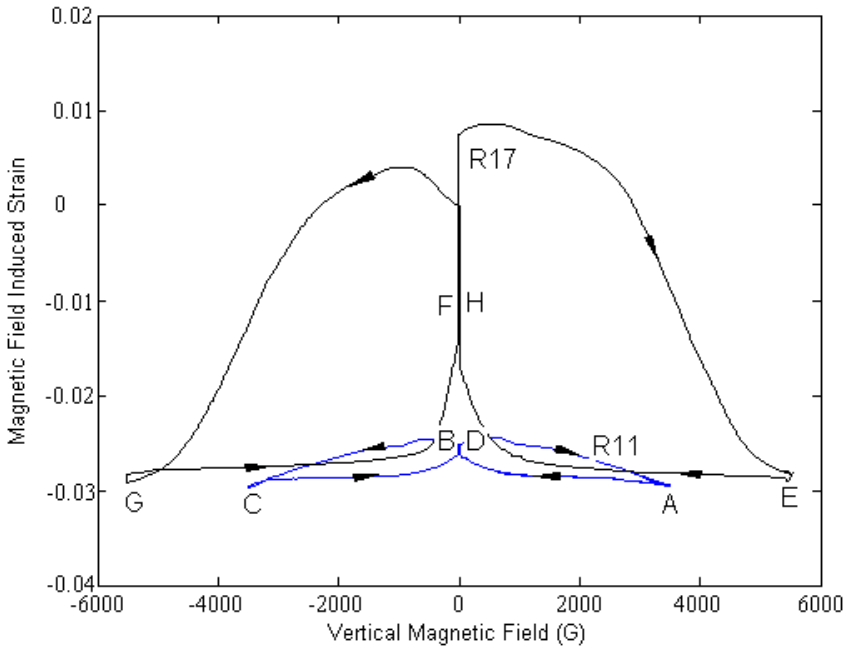

Figure 5.10: The result of magnetic field induced strain vs. vertical magnetic field in the circular field part of test MFIS1 is shown here. The blue curve shows the MFIS path of 3690 G vertical circular field under 0.5 MPa compression, and the black curve shows the that of 5500 G vertical circular field under 0.5 MPa compression. The capital letter marked points are the same ones in Figure 5.9. The R11 curve starts from point A and R17 curve starts from point E.

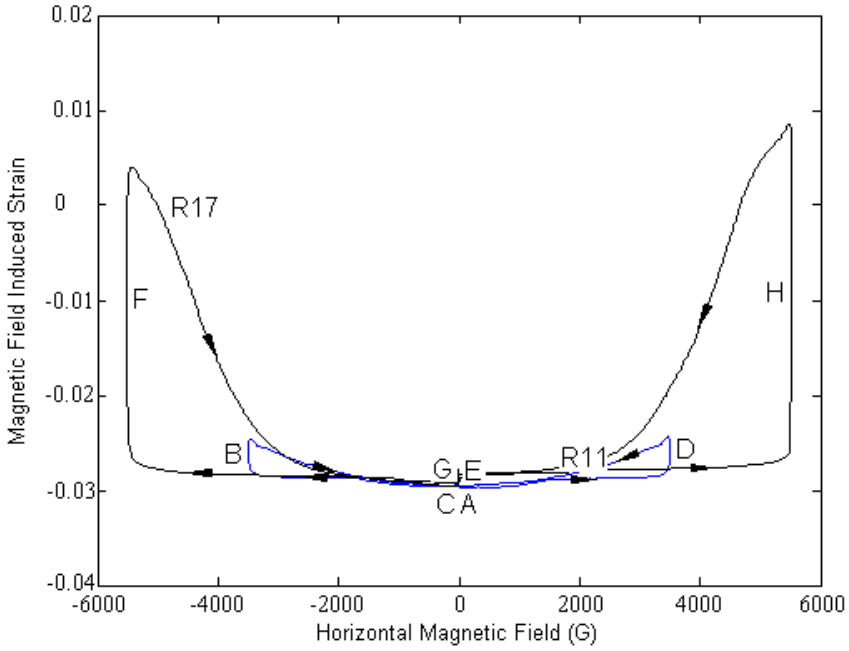

Figure 5.11: The result of magnetic field induced strain vs. horizontal magnetic field in the circular field part of test MFIS1 is shown here. The blue curve shows the MFIS path of 3690 G horizontal circular field under 0.5 MPa compression, and the black curve shows the that of 5500 G horizontal circular field under 0.5 MPa compression. The capital letter marked points are the same ones in Figure 5.9. The R11 curve starts from point A and R17 curve starts from point E.

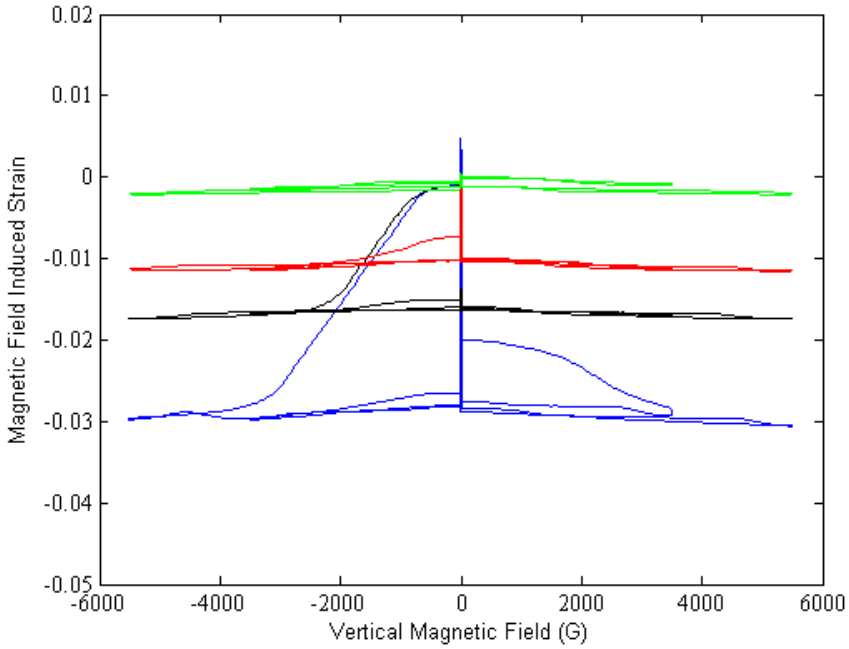

Figure 5.12: Results of MFISs vs. vertical linear magnetic field under different compressions are shown in the figure. Here, the blue curve indicates the result of 0.5 MPa compression from linear field part of test MFIS1, the black one is that of 1 MPa from linear field part of MFIS2, the red one is that of 1.5 MPa from linear field part of MFIS3 and the green one is that of 3 MPa from linear field part of test MFIS4.

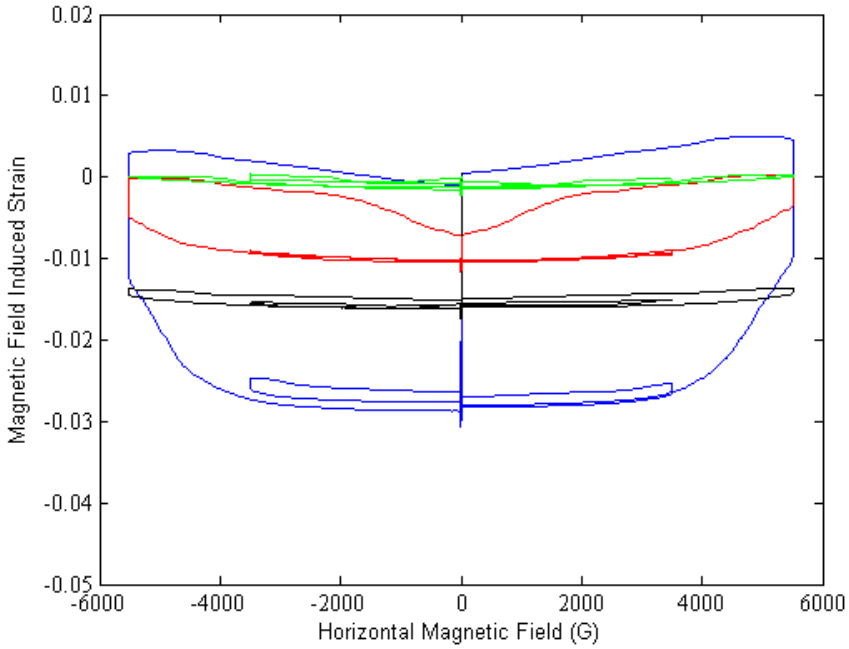

Figure 5.13: Results of MFISs vs. horizontal linear magnetic field under different compressions are shown in the figure. Here, the blue curve indicates the result of 0.5 MPa compression from linear field part of test MFIS1, the black one is that of 1 MPa from linear field part of MFIS2, the red one is that of 1.5 MPa from linear field part of MFIS3 and the green one is that of 3 MPa from linear field part of test MFIS4.

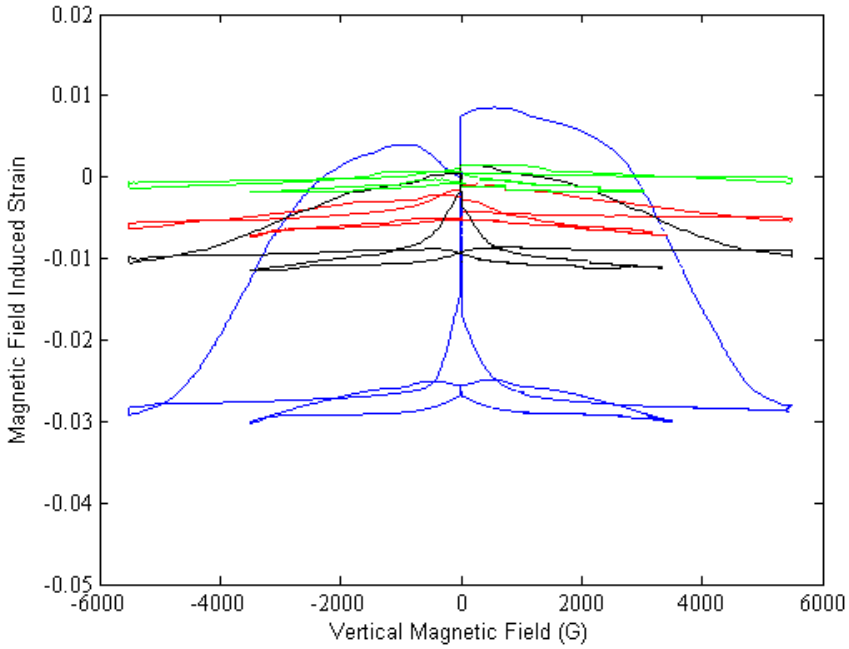

Figure 5.14: Results of MFISs vs. vertical component of circular field under different compressions are shown in the figure. Here, the blue curve indicates the result of 0.5 MPa compression from circular field part of test MFIS1, the black one is that of 1 MPa from circular field part of MFIS2, the red one is that of 1.5 MPa from circular field part of MFIS3 and the green one is that of 3 MPa from circular field part of test MFIS4.

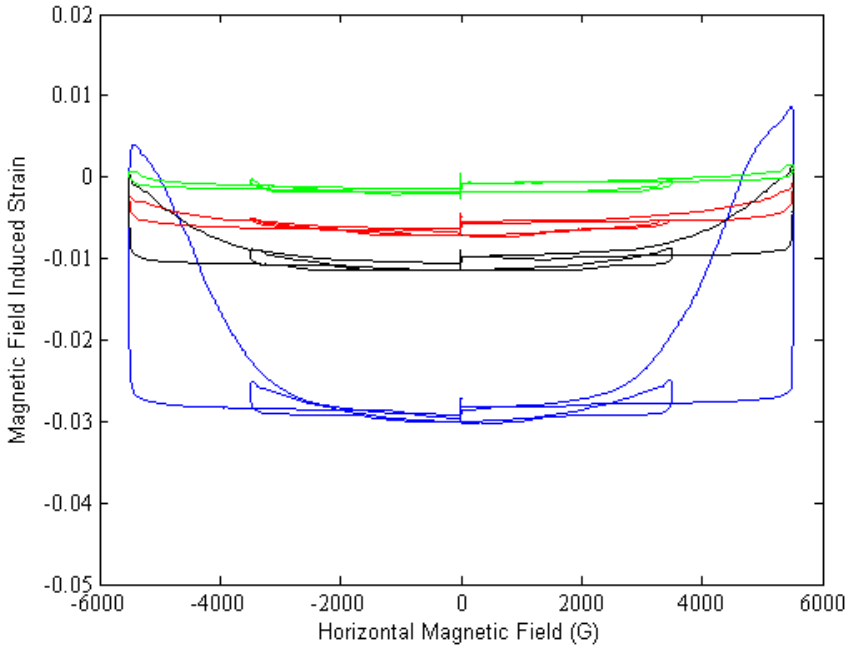

Figure 5.15: Results of MFISs vs. horizontal component of circular field under different compressions are shown in the figure. Here, the blue curve indicates the result of 0.5 MPa compression from circular field part of test MFIS1, the black one is that of 1 MPa from circular field part of MFIS2, the red one is that of 1.5 MPa from circular field part of MFIS3 and the green one is that of 3 MPa from circular field part of test MFIS4.

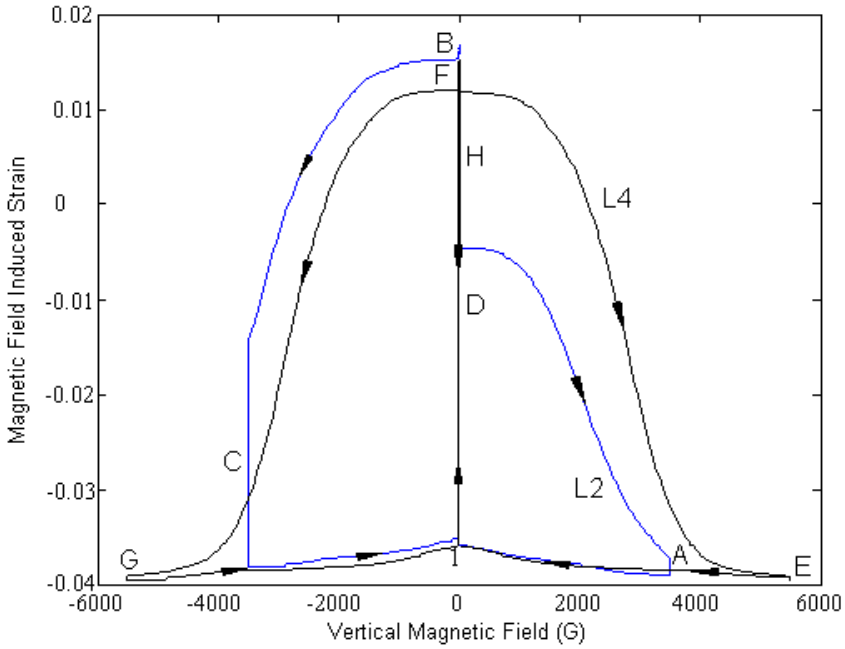

Figure 5.16: The result of magnetic field induced strain vs. vertical magnetic field in the linear field part of test MFIS6 is shown here. The blue curve shows the MFIS path of 3690 G initial vertical linear field under 0.5 MPa tension, and the black curve shows the that of 5500 G initial vertical linear field under 0.5 MPa tension. The letters correspond to the ones in Figure 5.4. Both curves L2 and L4 start from point 1.

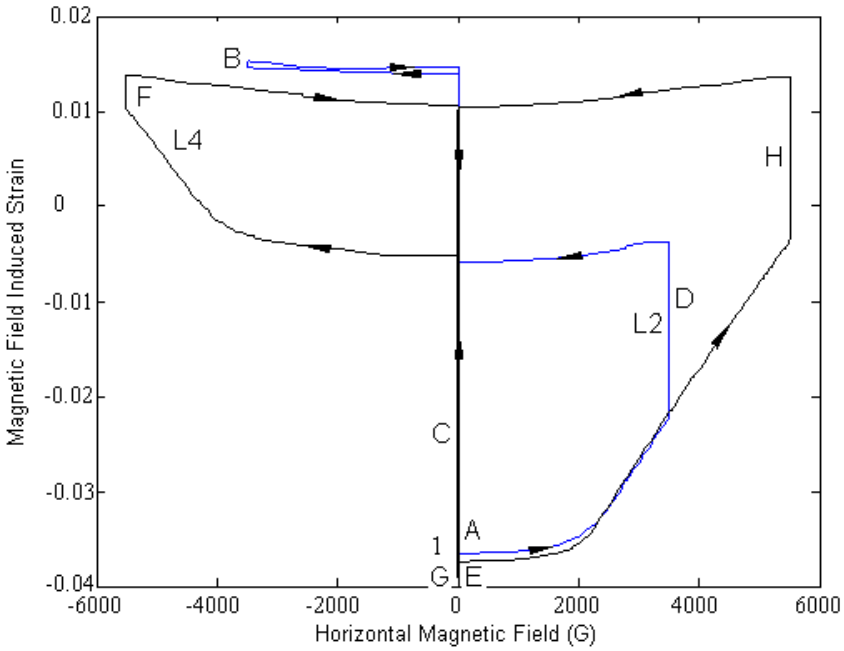

Figure 5.17: The result of magnetic field induced strain vs. horizontal magnetic field in the linear field part of test MFIS6 is shown here. The blue curve shows the MFIS path of 3690 G initial horizontal linear field under 0.5 MPa tension, and the black curve shows the that of 5500 G initial horizontal linear field under 0.5 MPa tension. The letters correspond to the ones in Figure 5.4. Both curves L2 and L4 start from point 1.

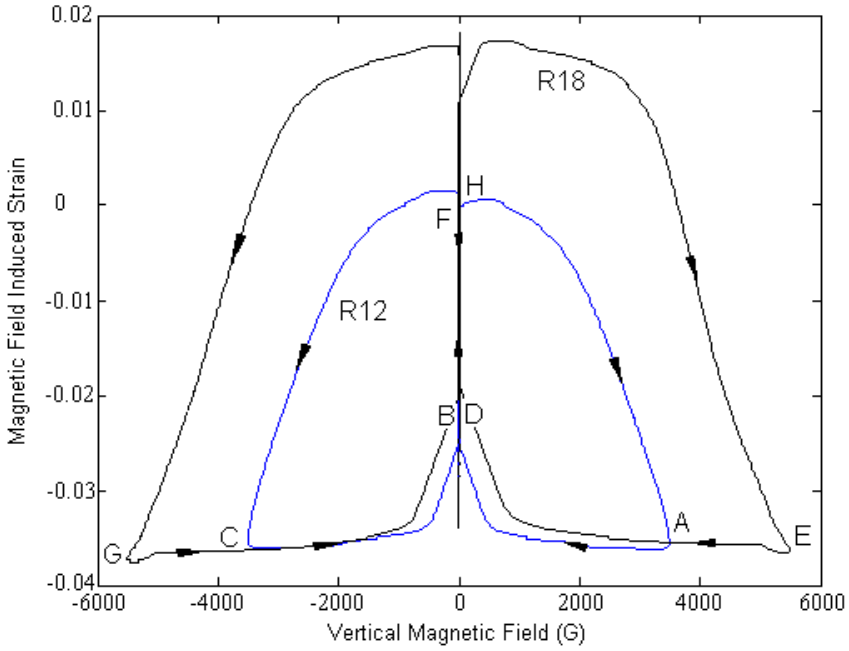

Figure 5.18: The result of magnetic field induced strain vs. vertical magnetic field in the circular field part of test MFIS6 is shown here. The blue curve shows the MFIS path of 3690 G vertical circular field under 0.5 MPa tension, and the black curve shows the that of 5500 G vertical circular field under 0.5 MPa tension. The letters correspond to the ones in Figure 5.9. The curve R12 starts from point D, and curve R18 starts from point H.

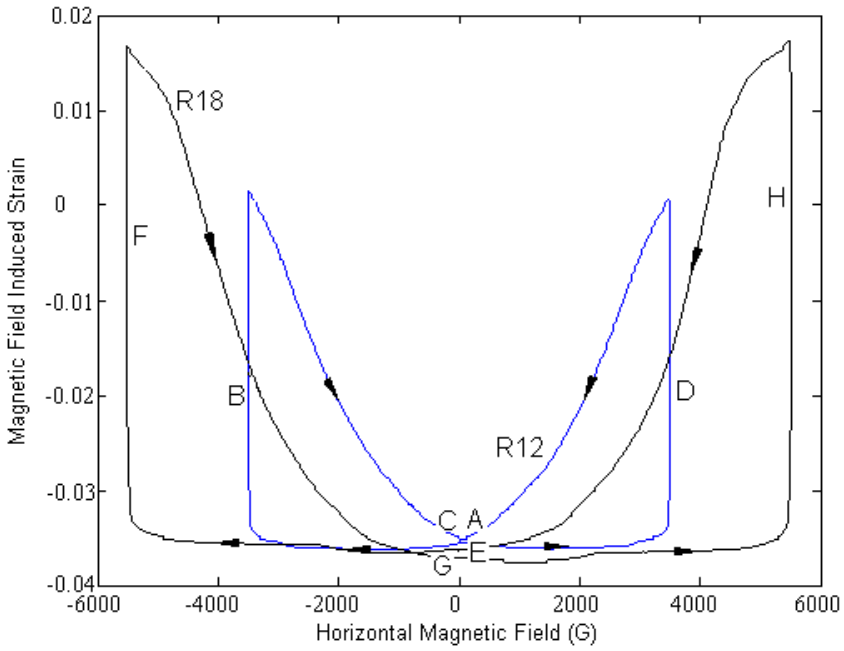

Figure 5.19: The result of magnetic field induced strain vs. horizontal magnetic field in the circular field part of test MFIS6 is shown here. The blue curve shows the MFIS path of 3690 G horizontal circular field under 0.5 MPa tension, and the black curve shows the that of 5500 G horizontal circular field under 0.5 MPa tension. The letters correspond to the ones in Figure 5.9. The curve R12 starts from point D, and curve R18 starts from point H.

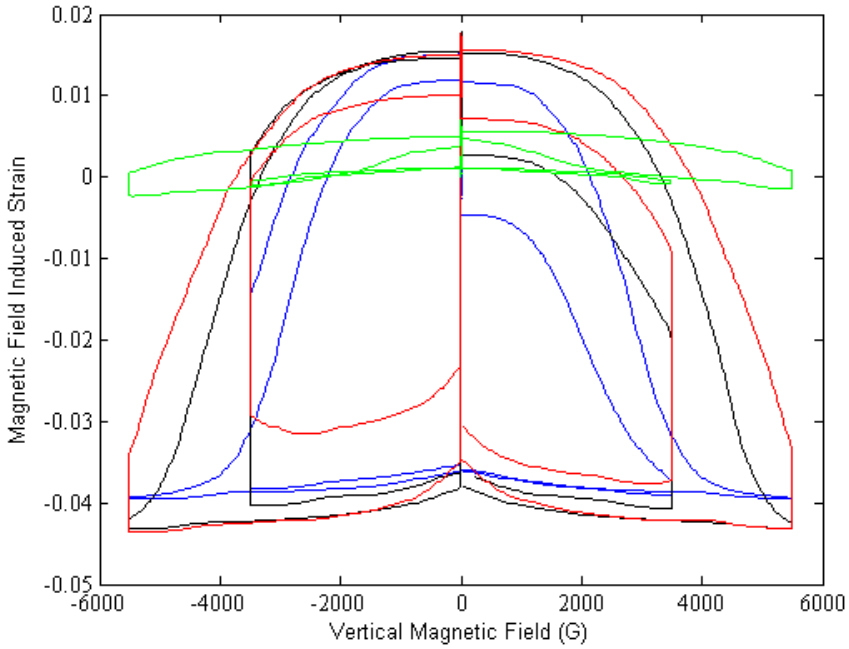

Figure 5.20: Results of MFISs vs. vertical linear magnetic field under different tensions are shown in the figure. Here, the blue curve indicates the result of 0.5 MPa tension from linear field part of test MFIS6, the black one is that of 1 MPa from linear field part of MFIS7, the red one is that of 1.5 MPa from linear field part of MFIS8 and the green one is that of 3 MPa from linear field part of test MFIS9.

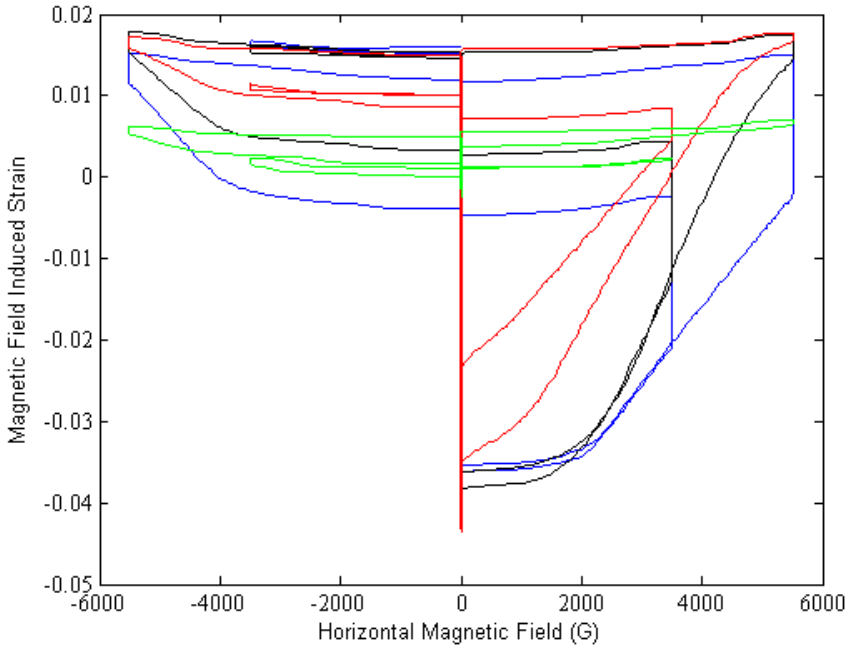

Figure 5.21: Results of MFISs vs. horizontal linear magnetic field under different tensions are shown in the figure. Here, the blue curve indicates the result of 0.5 MPa tension from linear field part of test MFIS6, the black one is that of 1 MPa from linear field part of MFIS7, the red one is that of 1.5 MPa from linear field part of MFIS8 and the green one is that of 3 MPa from linear field part of test MFIS9.

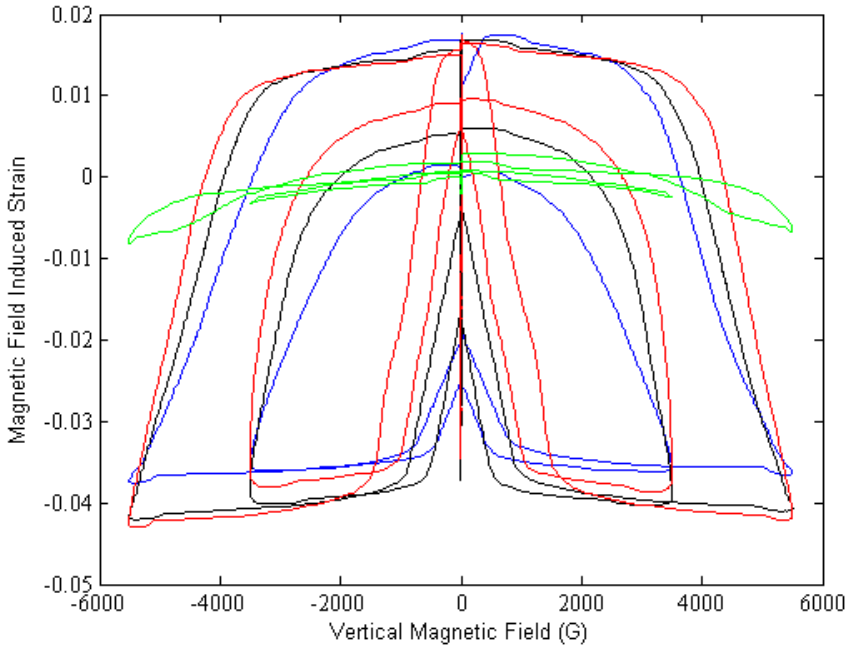

Figure 5.22: Results of MFISs vs. vertical component of rotary field under different tensions are shown in the figure. Here, the blue curve indicates the result of 0.5 MPa tension from rotary field part of test MFIS6, the black one is that of 1 MPa from rotary field part of MFIS7, the red one is that of 1.5 MPa from rotary field part of MFIS8 and the green one is that of 3 MPa from rotary field part of test MFIS9.

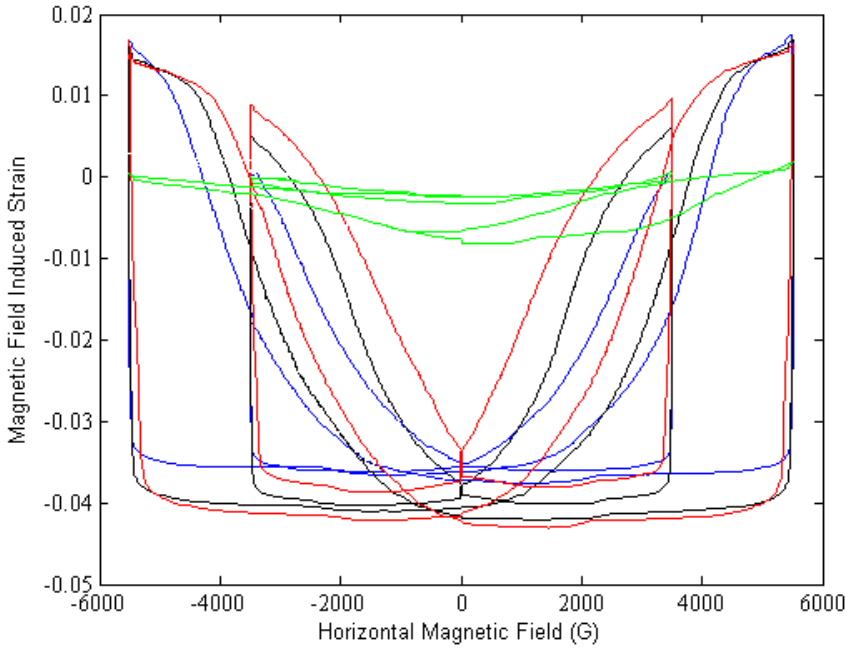

Figure 5.23: Results of MFISs vs. horizontal component of rotary field under different tensions are shown in the figure. Here, the blue curve indicates the result of 0.5 MPa tension from rotary field part of test MFIS6, the black one is that of 1 MPa from rotary field part of MFIS7, the red one is that of 1.5 MPa from rotary field part of MFIS8 and the green one is that of 3 MPa from rotary field part of test MFIS9.

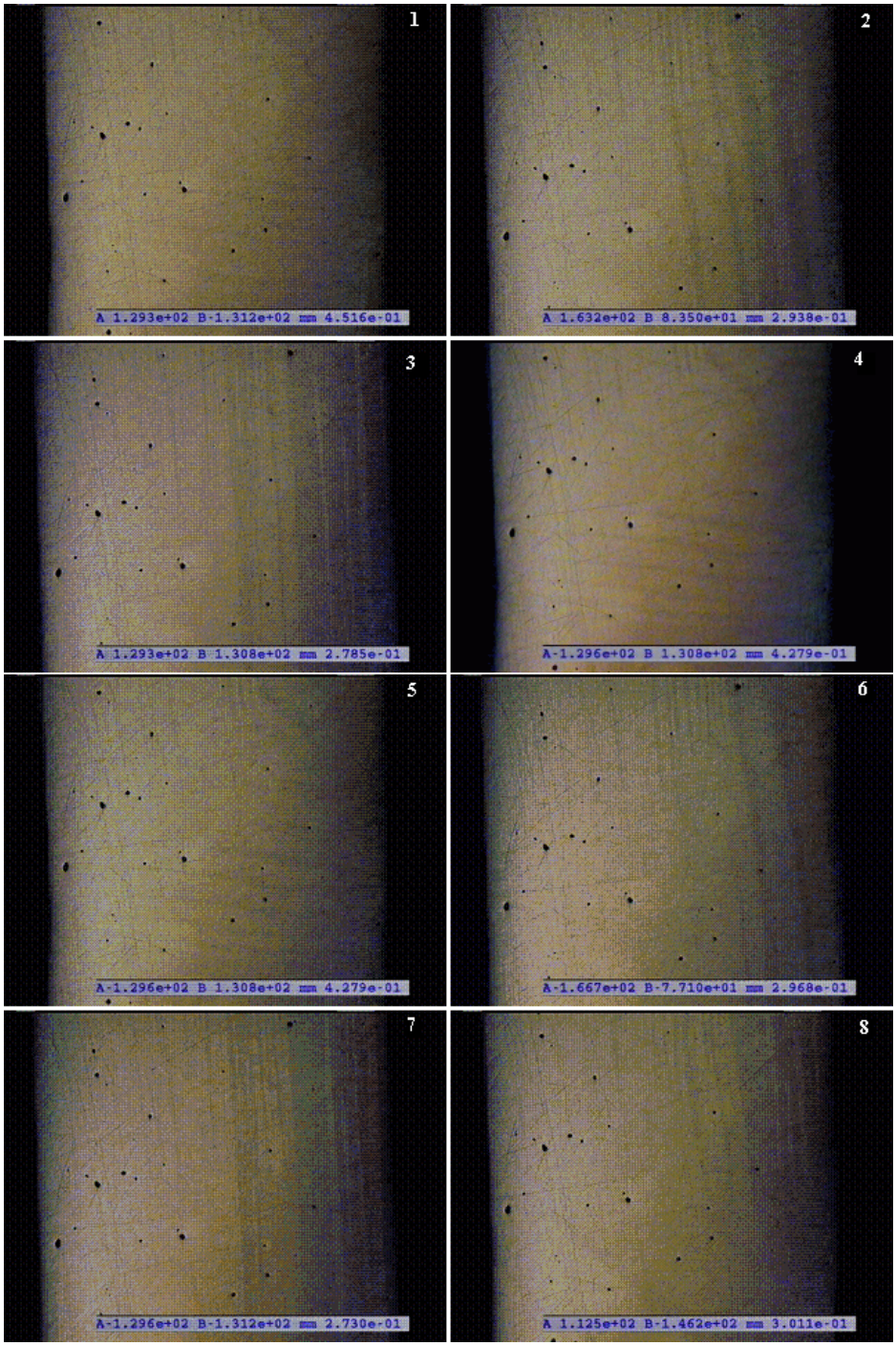

Figure 5.24: Microstructure change of Ni_2MnGa sample surface under applied circular magnetic field R18 and 0.5 MPa tension of test MFIS6 is shown in the images, and the directions of applied field in images 1 and 5 are horizontal right and left, which are at points H and F in Figures 5.18 and 5.19. In images 3 and 7 are vertical up and down, which are at points G and E in Figures 5.18 and 5.19. And in images 2, 4, 6 and 8 are between horizontal and vertical directions.

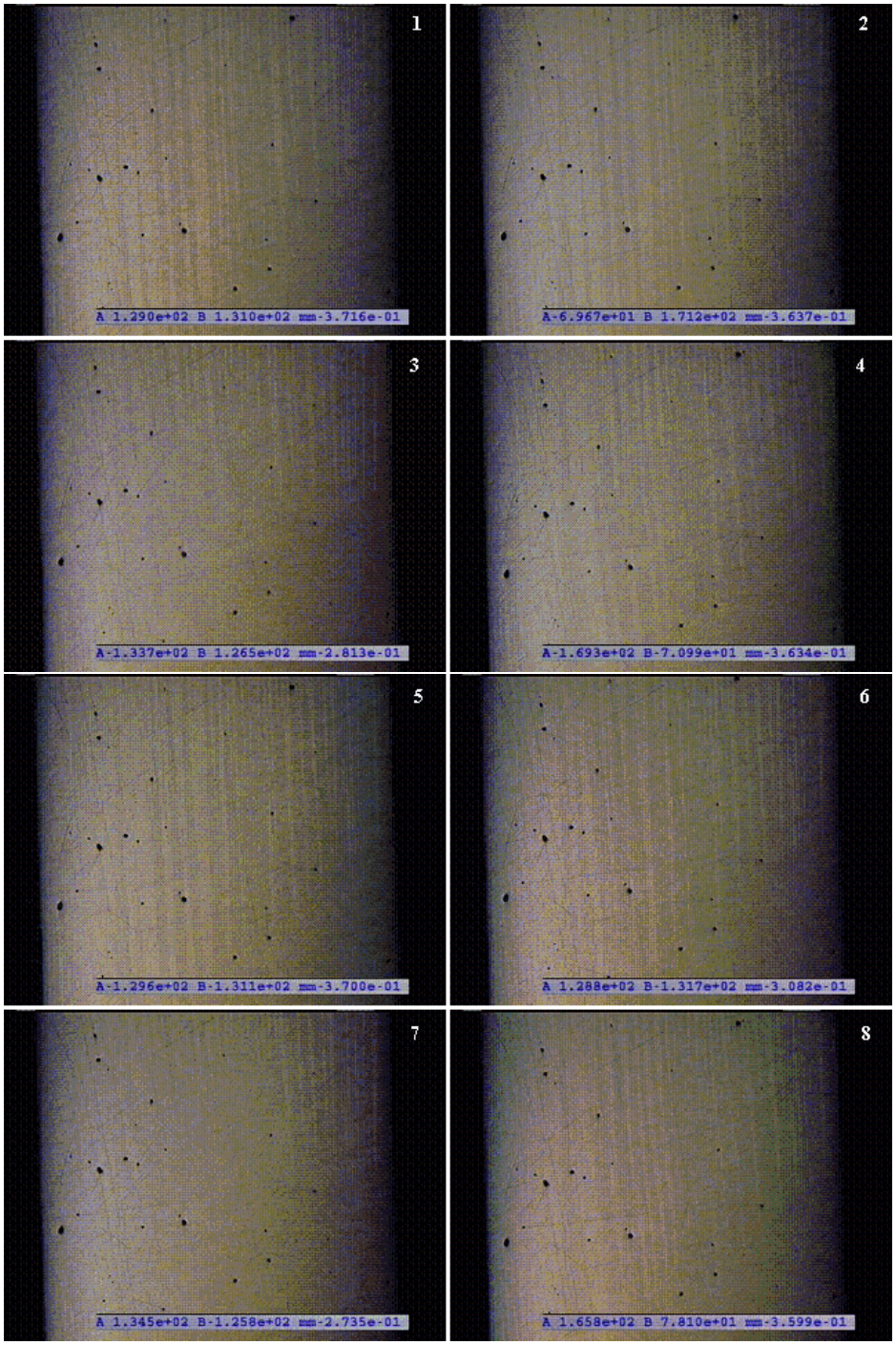

Figure 5.25: Microstructure change of Ni_2MnGa sample surface under applied circular magnetic field R17 and 0.5 MPa compression of test MFIS1 is shown in the images, and the directions of applied field in images 1 and 5 are vertical up and down, which are at points E and G in Figures 5.11 and 5.12. In images 3 and 7 are horizontal left and right, which are at points F and H in Figures 5.11 and 5.12. And in images 2, 4, 6 and 8 are between vertical and horizontal directions.

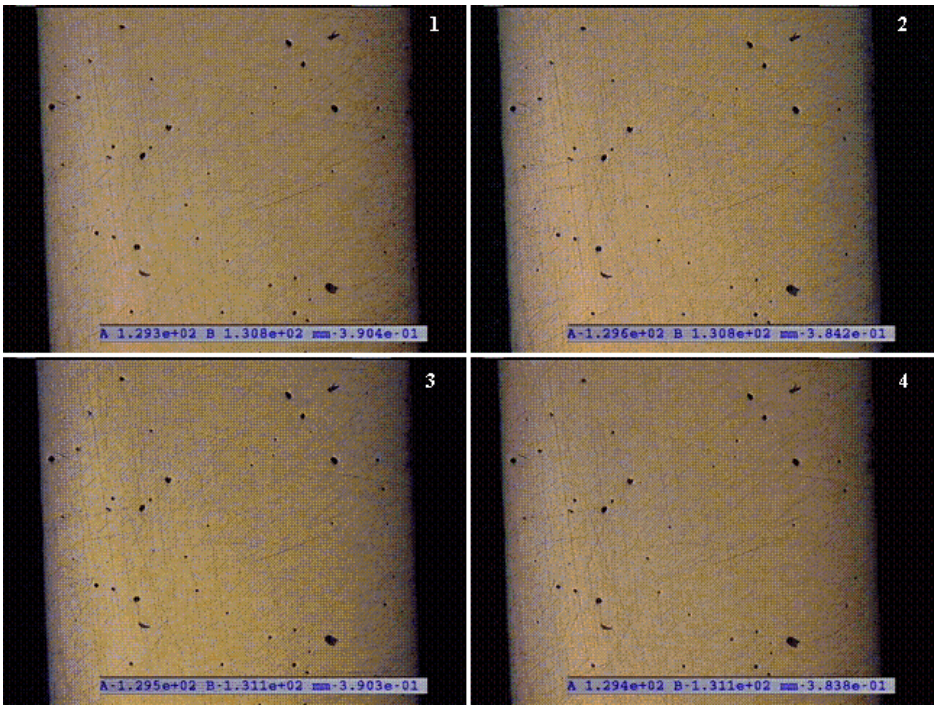

Figure 5.26: Microstructure change of Ni_2MnGa sample surface under applied circular magnetic field R17 and 3 MPa compression of test MFIS4 is shown in the images, and the directions of applied field in images 1 and 3 are vertical up and down, in image 2 and 4 are horizontal left and right.

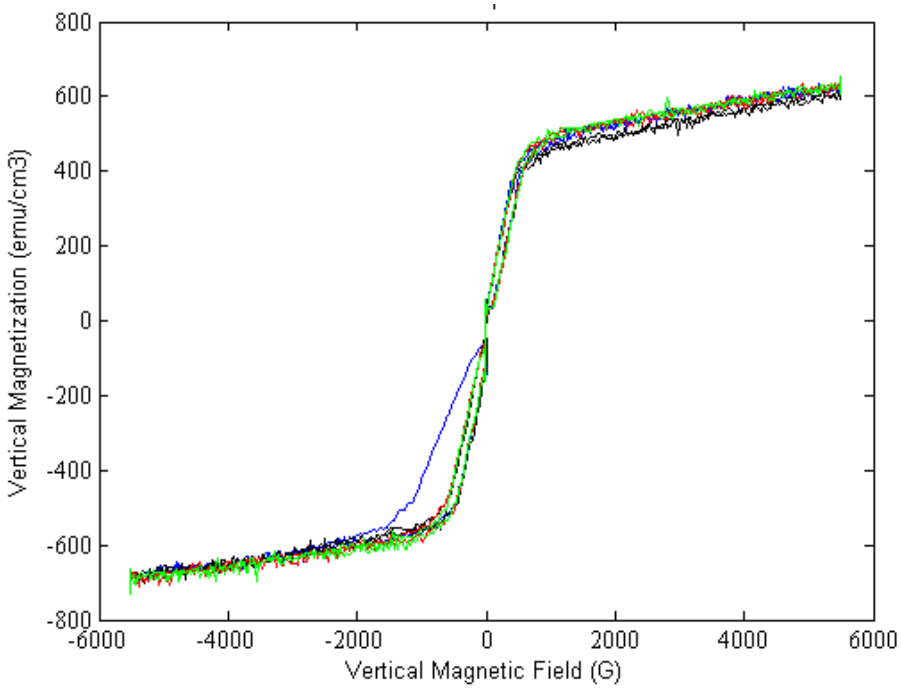

Figure 5.27: Results of vertical magnetization of the sample vs. vertical component of the applied field for the linear L3 pattern of the field path under different compressions are shown in the figure. Here, the blue curve indicates the result of 0.5 MPa compression of test MFIS1, the black one is that of 1 MPa of test MFIS2, the red one is that of 1.5 MPa of test MFIS3 and the green one is that of 3 MPa of test MFIS4.

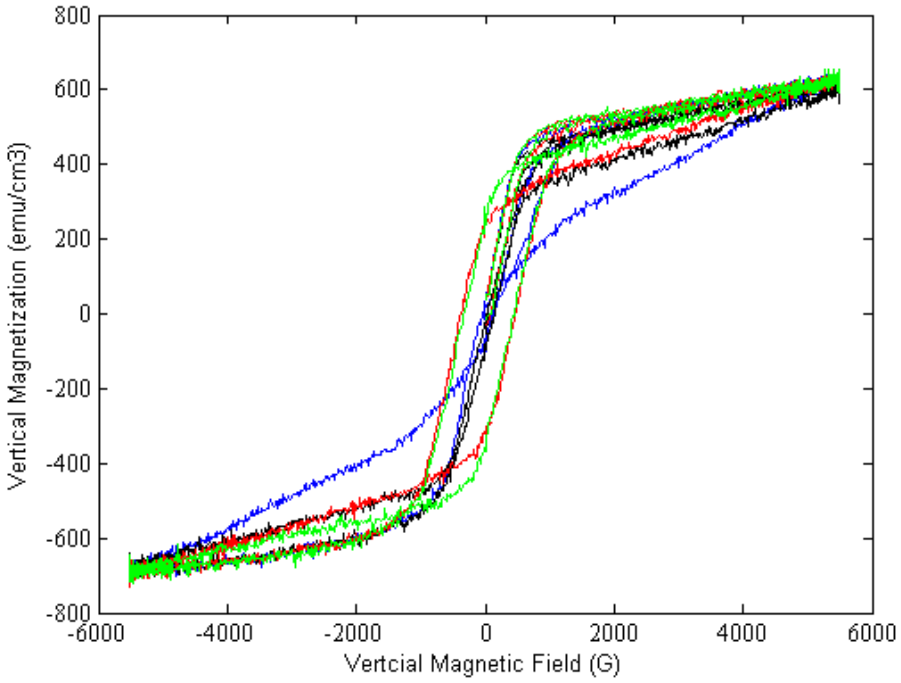

Figure 5.28: Results of vertical magnetization of the sample vs. vertical component of the applied field for the circular R17 pattern of the field path under different compressions are shown in the figure. Here, the blue curve indicates the result of 0.5 MPa compression of test MFIS1, the black one is that of 1 MPa of test MFIS2, the red one is that of 1.5 MPa of test MFIS3 and the green one is that of 3 MPa of test MFIS4.

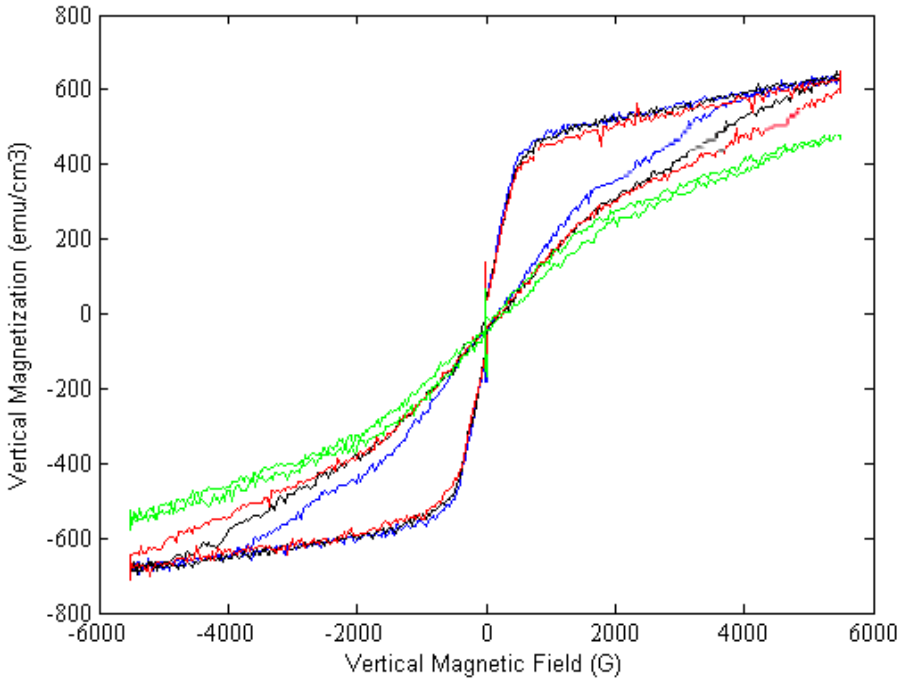

Figure 5.29: Results of vertical magnetization of the sample vs. vertical component of the applied field for the linear L4 pattern of the field path under different tensions are shown in the figure. Here, the blue curve indicates the result of 0.5 MPa tension of test MFIS6, the black one is that of 1 MPa of MFIS7, the red one is that of 1.5 MPa of MFIS8 and the green one is that of 3 MPa of MFIS9.

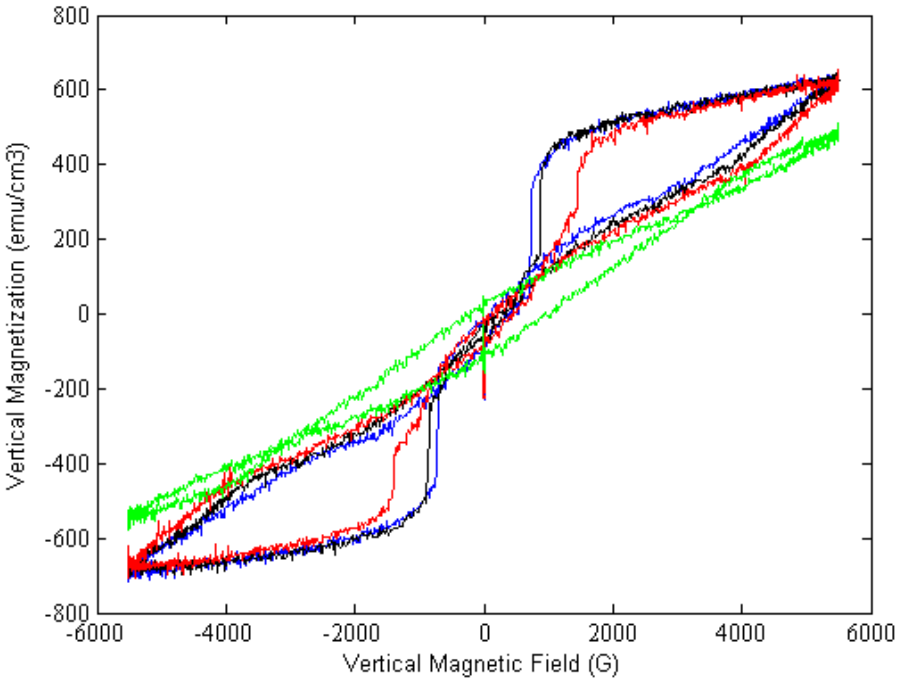

Figure 5.30: Results of vertical magnetization of the sample vs. vertical component of the applied field for the circular R18 pattern of the field path under different tensions are shown in the figure. Here, the blue curve indicates the result of 0.5 MPa tension of test MFIS6, the black one is that of 1 MPa of test MFIS7, the red one is that of 1.5 MPa of test MFIS8 and the green one is that of 3 MPa of MFIS9.

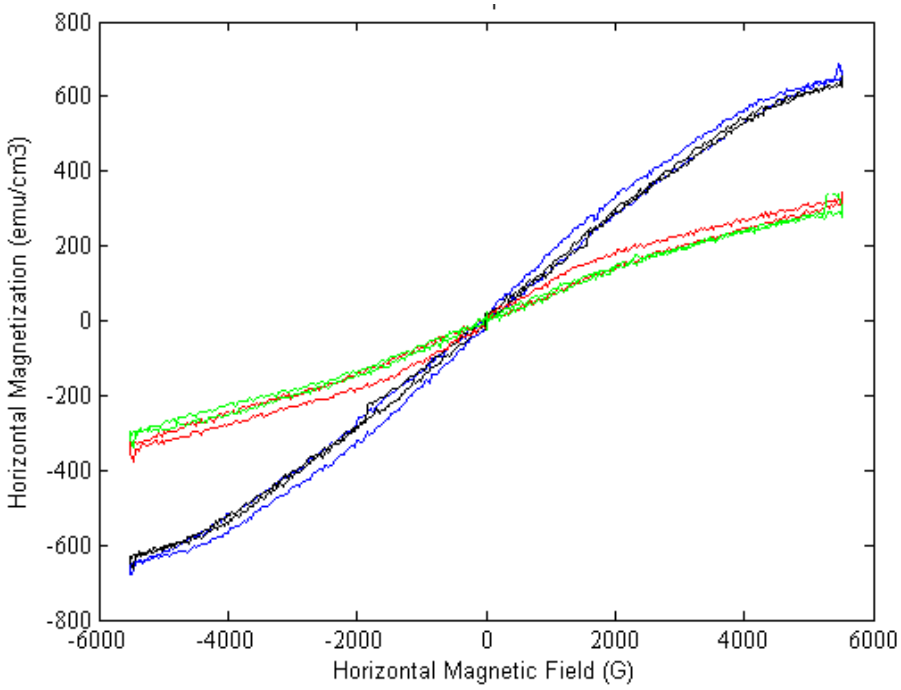

Figure 5.31: Results of horizontal magnetization of the sample vs. horizontal component of the applied field for the linear L3 pattern of the field path under different compressions are shown in the figure. Here, the blue curve indicates the result of 0.5 MPa compression of test MFIS1, the black one is that of 1 MPa of test MFIS2, the red one is that of 1.5 MPa of test MFIS3 and the green one is that of 3 MPa of test MFIS4.

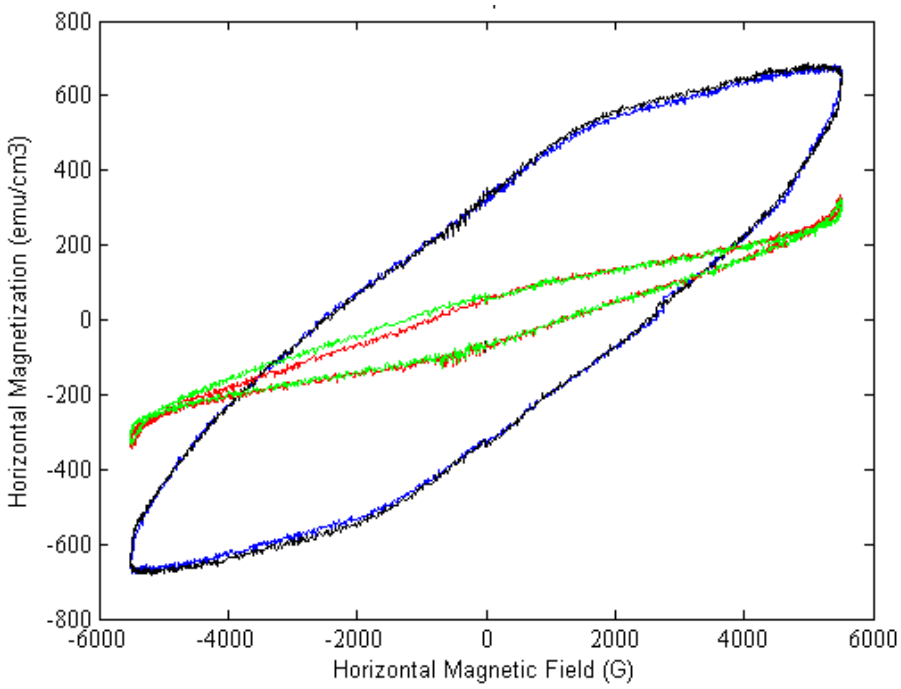

Figure 5.32: Results of horizontal magnetization of the sample vs. horizontal component of the applied field for the circular R17 pattern of the field path under different compressions are shown in the figure. Here, the blue curve indicates the result of 0.5 MPa compression of test MFIS1, the black one is that of 1 MPa of test MFIS2, the red one is that of 1.5 MPa of MFIS3 and the green one is that of 3 MPa of MFIS4.

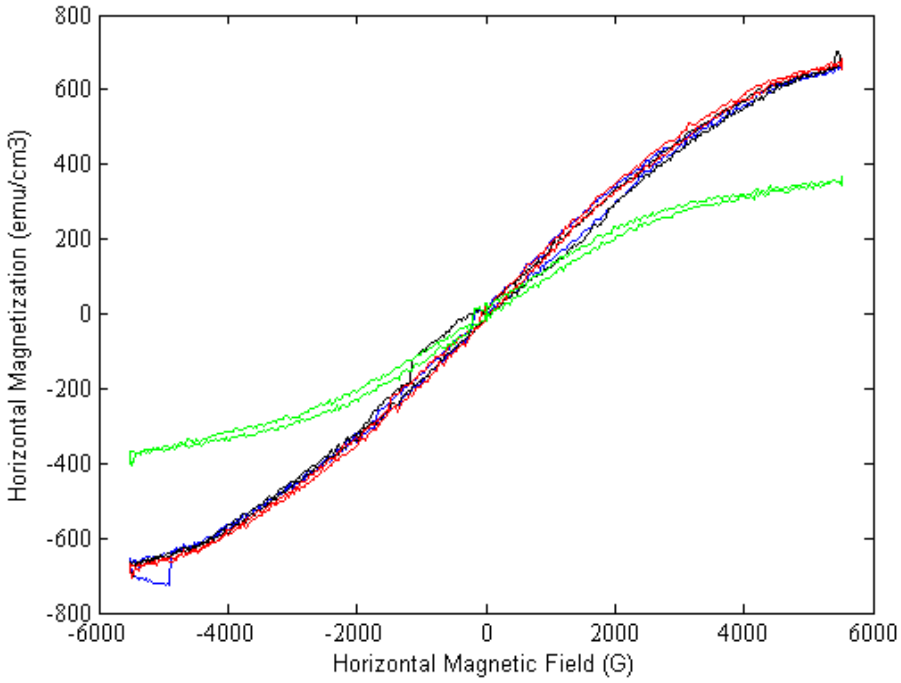

Figure 5.33: Results of horizontal magnetization of the sample vs. horizontal component of the applied field for the linear L4 pattern of the field path under different tensions are shown in the figure. Here, the blue curve indicates the result of 0.5 MPa tension of test MFIS6, the black one is that of 1 MPa of test MFIS7, the red one is that of 1.5 MPa of test MFIS8 and the green one is that of 3 MPa of test MFIS9.

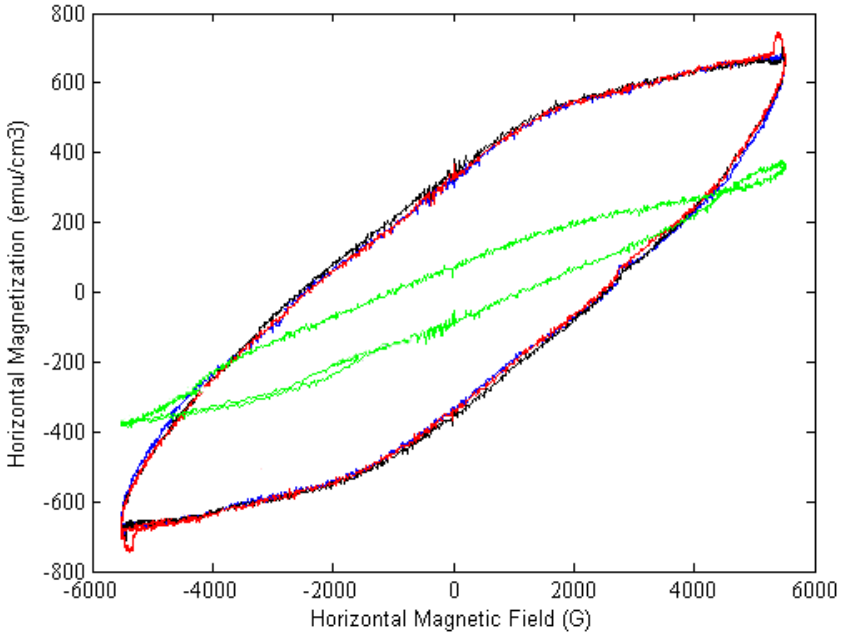

Figure 5.34: Results of horizontal magnetization of the sample vs. horizontal component of the applied field for the circular R18 pattern of the field path under different tensions are shown in the figure. Here, the blue curve indicates the result of 0.5 MPa tension of test MFIS6, the black one is that of 1 MPa of test MFIS7, the red one is that of 1.5 MPa of test MFIS8 and the green one is that of 3 MPa of test MFIS9.

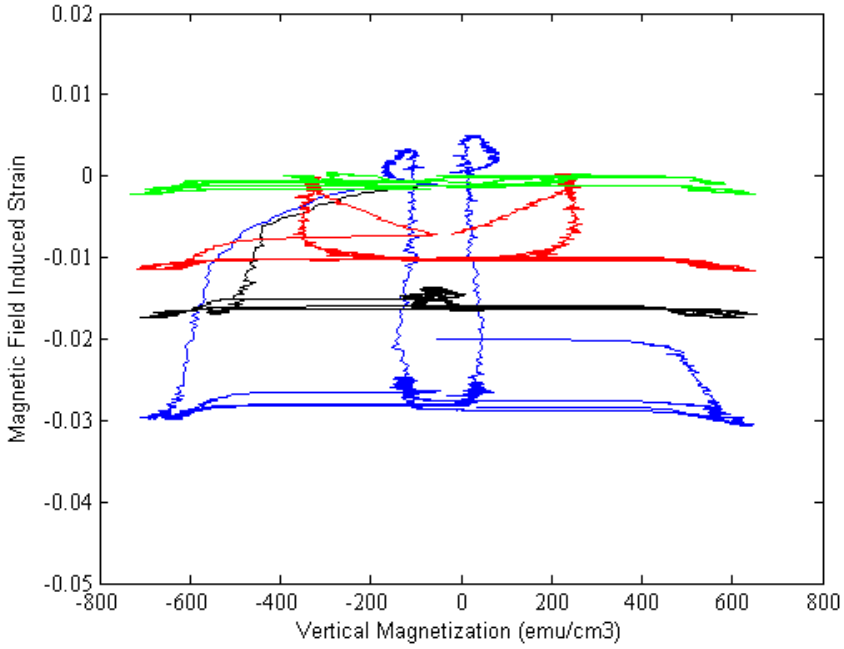

Figure 5.35: Results of MFISs vs. vertical magnetization under linear field path and different compressions are shown in the figure. Here, the blue curve indicates the result of 0.5 MPa compression of test MFIS1, the black one is that of 1 MPa of test MFIS2, the red one is that of 1.5 MPa of test MFIS3 and the green one is that of 3 MPa of test MFIS4.

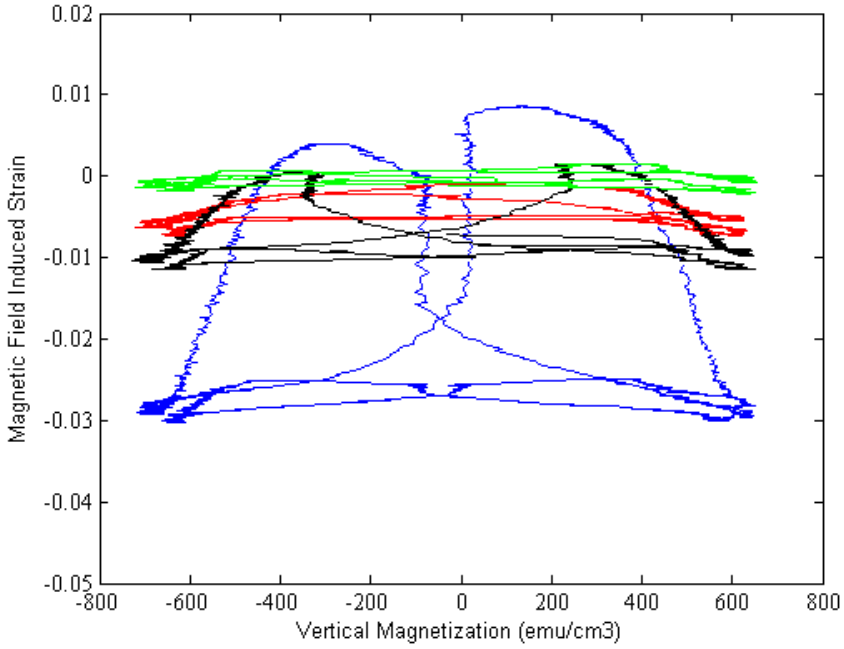

Figure 5.36: Results of MFISs vs. vertical magnetization under circular field path and different compressions are shown in the figure. Here, the blue curve indicates the result of 0.5 MPa compression of test MFIS1, the black one is that of 1 MPa of test MFIS2, the red one is that of 1.5 MPa of test MFIS3 and the green one is that of 3 MPa of test MFIS4.

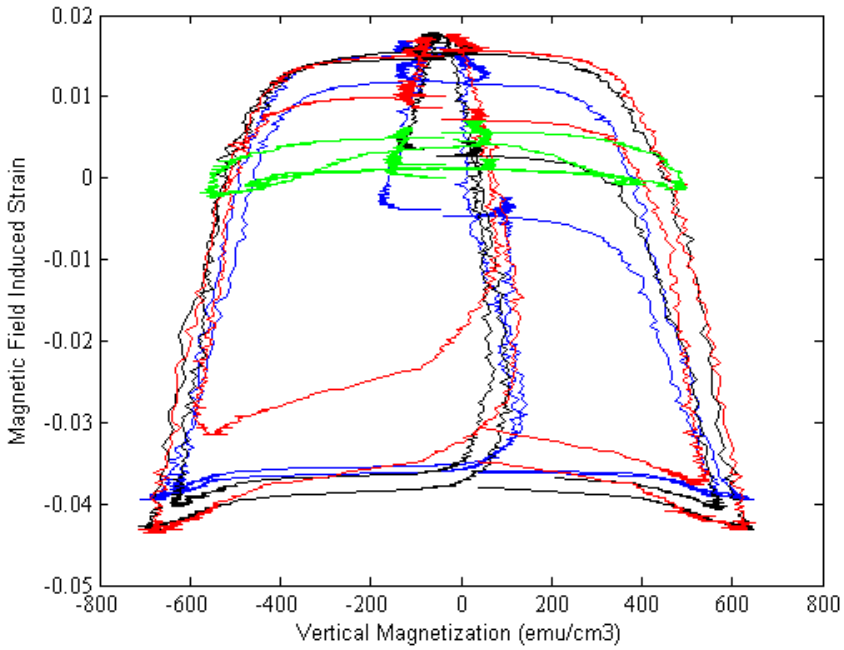

Figure 5.37: Results of MFISs vs. vertical magnetization under linear field path and different tensions are shown in the figure. Here, the blue curve indicates the result of 0.5 MPa tension of test MFIS6, the black one is that of 1 MPa of test MFIS7, the red one is that of 1.5 MPa of test MFIS8 and the green one is that of 3 MPa of test MFIS9.

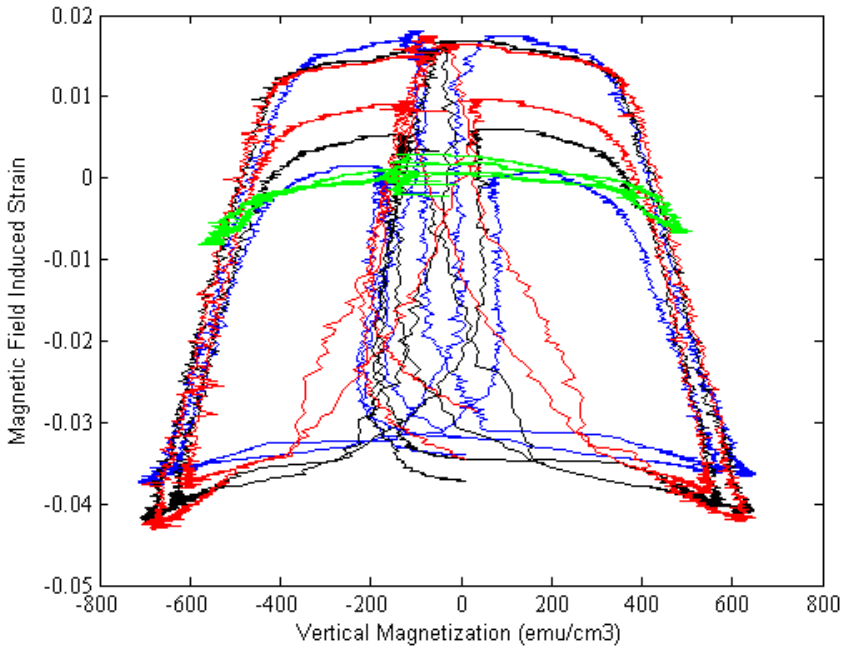

Figure 5.38: Results of MFISs vs. vertical magnetization under circular field path and different tensions are shown in the figure. Here, the blue curve indicates the result of 0.5 MPa tension of test MFIS6, the black one is that of 1 MPa of test MFIS7, the red one is that of 1.5 MPa of test MFIS8 and the green one is that of 3 MPa of test MFIS9.

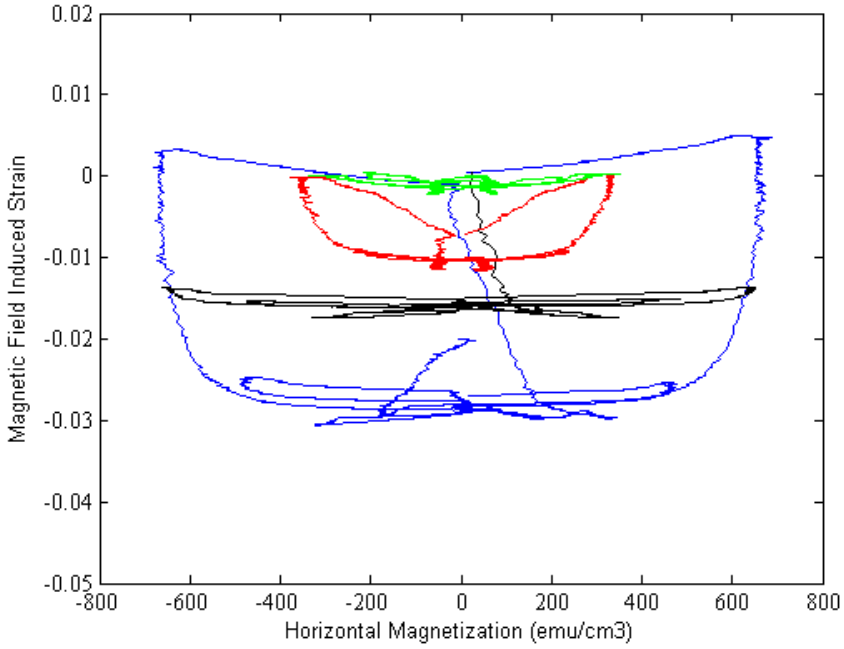

Figure 5.39: Results of MFISs vs. horizontal magnetization under linear field path and different compressions are shown in the figure. Here, the blue curve indicates the result of 0.5 MPa compression of test MFIS1, the black one is that of 1 MPa of test MFIS2, the red one is that of 1.5 MPa of test MFIS3 and the green one is that of 3 MPa of test MFIS4.

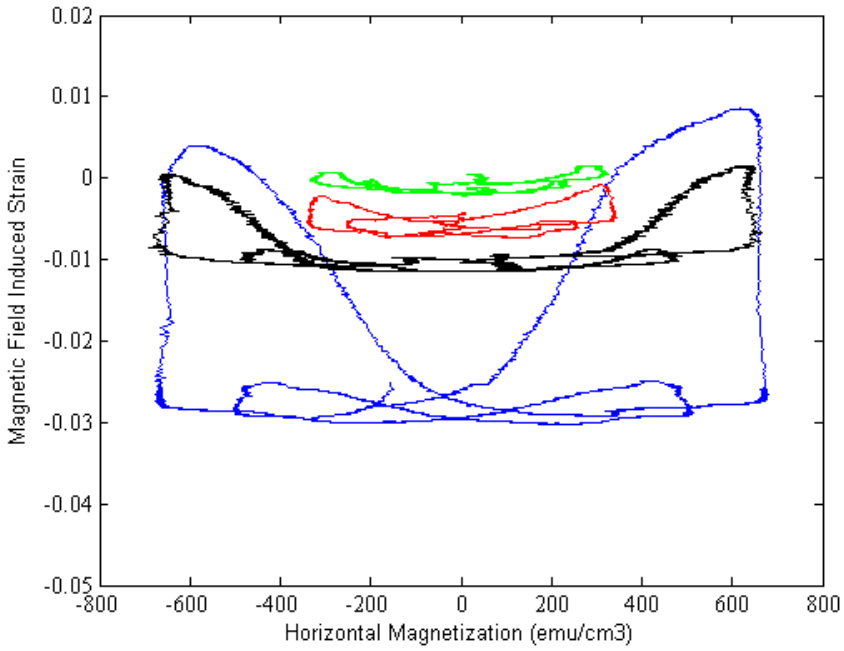

Figure 5.40: Results of MFISs vs. horizontal magnetization under circular field path and different compressions are shown in the figure. Here, the blue curve indicates the result of 0.5 MPa compression of test MFIS1, the black one is that of 1 MPa of test MFIS2, the red one is that of 1.5 MPa of test MFIS3 and the green one is that of 3 MPa of test MFIS4.

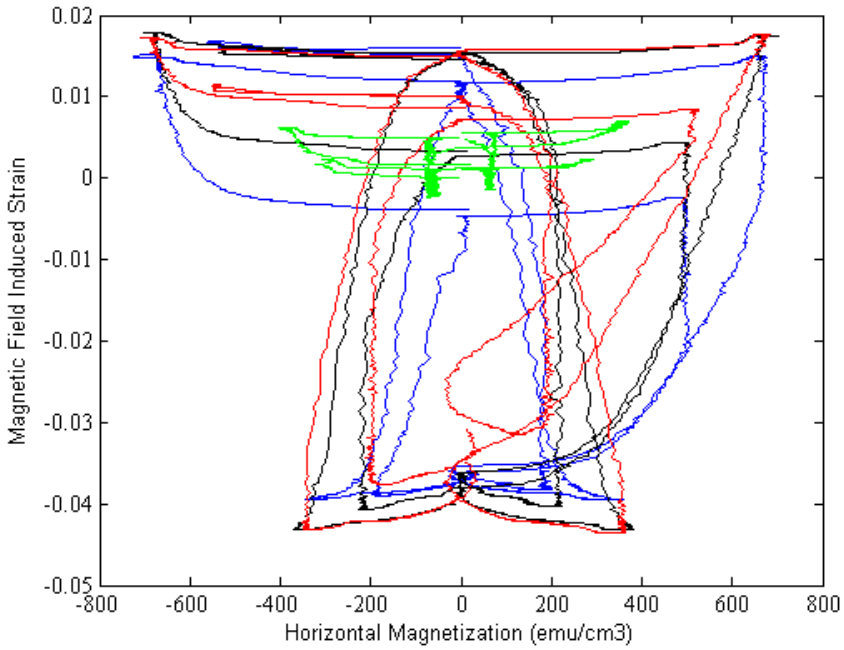

Figure 5.41: Results of MFISs vs. horizontal magnetization under linear field path and different tensions are shown in the figure. Here, the blue curve indicates the result of 0.5 MPa tension of test MFIS6, the black one is that of 1 MPa of test MFIS7, the red one is that of 1.5 MPa of test MFIS8 and the green one is that of 3 MPa of test MFIS9.

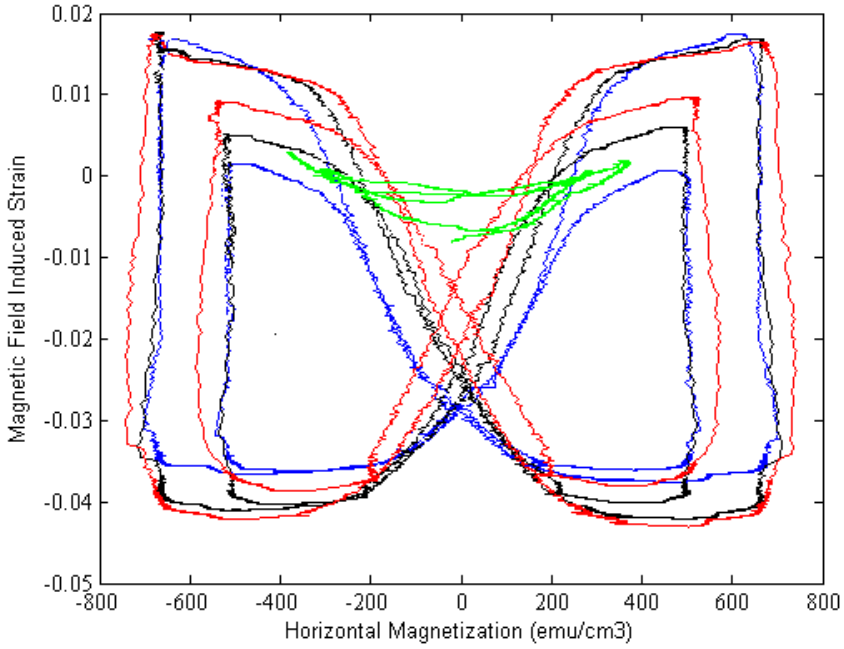

Figure 5.42: Results of MFISs vs. horizontal magnetization under circular field path and different tensions are shown in the figure. Here, the blue curve indicates the result of 0.5 MPa tension of test MFIS6, the black one is that of 1 MPa of test MFIS7, the red one is that of 1.5 MPa of test MFIS8 and the green one is that of 3 MPa of test MFIS9.

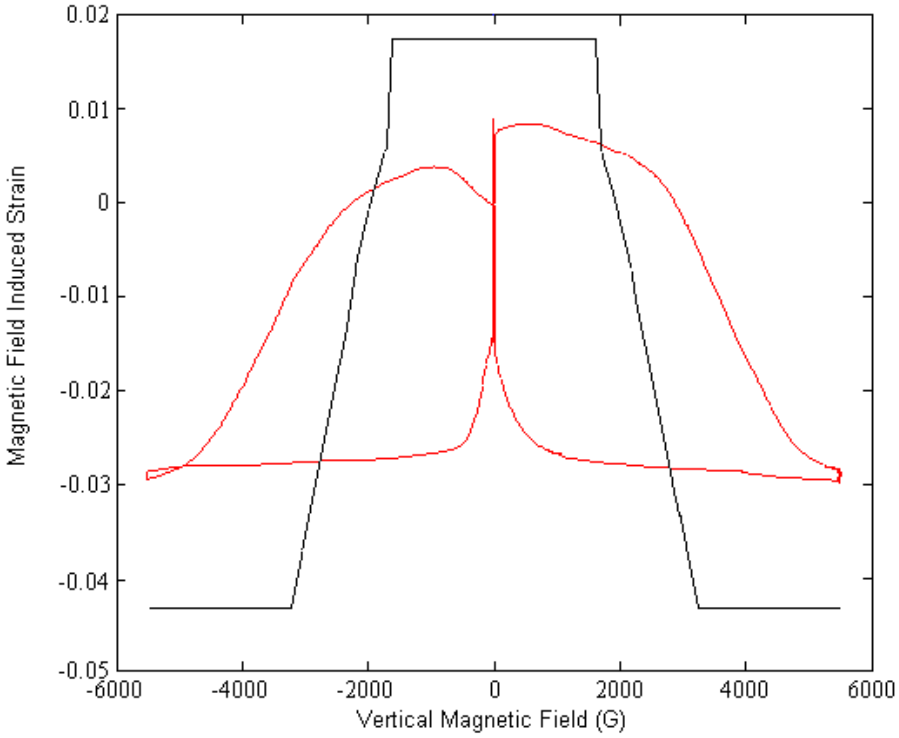

Figure 5.43: Comparison of the simple model calculation and the experimental result on MFIS vs. vertical component of circular field path R17 under 0.5 MPa compression is shown in the figure. Here, the black curve is the simple model calculation result and the red one is the experimental data.

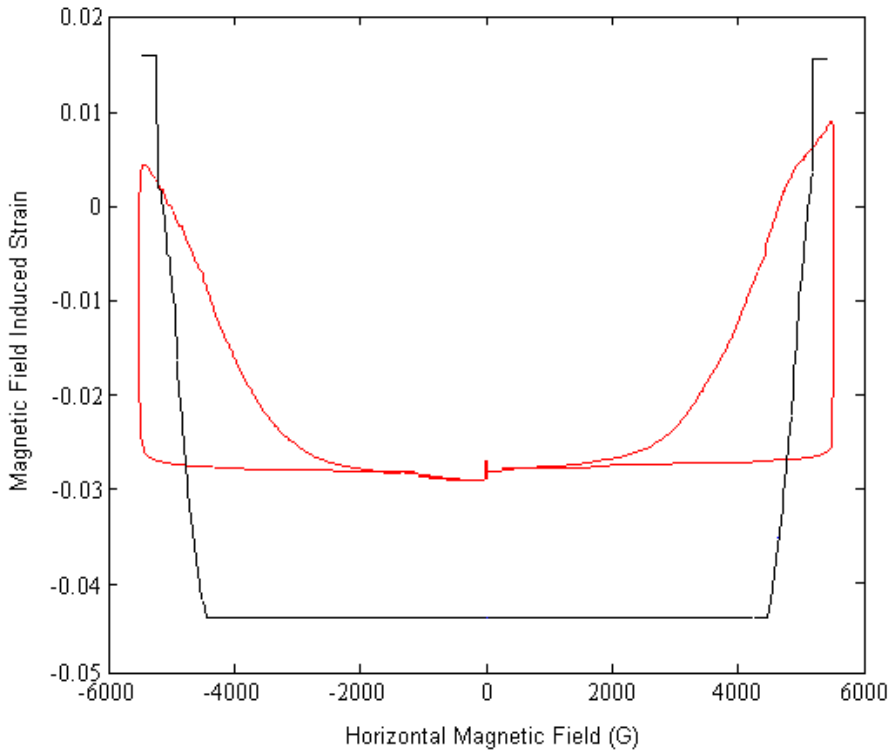

Figure 5.44: Comparison of the simple model calculation and the experimental result on MFIS vs. horizontal component of circular field path R17 under 0.5 MPa compression is shown in the figure. Here, the black curve is the simple model calculation result and the red one is the experimental data.

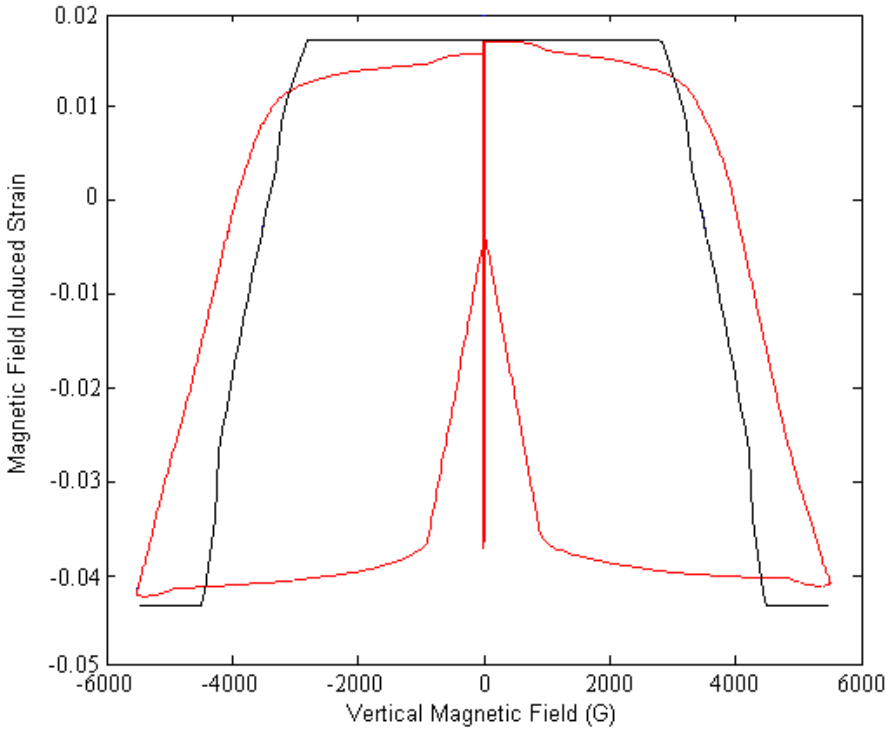

Figure 5.45: Comparison of the simple model calculation and the experimental result on MFIS vs. vertical component of circular field path R18 under 1 MPa tension is shown in the figure. Here, the black curve is the simple model calculation result and the red one is the experimental data.

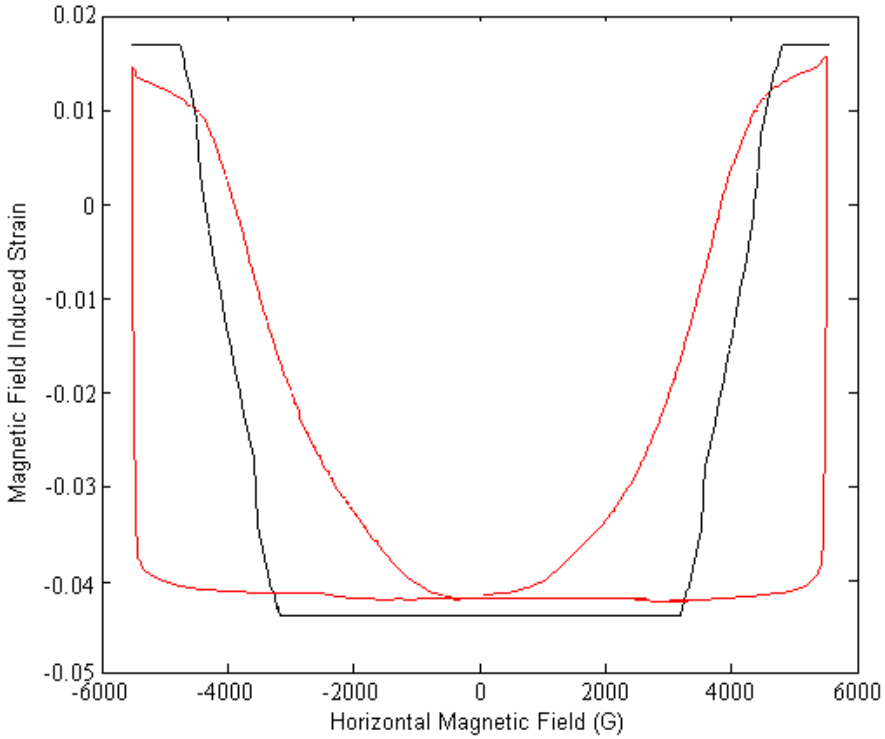

Figure 5.46: Comparison of the simple model calculation and the experimental result on MFIS vs. horizontal component of circular field path R18 under 1 MPa tension is shown in the figure. Here, the black curve is the simple model calculation result and the red one is the experimental data.

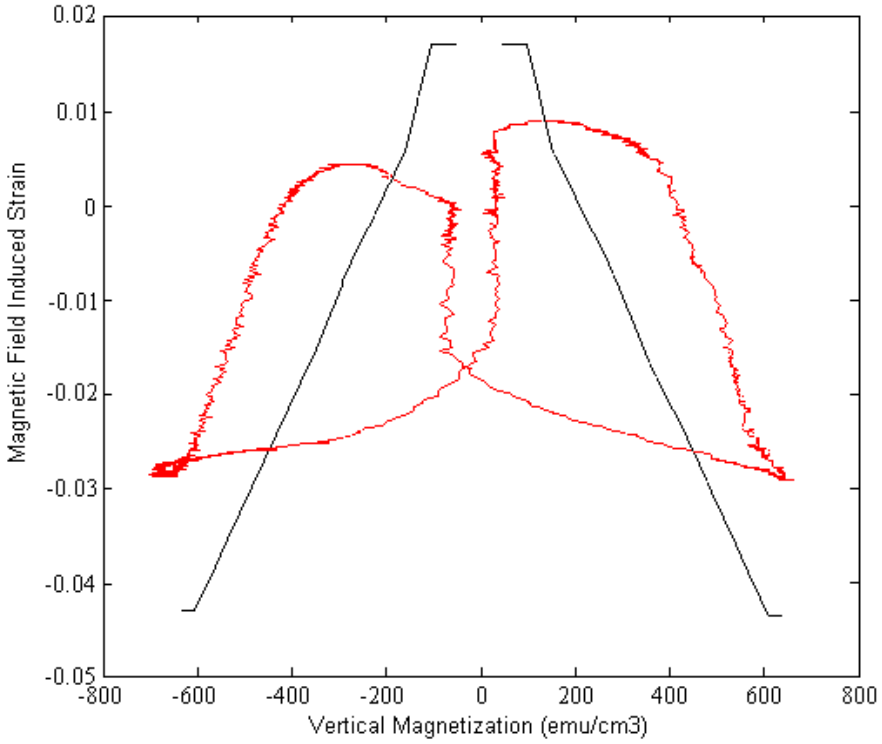

Figure 5.47: Comparison of the simple model calculation and the experimental result on MFIS vs. vertical magnetization of the sample under applied circular field path R17 and 0.5 MPa compression is shown in the figure. Here, the black curve is the simple model calculation result and the red one is the experimental data.

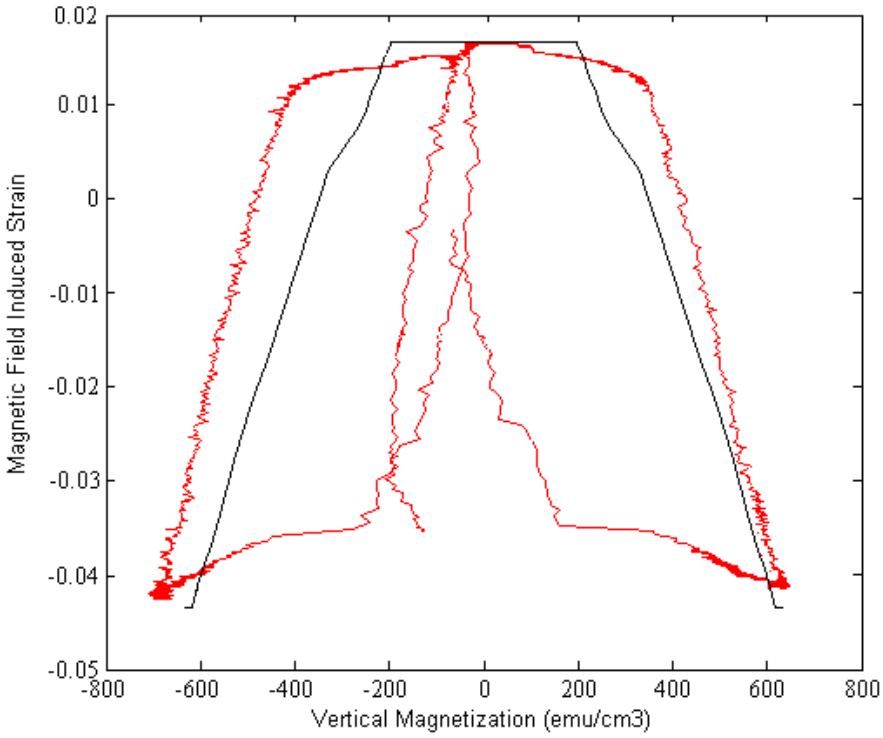

Figure 5.48: Comparison of the simple model calculation and the experimental result on MFIS vs. vertical magnetization of the sample under applied circular field path R18 and 1 MPa tension is shown in the figure. Here, the black curve is the simple model calculation result and the red one is the experimental data.

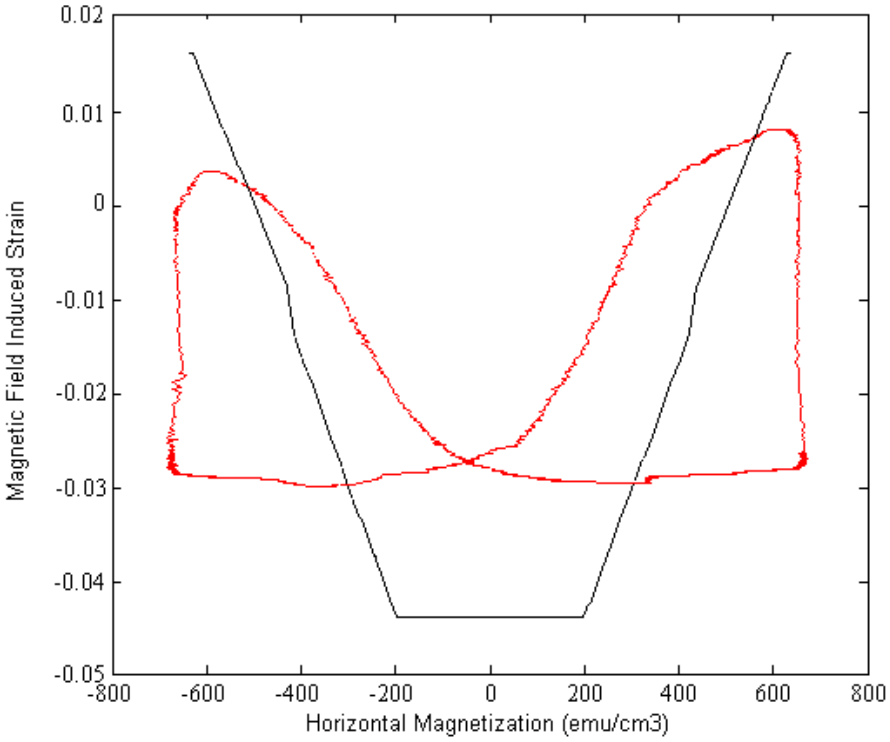

Figure 5.49: Comparison of the simple model calculation and the experimental result on MFIS vs. horizontal magnetization of the sample under applied circular field path R17 and 0.5 MPa compression is shown in the figure. Here, the black curve is the simple model calculation result and the red one is the experimental data.

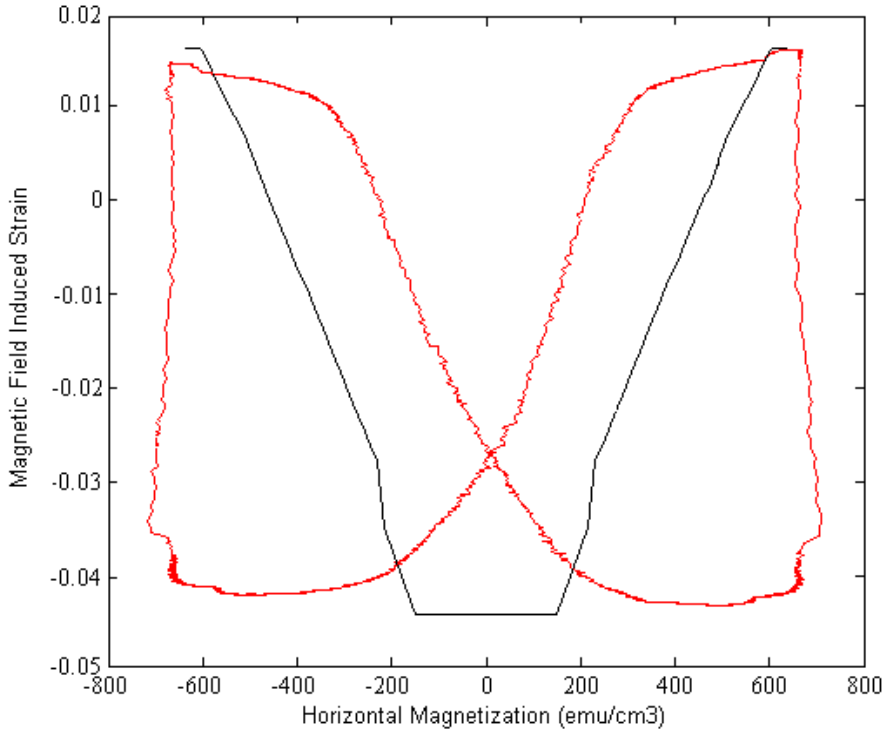

Figure 5.50: Comparison of the simple model calculation and the experimental result on MFIS vs. horizontal magnetization of the sample under applied circular field Path R18 and 1 MPa tension is shown in the figure. Here, the black curve is the simple model calculation result and the red one is the experimental data.

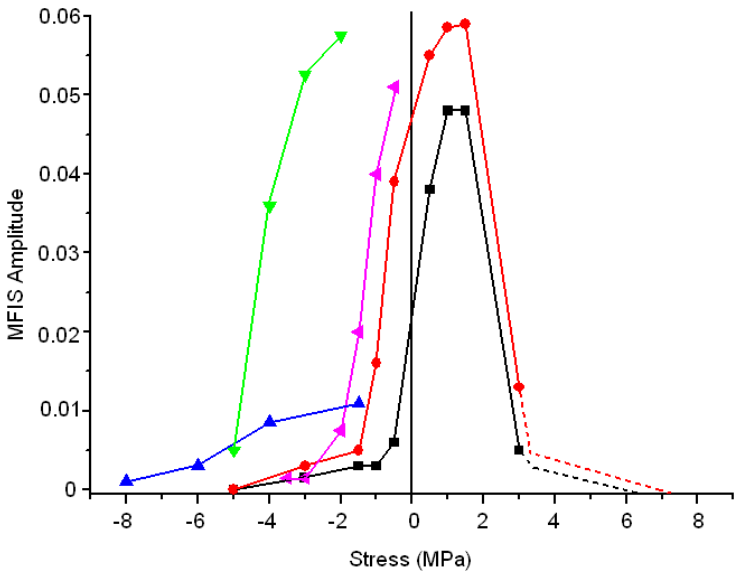

Figure 5.51: The maximum MFIS values under different uniaxial stresses are indicated in the figure, where the black squares represent values of our 3690 G experimental result, the red cycles represent values of our 5500 G result, the blue upward triangles represent values from experimental result of R. Tickle *et al.* with 12000 G field [9], the green downward triangles represent values from experiment of H. Karaca *et al.* with 15000 G field [20] and the pink triangles represent values from experiment of O. Heczko *et al.* with 11300 G field [10].

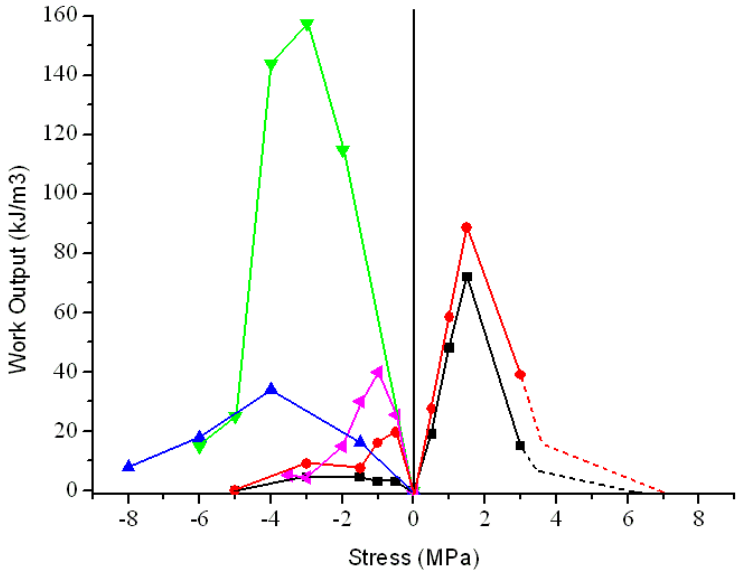

Figure 5.52: The work output values under different uniaxial stresses are indicated in the figure, where the black squares represent values of our 3690 G experimental result, the red cycles represent values of our 5500 G result, the blue upward triangles represent values from experimental result of R. Tickle *et al.* with 12000 G field [9], the green downward triangles represent values from experiment of H. Karaca *et al.* with 15000 G field [20] and the pink triangles represent values from experiment of O. Heczko *et al.* 11300 G field [10].

Chapter 6

Conclusions and Suggestions for Future Study

This dissertation studied the austenite-martensite (A-M) phase transformation processes and magneto-mechanical behaviors of the Ni_2MnGa ferromagnetic shape memory alloy (FMSA). Both theoretical and experimental works were developed to research the effects of stress and magnetic field on A-M phase transformation temperatures, the microstructure compatibilities between A-M interface and twin boundaries, and martensitic magnetic field induced strain under different magnetic field and uniaxial stress conditions for the single crystal longitude rectangular Ni_2MnGa sample. Two samples cut from almost same position in the Ni_2MnGa boule were used to perform different series of experiments.

From the microstructure pictures taken during phase transformation processes, it is found that the A-M interface and twin boundaries follow the theoretical compatibility calculations, though it may be hard to match each picture with one calculating result because the pictures only showed one dimension conditions. In order to match the microstructure with calculation exactly one by one, we need al least two orthogonal sample surfaces microstructure figures at the same time.

Under a certain large magnitude stresses application, which produce main part of the

ample into a single variant condition, the effect of stresses on the A-M phase transformation temperature will follow the Clausius-Clapeyron (C-C) theory prediction. The effect of compression on the phase transformation is about 0.2∼0.4 K/MPa, and the tension on the phase transformation is about 0.1 K/MPa. And the effect of magnetic field on the A-M phase transformation temperature is much harder to predict because under a lot of conditions, the microstructure is more complex than the theoretical assumption. Without explicitly figuring out the detail of microstructure in the sample, it is hardly to predict the effect of magnetic field on the phase transformation temperature theoretically.

In research of magneto-mechanical properties of Ni_2MnGa FSMA, the relationship between the applied stress and magnetic field, magnetization of the sample and the magnetic field induced strain (MFIS) of the rectangular single crystal sample is the most interesting topic, because this is related with the work output efficiency during the exchange process between mechanical energy and magnetic energy of the material on sensor or actuator applications. It is noticed that the initial homogeneous microstructure has a critical influence on the MFIS results, so first, a set of A-M phase transformation and detwinning processes were designed to obtain homogeneous microstructure before each MFIS experiment.

By applying different linear and rotary magnetic fields under different uniaxial stresses, the effects of applied magnetic field magnitudes, field paths and applied stresses on the magnetic field induced strains were investigated. It is found that, first, under same stresses and same magnetic field magnitudes, linear fields and rotary fields can obtain similar maximum MFIS values, but the data curves are much different. And this may be caused by the existences of 180^o magnetic domains or magnetic anisotropy. Second, under applied compression, the MFISs decreased with the increasing of the stress magnitudes with same applied field, but even under very small stress level (0.5 MPa), the MFIS is smaller than the theoretical prediction, while under a certain tension level ($\leq$ 2 MPa), the MFISs are very near the theoretical data, and also the MFIS decreased much with 3 MPa tension application. This is caused by different demagnetization factors

in longitude and transverse directions of the rectangular sample and the existence of the magnetic easy axis c of the Ni_2MnGa material. Further, it is predicted that the blocking stress for our longitude rectangular sample under tension will be larger than that under compression, and this will be proved true or not after finding some better adhesive to support the experimental tension larger than the possible blocking stress under martensitic temperature in future experiments. And it is concluded that work output under tension is larger than the same magnitude compression, which will help the potential uses of the longitude rectangular Ni_2MnGa material on sensor or actuator applications. Third, a simple calculation model based on micro-magneto-mechanical energy theory is used to analyze the relationship between the applied stress and magnetic field, magnetization of the sample and the magnetic field induced strain (MFIS) of the rectangular single crystal Ni_2MnGa sample in this dissertation. Comparing the theoretical model calculation and experimental results, it is found that the experimental results fit better with the theoretical results under tension than under compression and the experimental results indicate hysteresis behaviors, which can not obtain through the model calculations. So a more accurate model needs to be developed. The new model should include more energy mechanisms, such as twin boundary energy, and should be able to describe the hysteresis behaviors of MFISs. There are also some other interesting topics of MFISs of Ni_2MnGa FSMA, such as the size effect of sample on MFISs, the martensitic temperature effect on MFISs, which need more future further studies in order to provide a comprehensive theoretical support on the application of Ni_2MnGa ferromagnetic shape memory alloy.

References

[1] H. Funakubo. *Shape Memory Alloys*. Gordon and Breach Science Publisher, New York, 1987.

[2] T.W. Duerig, K.N. Melton, D. Stöckel, and C.M. Wayman. *Engineering Aspects of Shape Memory Alloys*. Butterworth-Heinemann, London; Boston, 1990.

[3] K. Otsuka and C.M. Wayman. *Shape Memory Materials*. Cambridge University Press, 1998.

[4] K. Otsuka and X. Ren. Recent developments in the research of shape memory alloys. *Intermetallics*, 7:511, 1999.

[5] C. Boller. Shape memory alloys - their challenge to contribute to smart structures. *Marterials For Smart Systems III*, M. Wun-Fogle, editor, 2000.

[6] M.J. Madou. *Fundamentals of Microfabrication - The Science of Miniaturization*. CRC Press, 2002.

[7] J.W. Christian. *The Theory of Transformations in Metals and Alloys, Part I*. Pergamon Press, 2002.

[8] K. Ullakko, J.K. Huang, C. Kantner, R.C. O'Handley, and V.V. Kokorin. Large magnetic-field-induced strains in Ni2MnGa single crystals. *Appl. Phys. Lett.*, 69:1966, 1996.

[9] R. Tickle, R.D. James, T.W. Shield, M. Wuttig, and V.V. Kokorin. Ferromagnetic shape memory in the NiMnGa system. *IEEE Trans. Magn.*, 35(5):4301, 1999.

[10] O. Heczko, A. Sozinov, and K. Ullakko. Giant field-induced reversible strain in magnetic shape memory NiMnGa alloy. *IEEE Trans. Magn.*, 36(5):3266, 2000.

[11] S.J. Murray, M.A. Marioni, S.M. Allen, R.C. O'Handley, and T.A. Lograsso. Giant magnetic-field-induced strain in Ni-Mn-Ga crystals: Experimental results and modeling. *J. Magn. Magn. Mater.*, 226:945, 2001.

[12] R.D. James and M. Wuttig. Magnetostriction of martensite. *Phil. Magn.*, A77:1273, 1998.

[13] R.C. O'Handley. Model for strain and magnetization in magnetic shape-memory alloys. *J. Appl. Phys.*, 83:3263, 1998.

[14] R. Tickle and R.D. James. Magnetic and magnetomechanical properties of Ni2MnGa. *J. Magn. Magn. Mater.*, 195:627, 1999.

[15] K. Inoue, K. Enami, M. Igawa, Y. Yamaguchi, and K. Ohoyama. Possibility of controlling the shape memory effect by magnetic field. *Inter. J. Appl. Elect. Mech.*, 12:25, 2000.

[16] B. Spasova, C. Ruffert, M.C. Wurz, and H.H. Gatzen. Application of MSM bulk material in a hybrid microactuator. *Phys. Stat. Sol.*, a205(10):2307, 2008.

[17] F. Khelfaoui, M. Kohl, J. Buschbeck, O. Heczko, S. Fähler, and L. Schultz. A fabrication technology for epitaxial Ni-Mn-Ga microactuators. *Eur. Phys. J. Special Topics*, 158:167, 2008.

[18] Y. Liang, H. Kato, and M. Taya. Model calculation of 3D-phase transformation diagram of ferromagnetic shape memory alloys. *Mech. Mater.*, 38:564, 2006.

[19] J. Cui, Y. Wu, and T.W. Shield. Effect of stress and magnetic field on martensitic phase transformation temperatures in FePd and NiMnGa single crystal. Revising (2009).

[20] H.E. Karaca, I. Karaman, B. Basaran, Y.I. Chumlyakov, and H.J. Maier. Magnetic field and stress induced martensite reorientation in NiMnGa ferromagnetic shape memory alloy single crystals. *Acta Mater.*, 54:233, 2006.

[21] C. Bechtold, A. Gerber, M. Wuttig, and E. Quandt. Magnetoelastic hysteresis in 5M NiMnGa single crystals. *Scrip. Mater.*, 58:1022, 2008.

[22] A. Malla, M.J. Dapino, T.A. Lograsso, and D.L. Schlagel. Large magnetically induced strains in Ni50Mn28.7Ga21.3 driven with collinear field and stress. *J. Appl. Phys.*, 99:063903, 2006.

[23] A. Sozinov, A.A. Likhachev, N. Lanska, and K. Ullakko. Giant magnetic-field-induced strain in NiMnGa seven-layered martensitic phase. *Appl. Phys. Lett.*, 80:1746, 2002.

[24] A.N. Vasil'ev, S.A. Klestov, V.V. Kokorin, R.Z. Levitin, V.V. Snegirev, and V.A. Chernenko. Magnetoelastic interaction under martensite transform in Ni2MnGa monocrystals. *Zhurn. Eksp I Teor. Fiziki*, 109(3):973, 1996.

[25] Y. Ganor, D. Shilo, T.W. Shield, and R.D. James. Breaching the work output limitation of ferromagnetic shape memory alloys. *Appl. Phys. Lett.*, 93:122509, 2008.

[26] K. Bhattacharya. *Microstructure of Martensite: Why It Forms and How It Gives Rise to The Shape-memory Effect*. Oxford University Press, 2003.

[27] M.F. Ashby and D.R.H. Jones. *Engineering Materials 2 (correction edition)*. Pergamon Press, 1998.

[28] R. Tickle. *Ferromagnetic Shape Memory Materials*. Ph.D. Thesis, University of Minnesota, 2000.

[29] T.W. Shield. Orientation dependence of the pseudoelastic behavior of single crystals of Cu-Al-Ni in tension. *J. Mech. Phys. Solids*, 43(6):869, 1995.

[30] R.C. O'Handley. *Modern Magnetic Materials Principles ans Application*. Wiley-Interscience Publication, 1999.

[31] J.M. Ball and R.D. James. Fine phase mixtures as minimizers of energy. *Arch. Rat. Mech. Anal*, 100:13, 1987.

[32] K.F. Hane. *Microsturctures in Thermoelastic Martensites*. Ph.D. Thesis, University of Minnesota, 1998.

[33] Fr. Heusler, W. Starck, and E. Haupt. *Verh. Deut. Phys. Ges.*, 5:219, 1903.

[34] V.V. Kokorin and V.V. Martynov. Subsequent formation of martensitic phases during uniaxial loading of Ni2MnGa single-crystals. *Fiz. Metal. Metalloved.*, 9:106, 1991.

[35] V.V. Kokorin, A.O. Perekos, A.A. Tshcherba, O.M. Babiy, and T.V. Efimova. Intermartensitic phase transitions in Ni-Mn-Ga alloy, magnetic field effect. *J. Magn. Magn. Mater*, 320(1):34, 2006.

[36] I.K. Zasimchuk, V.V. Kokorin, V.V. Martynov, A.V. Tkachenko, and V.A. Chernenko. The crystal structure of martensite in Heusler alloy Ni2MnGa. *Phys. Met. Metall*, 69:104, 1990.

[37] V. Kumar. Private communication. 2008.

[38] K. Shimizu and T. Kakashita. Effect of magnetic fields on martensitic transformations in ferrous alloys and steels. *ISIJ Int.*, 29:97, 1989.

[39] P.A. Malinen, V.D. Sadovskii, L.V. Smirnov, and Y.A. Fokina. Reasons for the influence of a pulsating magnetic field on martensitic transformation in steels and alloys. *Fiz. Metal. Metalloved.*, 23(3):535, 1967.

[40] A.E. Clark. *Ferromagnetic Materials*. Amsterdam: North-Holland, 1980.

[41] T.W. Shield. Magnetomechanical testing machine for ferromagnetic shape memory alloys. *Rev. Sci. Instru.*, 74(9):4077, 2003.

[42] K. Shimizu. Effect of stresses and magnetic fields on martensitic transformations. *Trans. Jpn. Inst. Metals*, 27(12):907, 1986.

[43] J.L. Ericksen. *Introduction to The Thermodynamics of Solids (Revised)*. Springer-Verlag Inc., 1991.

Appendix A

Details of Sample Preparation

The preparation processes of Ni_2MnGa single crystal experimental samples are made up of three main parts: orientating, cutting and polishing. In this section, the details of each part will be introduced.

A.1 Orientating Ni_2MnGa Single Crystal

The orientating process for Ni_2MnGa sample is followed as below steps:

1. Cut a 1mm thick un-oriented sample by using EDM from the top of Ni_2MnGa boule No.3, the normal direction [001] of the sample piece coincides with the direction [001] of the crystal boule;

2. Use acid solution ($HCl:HNO_3:H_2O$=2:1:1) to check if the sample cut from the boule is single crystalline or polycrystalline. If the sample is polycrystalline, it needs to check where is the grain boundary. After checking, it is found that the sample cut from boule-3 is not a single crystalline structure, the grain boundary detail is drawn in Figure A.1;

3. Polish the sample mechanically, until the sample surface is clean and shinny;

4. Send sample to X-ray Micro-diffraction (XRD) machine at Shepherd Laboratories to measure the crystal orientation. Here is the orientation data of the large crystal part 1 in Figure A.1:
   The normal direction is

$$\mathbf{n} = (0.93364, -0.35287, -0.06131). \tag{A.1}$$

   And the unit normal vector on the n-g plane is

$$\mathbf{n}_{n-g} = (0.99785, -0.06553). \tag{A.2}$$

   So the two orientation angles are

$$\alpha = \cos^{-1}(0.99785) = 3.76^{\circ}, \tag{A.3}$$

$$\beta = \cos^{-1}[\mathbf{n} \cdot \mathbf{n}_{n-g}] = 20.67^{\circ}. \tag{A.4}$$

   After these two important angle magnitudes obtained, the crystal boule can be sent to EDM to cut the designed orientation samples.

A.2 Cutting Samples From Ni_2MnGa Crystal Boule on EDM

For the EDM in the Electrical Engineering Department work shop, the tilt angle β of 20.67^o is too large. So we have to rotate the boule holder to minimize the tilt angle. The boule holder is rotated as 60^o, we can obtain the new inclined angle α'=19.8^o and tilt angle β'=7.11^o. We cut the normal oriented pieces A, B and C from the boule positions 20mm, 24mm and 28mm from the top, according angles α' and β' by using EDM.

After cutting, the crystalline structure of each sample piece, A, B and C, needs to be checked. We still use the acid solution to etch the sample pieces, then we find that all three pieces have the similar crystalline structures as drawn in Figure A.2. It needs to check which part is the normal oriented area that we want, so we go back to Shepherd Laboratories to check them by using XRD again. After this work, it is found that the upper part A in Figure A.2 is the normal oriented part.

By using the second time XRD orientation data, we can cut the 2.00mm[100]$\times$2.00mm[010] $\times$10.00mm[001] oriented sample pieces NMG3-P6, P7, P8 and P9 through calculated paths on EDM.

The composition variation of the Ni_2MnGa crystal boule, which has the nominal composition of Ni 50%, Mn 27% and Ga 23% along its long axis is shown in Figure B.3. After checking back the cutting positions of the samples, it is known that the samples NMG3-P6, P7, P8 and P9 have the same composition of Ni 49%, Mn 28% and Ga 23% at the position of the boule as shown in the vertical line in Figure A.3.

A.3 Polishing Process and Final Cleaning

In order to observe the sample surface microstructure change during the experiments, the (100) sample surface needs to be polished very well and satisfies the observation requirement of the optical microscopy in the MMTM. By using BUEHLER Minimet^{TM} polisher, which is shown in Figure A.4, and BUEHLER Carbinmet^{TM} discs polish papers that are the gray ones shown in Figure A.5, the samples can be polished from Grid 320 (rough) to Grid 1200 (fine). It is found that after Grid 1200 polishing, the surfaces can not satisfy the requriement of the observation, so the BUEHLER Mastertex^{TM} polishing cloth that is the white one shown in Figure B.5 and BUEHLER α Micropolish Alumina^{TM} polishing suspensions (5μm, 1μm, 0.3μm) as shown in Figure A.6 are used to polish samples to reach the requirement.

After the mechanical polishing, samples need to be washed by De-ion water, actone and alcohol at least three times, which will remove the polishing remains and greases and help the set up of the sample on the MMTM fixture.

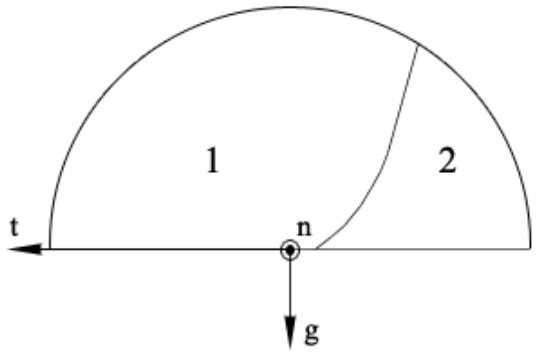

Figure A.1: Schematic Drawing of Grain Boundary on Un-oriented Sample.

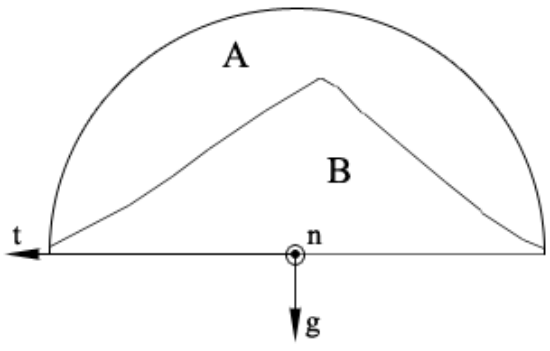

Figure A.2: Schematic Drawing of Grain Boundary on Oriented Sample.

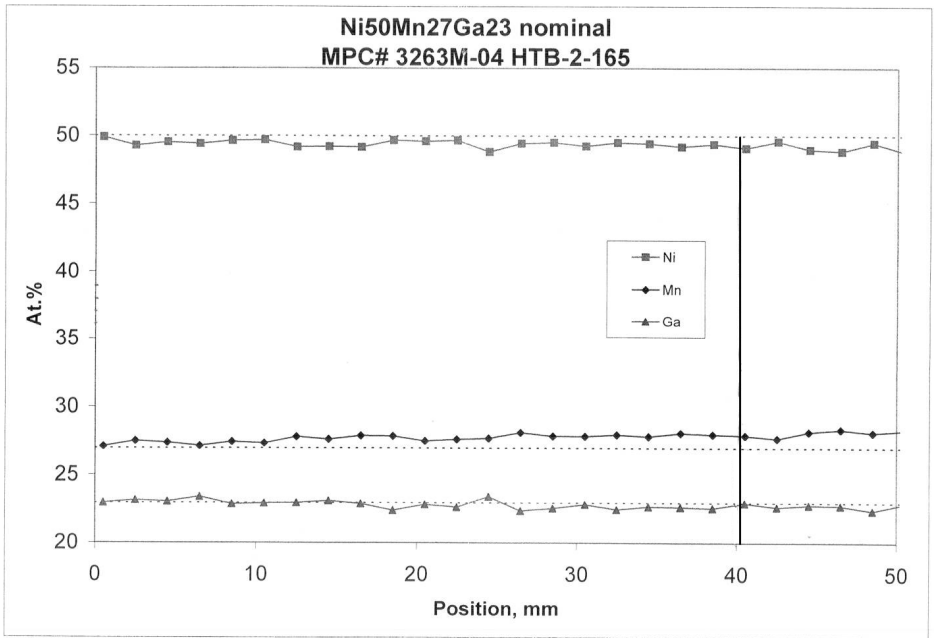

Figure A.3: Composition Variation in Ni_2MnGa Crystal Boule.

Figure A.4: BUEHLER Minimet Polisher.

Figure A.5: BUEHLER Polish Papers and Polishing Cloth.

Figure A.6: BUEHLER α Micropolish Alumina Polishing Suspensions.

Appendix B

Magneto-Mechanical Test Machine

Here is a schematic drawing of the magneto-mechanical test machine (MMTM) with the compression fixture, which is slightly different with the fixture in our experiments, (Courtesy of Professor Shield [43]) in Figure B.1.

The MMTM is designed and constructed to provide applied magnetic field and applied stress, which can rearrange the microstructure of the martensitic ferromagnetic shape memory alloy to the energetically favored condition. As brief described in Section 3.2.1, the MMTM is made of three main sub-systems. The first one is the load sub-system, which is the Instron 4467 mechanical testing machine with 1300 N load cell, and used to provide and control the applied stress. Its loading rod is made of non-magnetic aluminum bronze (alloy 642), which has a magnetic permeability near 1.0. The accuracy of the displacement and load control are 0.5μm and 0.05N. And the displacement and load can be both controlled manually or programmed. The displacement and load were not applied to the sample directly, but through the fixture on MMTM, which will be introduced in next appendix chapter. The second one is electromagnet sub-system, which includes four electromagnet coils, combined with four poles respectively. The combinations of coil and pole can produce different magnitude of magnetic field at the angles of 45^o/225^o and 135^o/315^o. All coils are made of hollow core copper conductors. And the cooling water can be pump through them during the operation. The coils are driven by a pair of bipolar 10 kW power supplies, the the currents in either pair of coils can be controlled separately by program. So by controlling separately the currents in either pair of coils, any orientation and magnitude (in the allowable range) magnetic field in the plane that contains the mechanical loading axis can be obtained. A maximum magnetic field of 8500 G (0.85 T) under full power of the supplies can be generated in the center of the 100mm pole gap. The third one is the temperature control sub-system. In order to perform A-M phase transformation experiments and low-temperature martensitic magneto-mechanical experiments, a PolyScience^{TM} temperature control system with Dynalene^{TM} HC-50 fluid is combined in MMTM. Based on this temperature control system, a temperature range of -50 to 150^{o}C can be provided to satisfy the experimental requirements. The temperature change range can not be set through program as load, displacement or magnetic field, it has to be set manually on the PolyScience^{TM} temperature control machine. And the maximum rate of

temperature change is about 1°C/min.

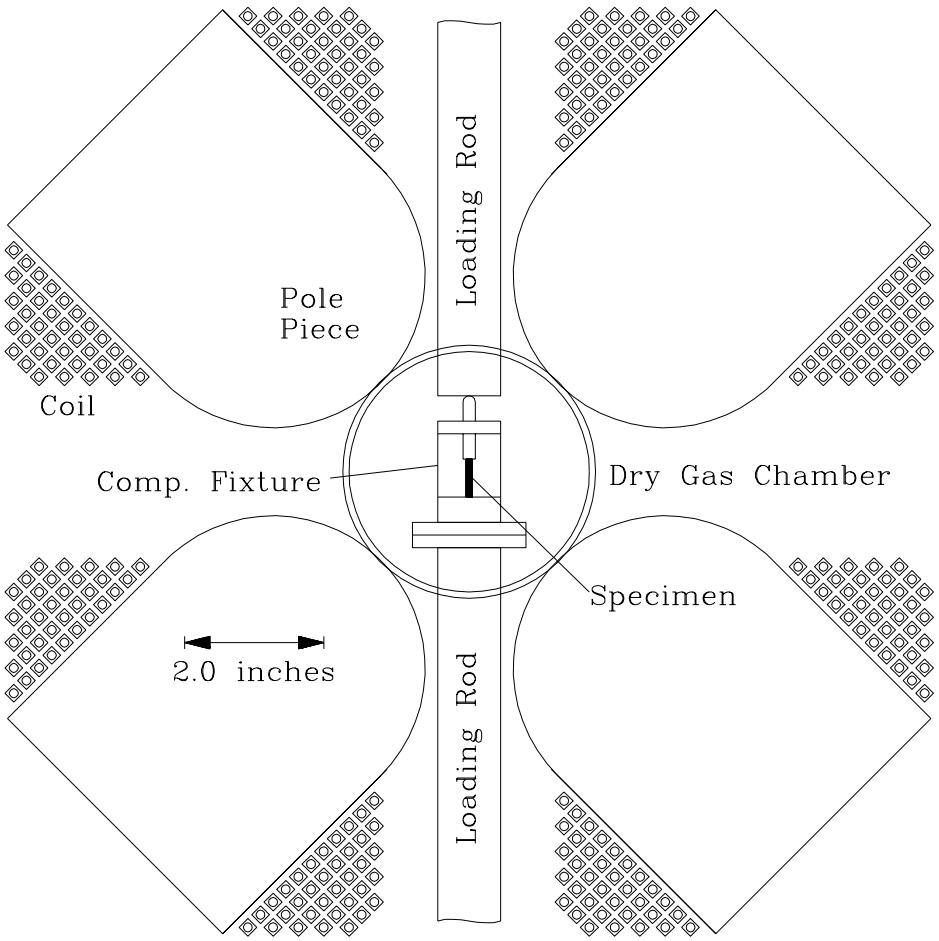

Figure B.1: Structure of Poles (with coils), Loading Rods and Fixture of the MMTM.

Appendix C

Sample Fixture on MMTM and Sample Loading Details

After the three main preparation processes of Ni_2MnGa single crystal rectangular experimental samples. The sample will be set up on the sample fixture and loaded into MMTM.

C.1 Sample Fixture on MMTM

From Figure 3.4, we can see: the Hall probes that used to measure the magnetic field around the sample, which will be further used to calculate the sample magnetization; the displacement sensor (cap. sensor) that used to measure the load head movement, which can be used to calculate the strain of the sample. And there is also a thermal couple on the back of the fixture to record the real time temperature change on the fixture and the sample. More details about the data recording and further calculation is shown in reported work [43].

And Figure C.1 is the schematic drawing of the fixture and load head. From Figure C.1, it can be found the 3D details of the fixture and load head. Because the sample is glued at the bottom with the fixture and at the top with the load rod, and the load rod is fixed with a rectangular load frame, so the load head can be moved up to apply tension or moved down to apply compression to the sample under the designed program. It needs to be noticed that when the sample is applied compression, the maximum allowable stress will depend only on the sample, but when it is applied tension, the maximum allowable stress will depend not only on the sample but also on the maximum bonding strength of the adhesive. The magnitudes of applied load and magnetic field are controlled by the MMTM, and will not be influenced by the fixture.

C.2 Sample Loading Details

Sample is glued by 3M Scotch-Weld^{TM} Instant Adhesive CA6 onto the fixture in MMTM. After final fine polishing, the sample and the fixture will be cleaned with acetone and alcohol, which will remove polish remains and greases and help improving the adhesive bonding strength. The CA6 instant adhesive is applied to sample and fixture under

room temperature, and the hard time of CA6 instant adhesive is less than 10 seconds, but the maximum bonding strength will be reached at least 18 hours at room temperature. So we could not start the experiment right after the adhesive becomes hard, but need to wait until the maximum bonding strength is reached. With an acceptable sample loading process, after 18 hours, the sample on the fixture can be applied at least 12N tension, which equals 3MPa, without any glue debonding. When it is found that the adhesive can support 12N tension, the designed experiments can be started.

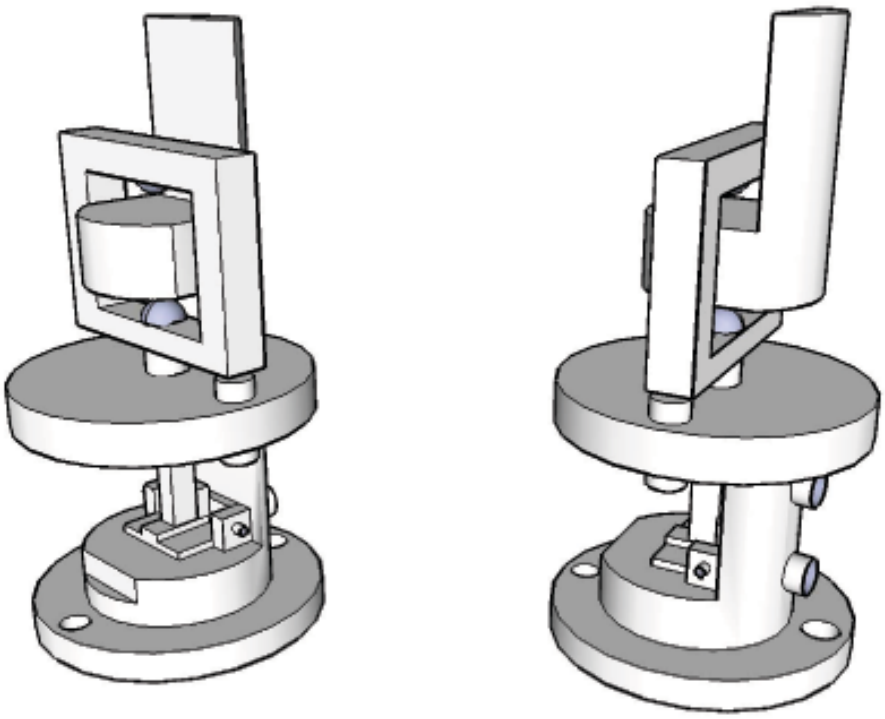

Figure C.1: 3D Schematic Drawing of MMTM Fixture and Load Head.

Appendix D

Program Control and Data & Images Recording System

The MMTM is controlled by a program called *mmtmcontrol* under computer *Ampere*. Before each experiment, the loading paths need to be designed and channels, which will be used during experiment running, need to be selected in the program. By inputting different loading paths, the applied load and magnetic field on the sample can be changed as different magnitudes and rates as different aims. All the real-time data obtained by different sensors including stress, load head displacement, temperature, currents in the coils and magnetic field measurement will be recorded automatic and drawn as selected channels through two windows, which will help to inspect the running condition of the test machine as shown in Figure E.1. The program running will be interrupted manually thus the MMTM will be stopped if there is anything wrong in the real-time figurations. And then the sample, MMTM and program set ups need to be checked on by one until the problem is figured out. Then the program and MMTM can be run again.

If everything is fine, after the test running as designed loading paths, the program will terminate the MMTM running. And then all acquired data in each experiment will be saved in one data file under selected directory in the computer.

At the same time of running *mmtmcontrol* in *Ampere*, the other program called *mediarecorder* will be run in the other computer *Tesla*, which is used to obtain the images or videos of the sample surface microstructure change through the microscope at the back side of MMTM. All the images or videos can be overlayed with real-time data, such as temperature, stress, coil currents, etc, which will help the later analysis on the microstructure change. The images or videos can be saved in the computer and the videos can also be saved in the accessorial video tape recorder.

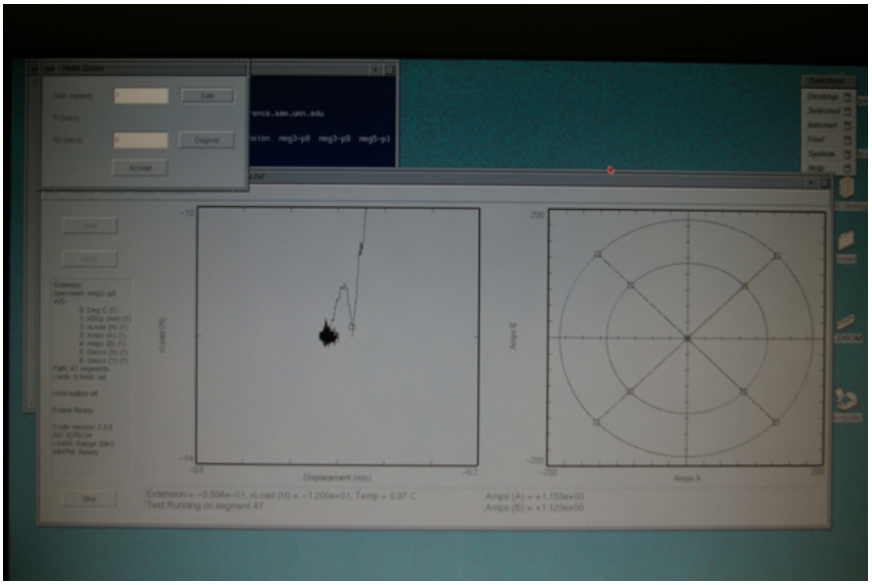

Figure D.1: Mmtmcontrol Program Window.

Appendix E

Matlab Code of Theoretical Calculation

All theoretical calculations are finished based on Matlab program. C: Define π and demaganitization factors (D_v, D_h);

1: pi=3.1415926;

2: Dv = 0.0878938;

3: Dh = (1-Dv)/2;

C: Define magnitude of the applied field $(h_0 : Gauss)$

C: and saturation magnetization value $(m_s : emu/cc)$of Ni_2MnGa sample;

3: h0 = 5500;

4: ms = 900;

C: Define loading stress ($\sigma : erg/cc$, where 1 $MPa = 10^7 erg/cc$,

C: and positive value means compression, negative value means tension);

5: sigma = 70000000;

C: Define strains related with lattice parameters;

6: lata = 5.92/5.82-1.0;

7: latc = 5.57/5.82-1.0;

C: Define anisotropy energy of Ni_2MnGa material $(K_u : erg/cc)$;

8: anisoA = 2450000;

C: Define the range of angles to check over;

9: maxdtm = 90;

C: Define the running step length;

10: tstep = maxdtm/100;

C: Define the minimum magnetization to check;

11: magmin = ms/2;

C: Define the resolution in magnetization to check;

12: magstep = (ms-magmin)/10;

13:

14: for ii = 0:90

15: thetah = ii;

16: emin = 1000000;

17: t1min = 0;

18: t2min = 0;

19: m1min = 0;

```
20: m2min = 0;
21: fmin = 0;
22: thetam1 = 0;
23:
24: if thetam1 < maxdtm
25:     thetam2 = 0;
26: if thetam2 < maxdtm
27:     m1 = ms;
28: if m1 > magmin
29:     m2 = ms;
30: if m2 > magmin
31:     thetah = pi*thetah/180;
32:     thetam1 = pi*thetam1/180;
33:     thetam2 = pi*thetam2/180;
34:
35:ch = cos(thetah);
36:sh = sin(thetah);
37:cm1 = cos(thetam1);
38:sm1 = sin(thetam1);
39:cm2 = cos(thetam2);
40:sm2 = sin(thetam2);
41:dmdf1 = m1*cm1-m2*sm2;
42:dmdf2 = m1*sm1-m2*cm2;
43:
44:f=(-sigma*(lata-latc)+h0*(ch*dmdf1+sh*dmdf2)
45:-4*pi*(Dh*m2*sm2*dmdf1+Dv*m2*cm2*dmdf2)-anisoA*(sm1*sm1-
46:sm2*sm2))/(4*pi*(Dh*dmdf1*dmdf1 + Dv*dmdf2*dmdf2));
47:
48: if f < 0.0
49:     f = 0.0;
50:     fp = 1.0;
51:       mbar1 = f*m1*cm1+fp*m2*sm2;
```

```
52:       mbar2 = f*m1*sm1+fp*m2*cm2;
53:        e0 = sigma*(fp*latc+f*lata)-h0*(ch*mbar1+sh*mbar2)
54:        +2*pi*(Dh*mbar1*mbar1+Dv*mbar2*mbar2)
55:        +f*anisoA*sm1*sm1+fp*anisoA*sm2*sm2;
56:      f = 1;
57:      fp = 0.0;
58:       mbar1 = f*m1*cm1+fp*m2*sm2;
59:       mbar2 = f*m1*sm1+fp*m2*cm2;
60:        e1 = sigma*(fp*latc+f*lata)-h0*(ch*mbar1+sh*mbar2)
61:        +2*pi*(Dh*mbar1*mbar1+Dv*mbar2*mbar2)
62:        +f*anisoA*sm1*sm1+fp*anisoA*sm2*sm2;
63:
64:          if e1 < e0
65:             f = 1.0;
66:             e = e1;
67:          else
68:             f = 0.0;
69:             e = e0;
70:          end
71:
72: elseif f > 1.0
73:      f = 0.0;
74:      fp = 1.0;
75:       mbar1 = f*m1*cm1+fp*m2*sm2;
76:       mbar2 = f*m1*sm1+fp*m2*cm2;
77:        e0 = sigma*(fp*latc+f*lata)-h0*(ch*mbar1+sh*mbar2)
78:        +2*pi*(Dh*mbar1*mbar1+Dv*mbar2*mbar2)
79:        +f*anisoA*sm1*sm1+fp*anisoA*sm2*sm2;
80:      f = 1;
81:      fp = 0.0;
82:       mbar1 = f*m1*cm1+fp*m2*sm2;
83:       mbar2 = f*m1*sm1+fp*m2*cm2;
```

```
84:          e1 = sigma*(fp*latc+f*lata)-h0*(ch*mbar1+sh*mbar2)
85:          +2*pi*(Dh*mbar1*mbar1+Dv*mbar2*mbar2)
86:          +f*anisoA*sm1*sm1+fp*anisoA*sm2*sm2;
87:
88:             if e1 < e0
89:                f = 1.0;
90:                e = e1;
91:             else
92:                f = 0.0;
93:                e = e0;
94:             end
95:
96: else
97:       fp = 1.0 - f;
98:       mbar1 = f*m1*cm1 + fp*m2*sm2;
99:       mbar2 = f*m1*sm1 + fp*m2*cm2;
100:      e = sigma*(fp*latc+f*lata)-h0*(ch*mbar1+sh*mbar2)
101:      +2*pi*(Dh*mbar1*mbar1+Dv*mbar2*mbar2)
102:      +f*anisoA*sm1*sm1+fp*anisoA*sm2*sm2;
103:end
104:
105:if e < emin
106:    emin = e;
107:    m1min = m1;
108:    t1min = thetam1;
109:    m2min = m2;
110:    t2min = thetam2;
111:    fmin = f;
112:    end
113:
114:m2 = m2 - magstep;
115:end
```

```
116:m1 = m1 - magstep;
117:end
118:thetam2 = thetam2 + tstep;
119:end
120:thetam1 = thetam1 + tstep;
121:end
122:
123:t1min = pi*t1min/180;
124:t2min = pi*t2min/180;
125:c1 = cos(t1min);
126:s1 = sin(t1min);
127:c2 = cos(t2min);
128:s2 = sin(t2min);
129:fp = 1.0 - fmin;
130:
131:mx = fmin*m1min*c1+fp*m2min*s2;
132:my = fmin*m1min*s1+fp*m2min*c2;
133:
134:avemag= sqrt(mx*mx+my*my);
135:avemangle= atan(my/mx)*180/pi;
136:epsilon = lata*(1-fmin)+latc*fmin;
137:
138:fvec(ii+1)=f;
139:eminvec(ii+1)=emin;
140:avemagvec(ii+1)=avemag;
141:avemanglevec(ii+1)=avemangle;
142:avemangle1vec(ii+1)=-avemangle;
143:epsilonvec(ii+1)=epsilon;
144:thetahvec(ii+1)=thetah*180/pi;
145:thetah1vec(ii+1)=-thetah*180/pi;
146:end
```

Appendix F

Experimental Data File Directories in Workstation

Table F.1: All A-M phase transformation temperature test files are saved at workstation Ampere under /usr2/home/ymwu/nmg3-p8 directory.

Test Name	Subdirectory Under /usr2/home/ymwu/nmg3-p8
PT Temp. 1	../oct-27-2007/load-32n-comp-nofield-temp.gf
PT Temp. 2	../oct-27-2007/load-32n-comp-field-65-001-temp.gf
PT Temp. 3	../oct-27-2007/load-32n-comp-field-130-001-temp.gf
PT Temp. 4	../oct-27-2007/load-32n-comp-field-65-010-temp.gf
PT Temp. 5	../oct-27-2007/load-32n-comp-field-130-010-temp.gf
PT Temp. 6	../nov-7-2007/load-8n-comp-nofield-temp.gf
PT Temp. 7	../nov-7-2007/load-8n-comp-field-65-001-temp.gf
PT Temp. 8	../nov-7-2007/load-8n-comp-field-130-001-temp.gf
PT Temp. 9	../nov-7-2007/load-8n-comp-field-65-010-temp.gf
PT Temp. 10	../nov-7-2007/load-8n-comp-field-130-010-temp.gf
PT Temp. 11	../nov-7-2007/load-4n-comp-nofield-temp.gf
PT Temp. 12	../nov-7-2007/load-4n-comp-field-65-001-temp.gf
PT Temp. 13	../nov-7-2007/load-4n-comp-field-130-001-temp.gf
PT Temp. 14	../nov-7-2007/load-4n-comp-field-65-010-temp.gf
PT Temp. 15	../nov-7-2007/load-4n-comp-field-130-010-temp.gf
PT Temp. 16	../2007-dec/load-4n-tens-nofield-temp.gf
PT Temp. 17	../2007-dec/load-4n-tens-field-65-001-temp.gf
PT Temp. 18	../2007-dec/load-4n-tens-field-130-001-temp.gf
PT Temp. 19	../2007-dec/load-4n-tens-field-65-010-temp.gf
PT Temp. 20	../2007-dec/load-4n-tens-field-130-010-temp.gf
PT Temp. 21	../2007-dec/load-8n-tens-nofield-temp.gf
PT Temp. 22	../2007-dec/load-8n-tens-field-65-001-temp.gf
PT Temp. 23	../2007-dec/load-8n-tens-field-130-001-temp.gf
PT Temp. 24	../2007-dec/load-8n-tens-field-65-010-temp.gf
PT Temp. 25	../2007-dec/load-8n-tens-field-130-010-temp.gf
PT Temp. 26	../2007-dec/load-12n-tens-nofield-temp.gf
PT Temp. 27	../2007-dec/load-12n-tens-field-65-001-temp.gf
PT Temp. 28	../2007-dec/load-12n-tens-field-130-001-temp.gf
PT Temp. 29	../2007-dec/load-12n-tens-field-65-010-temp.gf
PT Temp. 30	../2007-dec/load-12n-tens-field-130-010-temp-break.gf

Table F.2: All preliminary training and magneto-mechanical test files are saved at workstation Ampere under /usr2/home/ymwu/nmg3-p9 directory.

Test Name	Subdirectory Under /usr2/home/ymwu/nmg3-p9
PTtest1	../phasetransformation/Comp-32n-field-130-001-temp-1.gf
PTtest2	../phasetransformation/Comp-4n-field-130-001-temp-1.gf
PTtest3	../phasetransformation/Load-0n-no-field-temp.gf
PTtest4	../phasetransformation/Tens-4n-field-130-010-temp.gf
PTtest5	../phasetransformation/Tens-12n-field-130-010-temp.gf
TRtest1	../finaltest/32n-comp-cooling-detwin.gf
TRtest2	../finaltest/32n-comp-cooling-detwin-6.gf
TRtest3	../finaltest/32n-comp-cooling-detwin-4.gf
PMFIS1	../rotatefield/Comp-4n-2n-field-001-9rot-2.gf
PMFIS2	../rotatefield/Tens-4n-2n-field-010-9rot-2.gf
PMFIS3	../finaltest/linear-rotate-field-repeat-with-demag-stop-at-max-2.gf
PMFIS4	../finaltest/linear-rotate-field-repeat-with-demag-stop-at-max-3.gf
PMFIS5	../finaltest/linear-rotate-field-repeat-with-demag-stop-at-max-1.gf
PMFIS6	../finaltest/linear-rotate-field-repeat-with-demag-stop-at-max-4.gf

Table F.3: All final magneto-mechanical test and magnetization calibration files are saved at workstation Ampere under /usr2/home/ymwu/finalexp directory.

Test Name	Subdirectory Under /usr2/home/ymwu/finalexp
MFIS1	../comp-2N-60s-hold-MFIS-1.gf
MFIS2	../comp-4N-60s-hold-MFIS.gf
MFIS3	../comp-6N-60s-hold-MFIS.gf
MFIS4	../comp-12N-60s-hold-MFIS.gf
MFIS5	../comp-20N-MFIS-1.gf
MFIS6	../tens-2N-60s-hold-MFIS.gf
MFIS7	../tens-4N-60s-hold-MFIS.gf
MFIS8	../tens-6N-60s-hold-MFIS.gf
MFIS9	../tens-12N-60s-hold-MFIS.gf
MFIS10	../tens-20N-60s-hold-MFIS-broken.gf
Comp. Magn. Cali. 1	../cali-comp.gf
Comp. Magn. Cali. 2	../cali-comp-60s.gf
Tens. Magn. Cali. 1	../cali-tens.gf
Tens. Magn. Cali. 1	../cali-tens-60s.gf